



UNIVERSITÀ  
DI TRENTO

---

Department of Mathematics

---

# A 0D-1D Global, Closed-Loop Model of the Cardiovascular System

Master Degree in Mathematics

Supervisor

Prof. Lucas Omar Müller (UniTN)

Candidate

Stefano Costa

---

Co-supervisor

Dr. Federica Caforio (UniGRAZ)

---

Date of Discussion:

Academic year 2023-24



---

## Acknowledgement

---

I thank everyone who feels they should be thanked.



---

# Table of contents

---

	Page
<b>1    Introduction</b>	<b>13</b>
1    Motivation and Goal . . . . .	15
2    Introduction to the Physiology of the Cardiovascular System . . . . .	15
<b>2    The ADAVN model</b>	<b>31</b>
1    Introduction . . . . .	33
2    The Reduced ADAVN Model . . . . .	34
3    The Mathematical Model . . . . .	38
4    High-Order Finite Volume Solver for 1D Blood Flow Simulations . . . . .	43
5    Boundary Conditions and Coupling Methods . . . . .	54
<b>3    The CircAdapt model</b>	<b>63</b>
1    Introduction to the Model . . . . .	65
2    Tube Module . . . . .	66
3    Sarcomere Module . . . . .	68
4    Chamber Module . . . . .	70
5    TriSeg Model of Ventricular Interaction . . . . .	72
6    Pericardial Mechanics . . . . .	74
7    Periphery . . . . .	74
8    Connecting the Modules . . . . .	75
9    Valve Dynamics . . . . .	75
10   Solving the ODE System . . . . .	77
11   Limitations of the CircAdapt Model . . . . .	84
<b>4    Coupling strategy</b>	<b>87</b>
1    Model Adjustments for Coupling . . . . .	89
2    Communication Between Models . . . . .	90
3    Numerical Stability . . . . .	92
<b>5    Results and Discussion</b>	<b>97</b>
1    Performance and Computational Speed of the Coupled Model . . . . .	99
2    Convergence Analysis . . . . .	99
3    Convergence of the Curves . . . . .	101
4    Haemodynamic Variables . . . . .	104
5    Curve Plots of Simulation Data . . . . .	107
<b>6    Conclusions</b>	<b>117</b>
1    Challenges in the Implementation . . . . .	119

2	Limitations of the Model . . . . .	119
3	Future Steps . . . . .	120
<b>7</b>	<b>Appendix</b>	<b>121</b>
1	Detailed Description of Vascular Connectivity in the ADAVN Model . . . . .	123
2	Cardiovascular Adaptation Mechanisms in CircAdapt . . . . .	136

---

# List of Figures

---

1.1	Diagram of the circulatory system . . . . .	16
1.2	The swirling pattern of myocardium . . . . .	18
1.3	Spatial and temporal scales of mechanisms contributing to heart function . . . . .	19
1.4	Illustration of a cardiac muscle cell . . . . .	20
1.5	A diagram illustrating various components of cardiac sarcomere structure . . . . .	20
1.6	Illustration of the valves of the heart when the ventricles are contracting . . . . .	22
2.1	Schematic representation of a generic vessel network . . . . .	33
2.2	One-dimensional counterpart of a generic vessel network . . . . .	34
2.3	Full ADAVN vessel network . . . . .	35
2.4	Schematic illustration for a generic peripheral circulation model in ADAVN . . . . .	37
2.5	Position of Starling-resistor elements in the cerebral venous network in ADAVN	42
2.6	Schematic representation of the numerical solution at three vessels sharing a node	54
2.7	Schematic representation of the numerical solution at three vessels sharing a node $P$ . . . . .	55
2.8	RCR lumped parameter model . . . . .	58
3.1	Schematic representation of the cardiovascular system in the CircAdapt model .	65
3.2	Diagram of the CircAdapt model equations and their solution process . . . . .	66
3.3	Schematic diagram of the CircAdapt model in circuit form . . . . .	67
3.4	TriSeg model of septal and left and right ventricular mechanics . . . . .	72
3.5	Schematic of the open and regurgiting valve in the CircAdapt model . . . . .	76
3.6	Solution of $y' = -2.3y$ computed with the forward Euler method with different step sizes . . . . .	83
4.1	The diagram shows the coupling between the ADAVN and CircAdapt models .	91
4.2	Diagram showing the update sequence of the coupled model . . . . .	92
5.1	Convergence of the PV loop in LV . . . . .	100
5.2	Convergence of the pressure profile in the ascending aorta . . . . .	100
5.3	Convergence of the pressure in the superior vena cava . . . . .	101
5.4	Convergence of the pressure profile in the left interior jugular vein . . . . .	101
5.5	Pressure in the cardiac chambers over 10 cardiac cycles . . . . .	102
5.6	Pressure and volume in the left ventricle . . . . .	108
5.7	Pressure and volume in the right ventricle . . . . .	108
5.8	PV loop of left ventricle in CircAdapt . . . . .	109
5.9	PV loop of right ventricle in CircAdapt . . . . .	109
5.10	Pressure and volume in the left atrium . . . . .	110
5.11	Pressure and volume in the right atrium . . . . .	110
5.12	Mass conservation in CircAdapt . . . . .	111

5.13 Pressure and flow in the ascending aorta . . . . .	112
5.14 Pressure and flow in the abdominal aorta . . . . .	112
5.15 Pressure and flow in the superior vena cava . . . . .	112
5.16 Pressure and flow in the right common carotid artery . . . . .	113
5.17 Pressure and flow in the right femoral vein . . . . .	113
5.18 Pressure and flow in the left internal jugular vein . . . . .	114
7.1 Left anterior cerebral artery and its connected terminal veins within the ADAVN model . . . . .	123
7.2 Right anterior cerebral artery and its connected terminal veins within the ADAVN model . . . . .	123
7.3 Left middle cerebral cerebral artery and its connected terminal veins within the ADAVN model . . . . .	124
7.4 Right middle cerebral cerebral artery and its connected terminal veins within the ADAVN model . . . . .	124
7.5 Left posterior cerebral postcommunicating artery and its connected terminal veins within the ADAVN model . . . . .	125
7.6 Right posterior cerebral postcommunicating artery and its connected terminal veins within the ADAVN model . . . . .	125
7.7 Left external carotid artery and its connected terminal veins within the ADAVN model . . . . .	126
7.8 Right external carotid artery and its connected terminal veins within the ADAVN model . . . . .	126
7.9 Azygos vein and its connected arteries within the ADAVN model . . . . .	127
7.10 Hepatic vein and its connected arteries within the ADAVN model . . . . .	127
7.11 Venous perforator and its connected arteries within the ADAVN model . . . . .	128
7.12 Left renal vein and its connected arteries within the ADAVN model . . . . .	128
7.13 Right renal vein and its connected arteries within the ADAVN model . . . . .	129
7.14 Right internal iliac vein and its connected arteries within the ADAVN model . . . . .	129
7.15 Left internal iliac vein and its connected arteries within the ADAVN model . . . . .	130
7.16 Left posterior interosseous artery and its connected veins within the ADAVN model . . . . .	130
7.17 Right posterior interosseous artery and its connected veins within the ADAVN model . . . . .	131
7.18 Left radial artery and its connected veins within the ADAVN model . . . . .	131
7.19 Right radial artery and its connected veins within the ADAVN model . . . . .	132
7.20 Left ulnar artery and its connected veins within the ADAVN model . . . . .	132
7.21 Right ulnar artery and its connected veins within the ADAVN model . . . . .	133
7.22 Left profunda femoris artery and its connected veins within the ADAVN model . . . . .	133
7.23 Right profunda femoris artery and its connected veins within the ADAVN model . . . . .	134
7.24 Left anterior tibial artery and its connected veins within the ADAVN model . . . . .	134
7.25 Right anterior tibial artery and its connected veins within the ADAVN model . . . . .	135
7.26 Left posterior tibial artery and its connected veins within the ADAVN model . . . . .	135
7.27 Right posterior tibial artery and its connected veins within the ADAVN model . . . . .	136
7.28 Impact of increased arterial pressure on stroke volume via peripheral resistance mechanisms. . . . .	138
7.29 Patient-specific modeling to reduce parameter uncertainty and enable diagnostic differentiation . . . . .	139
7.30 Summary diagram of blood vessel structure . . . . .	141

---

## List of Tables

---

5.1	Convergence norms for the total mass in the coupled model. . . . .	103
5.2	Convergence norms for pressure, volume, and flow in various cardiovascular compartments in ADAVN and CircAdapt models. . . . .	104
5.3	Main model-predicted cardiac and haemodynamic variables and reference values reported in the literature. . . . .	107



---

## List of Algorithms

---

1	Local time step update algorithm . . . . .	53
2	LTS solver algorithm . . . . .	59



## Introduction

## Contents of the chapter

---

1	Motivation and Goal . . . . .	15
2	Introduction to the Physiology of the Cardiovascular System . . . . .	15
2.1	Circulatory System . . . . .	15
2.2	Structure and Function of the Human Heart . . . . .	17
2.3	Multiscale Aspects of Cardiovascular System . . . . .	18
2.4	Anatomy of the Sarcomere . . . . .	19
2.5	Structure and Function of the Pericardium . . . . .	20
2.6	Anatomy of Heart Valves . . . . .	20
2.7	Mechanical Properties of Vessels in the Cardiovascular System . . . . .	21
2.8	Role of Peripheral Vasculature in Controlling Blood Flow . . . . .	23
2.9	Vascular distensibility . . . . .	23
2.10	The Role of Arteries in the Cardiovascular System . . . . .	24
2.11	The Role of Veins in the Cardiovascular System . . . . .	25

---

## 1 Motivation and Goal

Cardiovascular disease remains a leading cause of morbidity and mortality worldwide [19, 25], necessitating continuous advancements in modeling and simulation techniques to enhance our understanding of its intricacies [14]. Multidimensional models have proven to be valuable tools in the field of cardiovascular modeling. [1, 22].

Multiscale models in cardiovascular simulations are particularly effective in integrating processes at different spatial and temporal scales, such as heart chamber dynamics (0D) and blood flow in large vessels (1D). These models provide a means to simulate complex physiological processes and their interactions within the cardiovascular system. By capturing how localized changes in heart function can impact systemic hemodynamics, multiscale models reflect the interconnectedness of cardiovascular components. Such models offer deeper insights into disease mechanisms by allowing for the simulation of various pathologies [1, 13].

Multiscale approaches are highly effective in understanding disease mechanisms by linking global hemodynamic parameters, such as pressure and flow in large vessels (1D), with localized phenomena in heart chambers (0D). This approach provides a more comprehensive understanding of disease progression, enabling the prediction of how specific pathologies impact both local and systemic cardiovascular function. [1, 22].

An example of a coupled model can be found in [9], where the 0D CircAdapt model is coupled with a transmission line model to simulate both normotensive and hypertensive conditions. Although the results are promising, the model employs a simplified vessel network and uses linear methods, omitting the nonlinear advection term.

The objective of this work is to couple the CircAdapt model (a 0D model) with a reduced version of the ADAVN model (a 1D model). In this configuration, the heart and pulmonary circulation from CircAdapt are integrated with the detailed systemic circulation from the ADAVN model. The long-term goal is to create a coupled model capable of analyzing key parameters in the anatomically precise 1D circulation, such as pressure wave propagation, in response to modifications in the 0D CircAdapt heart model, which can simulate various cardiac pathologies.

The combination of these models will enhance the ability to study the systemic impacts of localized cardiac changes, providing a more integrated understanding of the heart's interaction with the entire circulatory system.

## 2 Introduction to the Physiology of the Cardiovascular System

This section explains the basic anatomical principles of the components of the cardiovascular system. By exploring the physiological principles that govern cardiovascular dynamics, a comprehensive understanding can be achieved, facilitating the integration into the models discussed in [Chapter 3](#) and [Chapter 2](#).

### 2.1 Circulatory System

#### Overview of the Circulatory System

The circulatory system is a system of organs that includes the heart, blood vessels, and blood which is circulated throughout the entire body [8]. The circulatory system has two divisions, a systemic circulation and a pulmonary circulation, as can be seen in [Figure 1.1](#).

The pulmonary circulation is a circuit loop from the right heart taking deoxygenated blood to the lungs where it is oxygenated and returned to the left heart. The systemic circulation

is a circuit loop that delivers oxygenated blood from the left heart to the rest of the body, and returns deoxygenated blood back to the right heart via large veins known as the venae cavae. The systemic circulation can also be defined as two parts - a macrocirculation and a microcirculation.

An average adult contains 4.7 to 5.7 liters of blood, accounting for approximately 7% of their total body weight. Blood consists of plasma, red blood cells, white blood cells, and platelets. Further circulatory routes are associated, such as the coronary circulation to the heart itself, the cerebral circulation to the brain, renal circulation to the kidneys, and bronchial circulation to the bronchi in the lungs. The human circulatory system is closed, meaning that the blood is contained within the vascular network. Nutrients travel through tiny blood vessels of the microcirculation to reach organs.

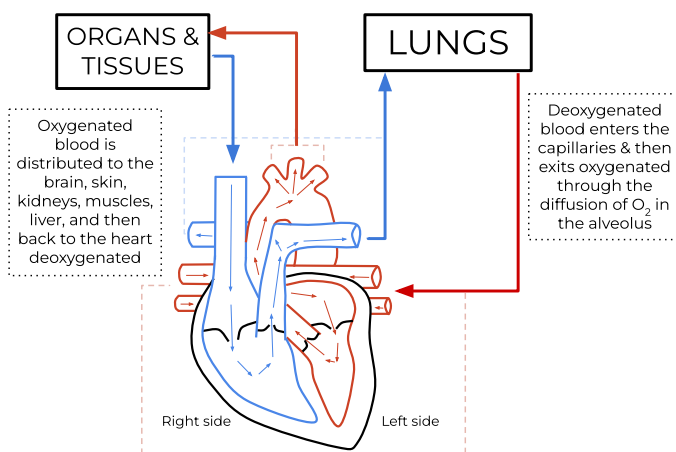


**Figure 1.1:** Diagram of the circulatory system. Image attribution: Sasha River Santilla, [Blood oxygenation to the pulmonary and systemic circulation, CC BY-SA 4.0](#).

## Blood Flow

The circulatory system uses the channel of blood vessels to deliver blood to all parts of the body [20]. This is a result of the left and right side of the heart working together to allow blood to flow continuously to the lungs and other parts of the body. The capillaries are responsible for allowing the blood to receive oxygen through tiny air sacs in the lungs. This is also the site where carbon dioxide exits the blood. This all occurs in the lungs where blood is oxygenated. The blood pressure in blood vessels is traditionally expressed in millimetres of mercury ( $1mmHg = 133Pa$ ). In the arterial system, this is usually around  $120mmHg$  systolic (high pressure wave due to contraction of the heart) and  $80mmHg$  diastolic (low pressure wave). In contrast, pressures in the venous system are constant and rarely exceed  $10mmHg$ .

Vessel length is the total length of the vessel measured as the distance away from the heart. As the total length of the vessel increases, the total resistance as a result of friction will increase. Vessel radius also affects the total resistance as a result of contact with the vessel wall. As the radius of the wall gets smaller, the proportion of the blood making contact with the wall will increase. The greater amount of contact with the wall will increase the total resistance against the blood flow.

## 2.2 Structure and Function of the Human Heart

### Chamber Structure and Blood Circulation in the Human Heart

The human heart comprises two main chambers called ventricles and two antechambers called atria. It is divided into the left and right sides, where the right side pumps deoxygenated blood into the pulmonary circulation, and the left side pumps oxygenated blood into the systemic circulation. Both sides function in a synchronized manner. The atria contract almost simultaneously, filling the ventricles, which then contract after approximately 120 ms, performing the main pumping action necessary for blood circulation[7].

The heart connects to several key vessels: the aorta (for systemic circulation), two venae cavae (returning blood from systemic circulation), pulmonary arteries and veins (for pulmonary circulation) [16]. Additionally, it includes four heart valves (pulmonary, tricuspid, mitral, and aortic) that regulate blood flow between chambers and into the pulmonary artery/aorta, coronary arteries and veins (supplying oxygen to the heart muscle), and the pericardium (a double-layered membranous sac that surrounds and stabilizes the heart).

### Muscular Architecture and Fiber Orientation in Ventricle and Atria

Although the complex muscular architecture of the ventricles has been studied for centuries, a comprehensive description of the macroscopic morphological structure of the cardiac muscle has only emerged in the last fifty years [18]. Torrent-Guasp [23, 24] proposed that both ventricles are formed by a single band of fibers, the Ventricular Myocardial Band (VMB), twisted into a helicoidal configuration with two spiral turns. Streeter's measurements [21] revealed a transmural variation of fiber direction, ranging from about  $-70^\circ$  in the short-axis plane at the outer ventricular surface (epicardium) to approximately  $+80^\circ$  at the inner part of the wall (endocardium). See also [Figure 1.2](#) for a representation.

By idealizing the left ventricle (LV) as a truncated prolate ellipsoid, fiber orientation can be analytically defined [3, 6]; these angles can be optimized to closely match experimental data. Following the hypothesis that fibers follow geodesic paths on toroidal surfaces within the ventricular wall [21], Peskin developed a mathematical theory describing fiber orientation using approximate geodesics [17]. Recently, another approach [21] based on the VMB concept described the LV as a set of identical spiral surfaces mapped from a half disc. This rule-based description of left ventricular anisotropy, consistent with Streeter's experimental data, supports Torrent-Guasp's VMB theory.

A similar structural arrangement is found in the atria, where the muscle fibers also exhibit a complex, layered architecture that supports efficient atrial contraction and blood flow dynamics. The atrial myocardium consists of bundles of muscle fibers arranged in an intricate pattern, forming a mesh-like network that allows for coordinated contraction and optimal blood flow regulation [10].

### Impact of Ventricular Radius on Wall Tension and Blood Pressure

The radius of the ventricle plays a crucial role in determining how effectively the active wall tension raises blood pressure [16]. This factor is particularly important in failing hearts, which become highly dilated and have an abnormally large radius. The degree of curvature in any hollow chamber, including the heart, affects the relationship between wall tension and internal pressure. This relationship, described in [Subsection 2.7](#), states that for a hollow sphere, the internal pressure is proportional to the wall tension and inversely proportional to the internal radius.

As the radius of the ventricle increases, its curvature decreases, which means a smaller portion

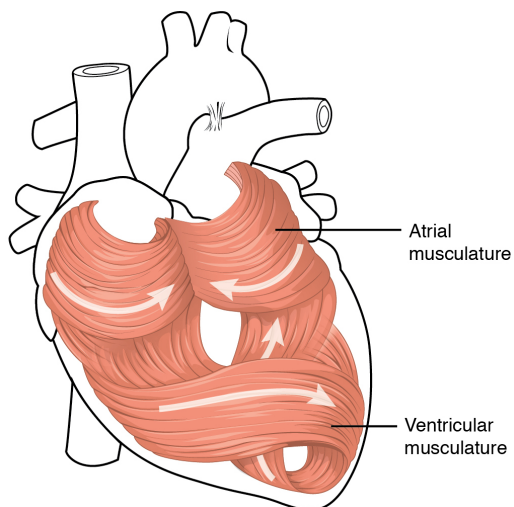


**Figure 1.2:** The swirling pattern of myocardium. Image attribution: OpenStax College, [Heart Musculature](#), CC BY 3.0.

of the wall tension is directed towards the cavity, resulting in less pressure generation. Thus, the curvature of the ventricular wall influences how effectively the active wall tension is converted into intraventricular pressure.

### Effects of Laplace's Law on Cardiac Performance and Ventricular Distension

Laplace's law impacts cardiac performance in several ways [16]. During the late phase of ejection, the decreasing chamber radius facilitates the process because the afterload, which is the resistance against which myocytes must shorten, falls as ejection proceeds. This phenomenon explains why ejection becomes easier as it continues and contributes to the peak of aortic pressure after the onset of ejection.

Ventricular distension has both advantages and disadvantages. The Frank-Starling mechanism and Laplace's law exert opposing effects on ventricular performance. While ventricular distension increases contraction force due to the Frank-Starling mechanism, it also reduces the pressure generated by a given contractile force because of Laplace's law. In a healthy heart, the increase in contractile energy from moderate distension outweighs the reduction in pressure-generating efficiency. However, in a grossly dilated, failing heart, the Laplace effect becomes dominant. Increased radius in such a heart does not significantly enhance contractile force but impairs systolic pressure generation and ejection.

### 2.3 Multiscale Aspects of Cardiovascular System

From molecular mechanisms to body functionality, each component of the cardiovascular system is intricately connected with biochemical and mechanical processes that occur across a wide range of spatial and temporal scales (see **Figure 1.3**) [18]. A comprehensive understanding of the multiscale properties is essential for successful modeling of these intrinsically multiscale phenomena. For instance, over long spatio-temporal scales, classical homogenization techniques have been effective in describing the dynamics of electrophysiological tissue properties. However, at smaller scales, these approaches may become ineffective.

For instance, the multiscale nature of heart function shares features with other biological systems, such as tissue growth, where a major challenge lies in linking macroscopic tissue-level descriptions with classical sub-cellular models (see the review [11]).

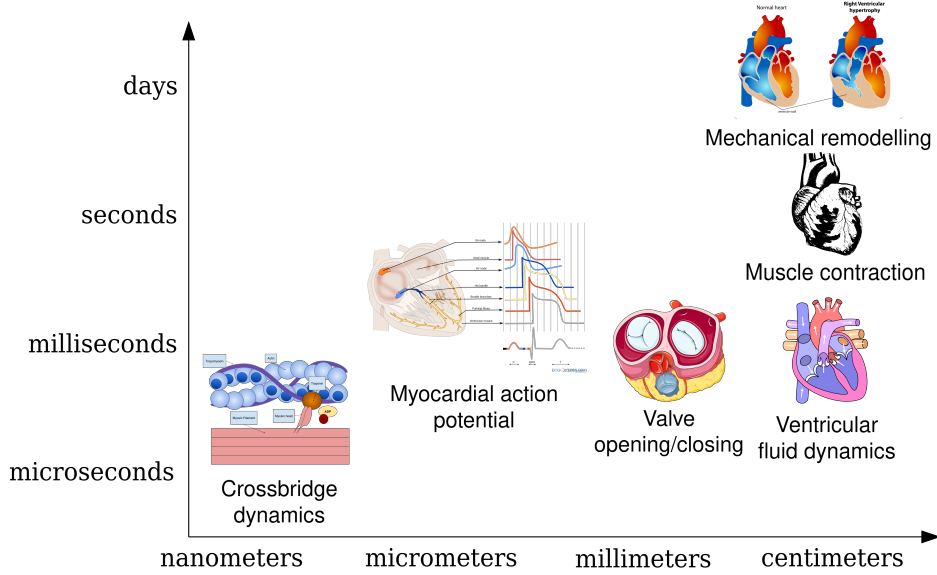


**Figure 1.3:** Spatial and temporal scales of mechanisms contributing to heart function. Inspired by [18]. Images attributions: [Erickzsierra](#), [Sliding Filament Theory](#), CC BY-SA 4.0; [ecgpedia](#), [Shapes of the cardiac action potential in the heart](#), CC BY-SA 3.0; [Laboratoires Servier](#), [Cardiovascular system - Valves 2](#), CC BY-SA 3.0; [Jerm](#), [Heart anterior exterior view](#), CC BY 2.5; [Wnauta](#), [Diagram of the human heart](#), CC BY-SA 3.0; [LadyofHats](#), [Right Ventricular hypertrophy](#), public domain.

## 2.4 Anatomy of the Sarcomere

### Structure of Human Cardiac Myocytes

The human cardiac myocyte (see [Figure 1.4](#)) is a cylindrical cell, approximately  $10\text{--}20\mu\text{m}$  wide and  $50\text{--}100\mu\text{m}$  long, with a single central nucleus and occasional branching [16]. Myocytes are connected end-to-end at intercalated discs, which contain gap junctions (intercellular channels that allow direct diffusion of ions) for electrical conduction and desmosomes (cell structures specialized for cell-to-cell adhesion) for mechanical strength.

The sarcomere, the fundamental contractile unit of the myocyte, is composed of long myofibrils packed within the cell. Each myofibril consists of sarcomeres aligned end-to-end, giving the cell its characteristic striped appearance. The resting length of a sarcomere is  $1.8\text{--}2.0\mu\text{m}$ . It contains thick myosin filaments and thin actin filaments, which overlap between the Z lines composed of  $\alpha$ -actinin.

### Myosin, Actin, and Regulatory Proteins in Cardiac Myocytes

Myosin filaments, located centrally in the sarcomere, form the A band, while actin filaments form the I band [16]. Actin filaments are anchored at the Z line and overlap with myosin filaments in the A band. The myosin molecule has a double-headed structure, essential for muscle contraction.

Regulatory proteins, tropomyosin and troponin, are attached to actin filaments and play a critical role in contraction initiation. Additionally, titin filaments run from Z line to Z line, providing elasticity and aligning myosin filaments. The transverse tubular system (T-tubules) invaginates at each Z line, allowing rapid transmission of electrical excitation into the cell, ensuring synchronized contraction of myofibrils.

## Mechanism of Cardiac Muscle Contraction

The contraction of the heart is driven by the shortening of sarcomeres through a sliding filament mechanism [16]. Actin filaments slide between myosin filaments, facilitated by the crossbridges formed by myosin heads, which act as independent force generators. This process is similar to rowing, with myosin heads repeatedly binding, rotating, and releasing actin filaments to produce movement. See also [Figure 1.5](#).

At rest, the binding sites on actin are blocked by tropomyosin. When the concentration of  $\text{Ca}^{2+}$  ions in the sarcoplasm rises,  $\text{Ca}^{2+}$  binds to troponin C, causing a shift that exposes the myosin-binding sites on actin. This allows the myosin heads to form crossbridges and initiate contraction. The movement of the myosin heads advances the actin filaments by 5 – 10 nm per cycle.

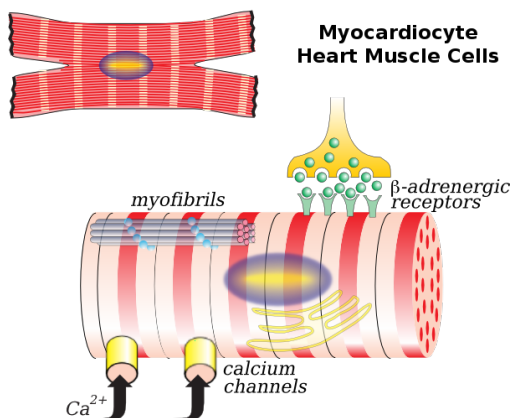


**Figure 1.4:** Illustration of a cardiac muscle cell. Image attribution: OCAL (OpenClipart), [Myocardiocyte](#), CC0 1.0.

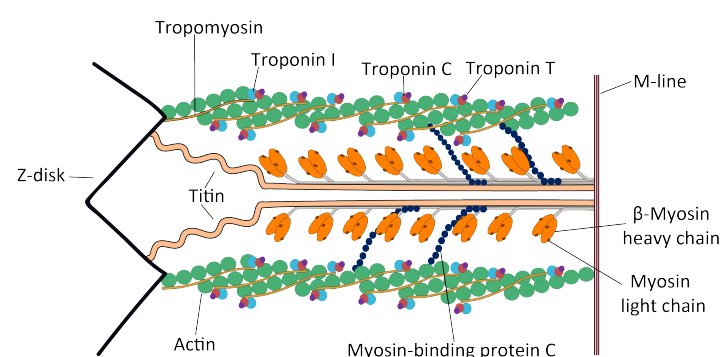


**Figure 1.5:** A diagram illustrating various components of cardiac sarcomere structure. Image attribution: Mohamed Elshennawy, M.D., [Cardiac sarcomere structure](#), CC BY-SA 4.0.

## 2.5 Structure and Function of the Pericardium

The pericardium is a fibroelastic sac which covers the heart from all sides except at the cardiac root (where the great vessels join the heart) and the bottom (where only the serous pericardium exists to cover the upper surface of the central tendon of diaphragm). The fibrous pericardium is semi-rigid, while the serous pericardium is flexible [5].

The same mesothelium, a thin layer of cells, that constitutes the serous pericardium also covers the heart as the epicardium, resulting in a continuous serous membrane that folds onto itself as two opposing surfaces, one over the fibrous pericardium and one over the heart. This creates a pouch-like space around the heart enclosed between the two opposing serosal surfaces, known as the pericardial space or pericardial cavity, which is filled with a small amount of serous fluid to lubricate the cardiac movements and cushions it from any external shock.

## 2.6 Anatomy of Heart Valves

### Heart Valves and Blood Flow Regulation

A heart valve is a biological one-way valve that allows blood to flow in one direction through the chambers of the heart [4]. Four cardiac valves are present in a mammalian heart and together they determine the pathway of blood flow through the heart. A heart valve opens or closes

according to differential blood pressure on each side.

The valves of the human heart can be grouped in two sets:

- ▷ Two atrioventricular valves to prevent backflow of blood from the ventricles into the atria:
  - ▷ Tricuspid valve or right atrioventricular valve, between the right atrium and right ventricle
  - ▷ Mitral valve or bicuspid valve, between the left atrium and left ventricle
- ▷ Two semilunar valves to prevent the backflow of blood into the ventricle:
  - ▷ Pulmonary valve, located at the opening between the right ventricle and the pulmonary trunk
  - ▷ Aortic valve, located at the opening between the left ventricle and the aorta.

The heart valves and the chambers are lined with the endocardium. Heart valves separate the atria from the ventricles, or the ventricles from a blood vessel. Heart valves are situated around the fibrous rings of the cardiac skeleton. The valves have flaps called leaflets that open to allow blood flow and then close to prevent backflow. The mitral valve has two cusps, whereas the others have three. There are nodules at the tips of the cusps that make the seal tighter.

### Function and Dynamics of Heart Valves During the Cardiac Cycle

During diastole, the mitral valve opens as a result of increased pressure from the left atrium as it fills with blood (preload) [12]. When atrial pressure increases above that of the left ventricle, the mitral valve opens. Opening facilitates the passive flow of blood into the left ventricle. Diastole ends with atrial contraction, ejecting the final 30% of blood from the left atrium to the left ventricle. This amount of blood is known as the end-diastolic volume (EDV), and the mitral valve closes at the end of atrial contraction to prevent a reversal of blood flow.

The tricuspid valve has three leaflets.

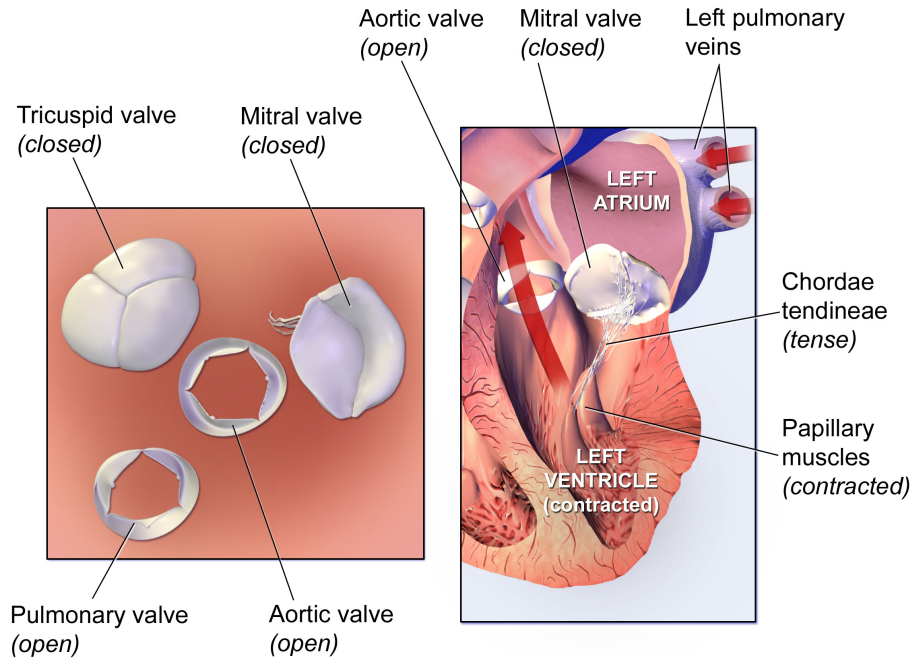
The aortic valve has three leaflets. During ventricular systole, pressure rises in the left ventricle and when it is greater than the pressure in the aorta, the aortic valve opens, allowing blood to exit the left ventricle into the aorta (see [Figure 1.6](#)). When ventricular systole ends, pressure in the left ventricle rapidly drops and the pressure in the aorta forces the aortic valve to close. The pulmonary valve has three leaflets. Similar to the aortic valve, the pulmonary valve opens in ventricular systole, when the pressure in the right ventricle rises above the pressure in the pulmonary artery [15]. At the end of ventricular systole, when the pressure in the right ventricle falls rapidly, the pressure in the pulmonary artery induces the closure of the pulmonary valve.

## 2.7 Mechanical Properties of Vessels in the Cardiovascular System

### Mechanical Factors Influencing the Radius of a Distensible Tube

The radius of a distensible tube is influenced by three mechanical factors [16]:

1. Internal pressure ( $P_i$ ) distending the tube.
2. External pressure ( $P_o$ ) compressing the tube.
3. Circumferential wall tension ( $T$ ), i.e. the force per unit length of the vessel.



## Valves of the Heart (Ventricles Contracting)

**Figure 1.6:** Illustration of the valves of the heart when the ventricles are contracting. Image attribution: [2], [Heart Ventricles Contract](#), CC BY 3.0

When the radius is at mechanical equilibrium, the circumferential wall tension balances the transmural pressure difference,  $P_i - P_o$ . According to Laplace's law for a thin-walled tube, the equilibrium wall tension is given by:

$$T = (P_i - P_o)r.$$

This implies that a larger vessel radius requires greater wall tension to counter a given transmural pressure difference. For example, wall tension is higher in the aorta than in smaller arteries with similar pressure, and capillary wall tension is very low.

Love's equation extends Laplace's law by considering wall thickness ( $w$ ), affecting wall stress ( $S$ ):

$$S = \frac{T}{w}$$

Thicker walls, like in the aorta, distribute the high wall tension among more cells and fibers, reducing individual stress. In contrast, capillaries have very thin walls ( $\sim 0.3\mu m$ ), leading to wall stress comparable to that in arteries despite lower blood pressure and wall tension. Notably, capillary wall stress in the human feet during standing can exceed the one in the aorta, showcasing the remarkable strength of capillary walls.

### Mechanisms of Vessel Wall Tension and Radius Adjustment

The total tension  $T$  in the vessel wall comprises two components: the passive tension from elastin and collagen fibrils, and the active tension exerted by smooth muscle cells. When the smooth muscle contracts, it immediately raises the wall tension  $T$ , causing a temporary mechanical disequilibrium. Consequently, the artery radius  $r$  begins to decrease. According to Laplace's law, if the transmural pressure remains constant while the radius  $r$  decreases, a new

mechanical equilibrium can only be attained by reducing the total wall tension  $T$ . This reduction is achieved by unloading the passive fibrils; as the vessel radius diminishes, the tension in the collagen and elastin fibers decreases. Essentially, there is a transfer of tension from the passive fibers to the active muscle cells, stabilizing the process of vasoconstriction.

Conversely, vasodilation occurs through smooth muscle relaxation. This relaxation reduces the active tension, leading to a temporary mechanical disequilibrium. The internal distending pressure then pushes the arterial wall outward, increasing the radius until the tension in the stretched collagen and elastin fibers re-establishes mechanical equilibrium.

## 2.8 Role of Peripheral Vasculature in Controlling Blood Flow

### Introduction to Blood Flow Regulation

Maintaining a constant high blood flow to all tissues at all times would be impractical, as it would far exceed the pumping capacity of the heart [16]. One of the fundamental principles of circulatory function is the ability of each tissue to regulate its own local blood flow according to its metabolic needs. This regulation is essential for delivering oxygen and nutrients and for removing waste products such as carbon dioxide and hydrogen ions. Additionally, it helps maintain proper concentrations of other ions within the tissues and facilitates the transport of various hormones and other substances.

### Vascular Tone and Its Regulation

The peripheral vasculature plays a crucial role in regulating blood flow through the tension exerted by vascular smooth muscle, known as vascular tone. Vascular tone controls the diameter of resistance vessels, thus influencing blood flow [8]. Increased vascular tone causes vasoconstriction, reducing local blood flow, while decreased tone leads to vasodilatation, allowing the vessel to expand under blood pressure. Basal vascular tone is particularly high in tissues such as skeletal muscle, enabling significant increases in blood flow (hyperemia) when needed. Vascular tone adjusts regional blood flow, arterial blood pressure, capillary filtration rate, and central venous pressure. These adjustments ensure tissues receive adequate blood supply for functions like temperature regulation, exercise, and secretion.

### Autoregulation of Blood Flow

Blood flow increases with perfusion pressure up to a certain point, after which flow remains almost constant (the plateau) until the pressure exceeds approximately 160 mmHg [8]. Autoregulation, the phenomenon where blood flow remains stable despite changes in pressure, occurs because vascular resistance changes inversely with pressure. For instance, a rise in pressure triggers constriction in resistance vessels, preventing an increase in flow. Autoregulation is crucial for stabilizing blood flow to organs, such as the brain, amidst fluctuating arterial pressures.

## 2.9 Vascular distensibility

### Blood Vessels are Distensible

A valuable characteristic of the vascular system is that all blood vessels are distensible [8]. The distensible nature of the arteries allows them to accommodate the pulsatile output of the heart and to average out the pressure pulsations. This provides smooth, continuous flow of blood through the very small blood vessels of the tissues.

Veins are by far the most distensible vessels. Even slight increases in venous pressure cause the

veins to store 0.5 to 1.0 liter of extra blood. Therefore, the veins provide a reservoir function for storing large quantities of extra blood that can be called into use whenever required elsewhere in the circulation.

### Different Distensibility in Arteries and Veins

Anatomically, the walls of the arteries are far stronger than those of the veins [8]. Consequently, the veins, on average, are about eight times more distensible than the arteries. That is, a given increase in pressure causes about eight times as much increase in blood in a vein as in an artery of comparable size.

It usually is more important to know the total quantity of blood that can be stored in a given portion of the circulation for each  $mmHg$  pressure rise than to know the distensibilities of the individual vessels. This value is called the compliance of the respective vascular bed and is computed as:

$$\text{Vascular compliance} = \frac{\text{Increase in volume}}{\text{Increase in pressure}}. \quad (1.1)$$

The compliance of a systemic vein is about 24 times that of its corresponding artery because it is about 8 times as distensible and it has a volume about 3 times as great, hence from (1.1):  $8 \times 3 = 24$ .

## 2.10 The Role of Arteries in the Cardiovascular System

### Arterial Pressure Pulsations

With each beat of the heart a new surge of blood fills the arteries [8]. Were it not for distensibility of the arterial system, all of this new blood would have to flow through the peripheral blood vessels almost instantaneously, only during cardiac systole, and no flow would occur during diastole. However, the compliance of the arterial tree normally reduces the pressure pulsations to almost no pulsations by the time the blood reaches the capillaries; therefore, tissue blood flow is mainly continuous with very little pulsation.

In general, the greater the stroke volume output, the greater the amount of blood that must be accommodated in the arterial tree with each heartbeat, and, therefore, the higher the pressure rise and fall during systole and diastole, thus causing a greater pulse pressure. Conversely, the lower the compliance of the arterial system, the greater the rise in pressure for a given stroke volume of blood pumped into the arteries.

### Transmission of Pressure Pulses to the Peripheral Arteries

When the heart ejects blood into the aorta during systole, at first only the proximal portion of the aorta becomes distended because the inertia of the blood prevents sudden blood movement all the way to the periphery [8]. However, the rising pressure in the proximal aorta rapidly overcomes this inertia, and the wavefront of distention spreads further and further along the aorta. This is called transmission of the pressure pulse in the arteries. The velocity of pressure pulse transmission in the normal aorta is 3 to 5  $m/s$ ; 7 to 10  $m/s$  in the large arterial branches; and 15 to 35  $m/s$  in the small arteries. In general, the greater the compliance of each vascular segment, the lower the velocity, which explains the slow transmission in the aorta and the much faster transmission in the much less compliant small distal arteries. In the aorta, the velocity of transmission of the pressure pulse is 15 or more times the velocity of blood because the pressure pulse is simply a moving wave of pressure that involves little forward total movement of blood volume.

### The Role of Elastic Arteries in Modulating Blood Pressure and Pulse Pressure

During systole, the ventricle rapidly ejects blood into the elastic arteries, primarily the aorta and subclavian vessels, causing them to expand and leading to a sharp increase in arterial pressure [16].

A significant portion of the stroke volume (67%–80%) is temporarily stored in these arteries, while the remainder flows through peripheral resistance. The elastic recoil of these arteries helps maintain blood pressure during diastole, known as the Windkessel effect.

As ejection slows, blood begins to flow out of the arteries faster than it is ejected, causing a decrease in arterial volume and pressure, eventually leading to the closure of the aortic valve. The pulse pressure, the difference between systolic and diastolic pressure, is influenced by stroke volume and arterial stiffness. Increased arterial stiffness, which can result from factors like higher mean pressure, increased ejection velocity, and aging, leads to higher pulse pressure.

### Pulse Transmission and Arterial Wall Stiffness

If arteries were rigid, blood pressure would rise instantly throughout the arterial system during systole [16]. However, because arteries are elastic, the pressure increase takes time to reach distal arteries like the radial artery.

In young individuals, the pulse travels at  $4 - 5 \text{ m/s}$ , while in older individuals, it reaches  $10 - 15 \text{ m/s}$ .

As blood is ejected into the proximal aorta, it creates space by both distending the arterial wall and pushing blood forward. This process repeats along the arterial tree, similar to a shock wave traveling down a line of train cars.

The pulse is transmitted as a wave of wall distension, while the actual blood moves much slower. Pulse transmission velocity increases with arterial stiffness, which rises with blood pressure and age, making pulse lag time a useful measure of arterial distensibility.

## 2.11 The Role of Veins in the Cardiovascular System

For years, veins were thought to be merely channels for blood flow to the heart. However, it is now clear that they play several critical roles in circulation [8]. Notably, veins can constrict and expand, allowing them to store varying amounts of blood and release it as needed to maintain proper circulation.

### Venous Pressure

Blood from all the systemic veins flows into the right atrium of the heart; therefore, the pressure in the right atrium is called the central venous pressure [8]. Right atrial pressure is regulated by a balance between the ability of the heart to pump blood out of the right atrium and ventricle into the lungs and the tendency for blood to flow from the peripheral veins into the right atrium. If the right heart is pumping strongly, the right atrial pressure decreases. Conversely, a heart with weakened musculature increases the pressure in the right atrium. Also, any effect that causes rapid inflow of blood into the right atrium from the peripheral veins has the same effect. Some factors that can increase venous return, and consequently raise right atrial pressure, include increased blood volume, elevated large vessel tone throughout the body leading to higher peripheral venous pressures, and dilation of the arterioles, which reduces peripheral resistance and allows rapid blood flow from the arteries into the veins.

The same factors that regulate right atrial pressure also contribute to the regulation of cardiac output, because the amount of blood pumped by the heart depends on both the ability of the heart to pump and the tendency for blood to flow into the heart from the peripheral vessels.

## Venous Resistance

Large veins have so little resistance to blood flow when they are distended that the resistance is almost of no importance [8]. However, most of the large veins that enter the thorax are compressed at many points by the surrounding tissues so that blood flow is impeded at these points. For instance, the veins from the arms are compressed by their sharp angulations over the first rib. Also, the pressure in the neck veins often falls so low that the atmospheric pressure on the outside of the neck causes these veins to collapse.

## Venous Valves

Were it not for valves in the veins, the gravitational pressure effect would cause the venous pressure in the feet always to be about 90 mmHg in a standing adult [8]. However, every time one moves the legs, one tightens the muscles and compresses the veins in or adjacent to the muscles, and this squeezes the blood out of the veins. But the valves in the veins are arranged so that the direction of venous blood flow can be only toward the heart. Consequently, every time a person moves the legs, a certain amount of venous blood is propelled toward the heart. This pumping system is known as the “venous pump” and it is efficient enough that under ordinary circumstances, the venous pressure in the feet of a walking adult remains less than 20mmHg.

## Blood Reservoir Function of the Veins

More than 60 percent of all the blood in the circulatory system is usually in the veins [8]. For this reason and also because the veins are so compliant, it is said that the venous system serves as a blood reservoir for the circulation.

During events such as hemorrhages, when blood is lost from the body and arterial pressure begins to fall, nervous signals are elicited from the carotid sinuses and other pressure-sensitive areas of the circulation. These in turn elicit nerve signals from the brain and spinal cord mainly through sympathetic nerves to the veins, causing them to constrict. This takes up much of the slack in the circulatory system caused by the lost blood. Indeed, even after as much as 20 percent of the total blood volume has been lost, the circulatory system often functions almost normally because of this variable reservoir function of the veins.

## Control of Cardiac Output by Venous Return

When one states that cardiac output is controlled by venous return, this means that it is not the heart itself that is normally the primary controller of cardiac output [8]. Instead, it is the various factors of the peripheral circulation that affect flow of blood into the heart from the veins, called venous return, that are the primary controllers.

The main reason why peripheral factors are usually more important than the heart itself in controlling cardiac output is that the heart has an inherent mechanism that automatically allows it to pump an amount of blood flows into the right atrium from the veins. This mechanism is called the Frank-Starling law of the heart. Basically, this law states that when increased quantities of blood flow into the heart, the increased blood stretches the walls of the heart chambers. As a result of the stretch, the cardiac muscle contracts with increased force, and this empties the extra blood that has entered from the systemic circulation.

Therefore, the blood that flows into the heart is automatically pumped without delay into the aorta and flows again through the circulation. Another important factor is that stretching the heart causes the heart to pump faster—at an increased heart rate. That is, stretch of the sinus node in the wall of the right atrium has a direct effect on the rhythmicity of the node itself to

increase heart rate as much as 10 to 15 percent.

The venous return to the heart is the sum of all the local blood flows through all the individual tissue segments of the peripheral circulation (see also [Subsection 2.8](#)).

### Decrease in Cardiac Output Caused by Decreased Venous Return

Anything that interferes with venous return also can lead to a decreased cardiac output [8]. Some of these factors are the following:

- ▷ Decreased blood volume.

By far, the most common non-cardiac peripheral factor that leads to a decreased cardiac output is a decreased blood volume, resulting most often from hemorrhage. It is clear why this condition decreases the cardiac output: loss of blood decreases the filling of the vascular system to such a low level that there is not enough blood in the peripheral vessels to create sufficiently high peripherall vascular pressure to push the blood back to the heart.

- ▷ Acute venous dilation.

On some occasions, the peripheral veins become acutely vasodilated. This results most often when the sympathetic nervous system suddenly becomes inactive. For instance, fainting often results from sudden loss of sympathetic nervous system activity, which causes the peripheral capacitative vessels, especially the veins, to dilate markedly. This decreases the filling pressure of the vascular system because the blood volume can no longer create adequate pressure in the now relaxed peripheral blood vessels. As a result, the blood “pools” in the vessels and does not return to the heart.

- ▷ Obstruction of the large veins.

On rare occasions, the large veins leading into the heart become obstructed, so the blood in the peripheral vessels cannot flow back into the heart. Consequently, the cardiac output falls markedly.

It should be noted that these factors are crucial for the calibration of a mathematical model. Efforts are made to control aspects such as those listed to ensure the overall dynamics function correctly.



# Bibliography

- [1] Christoph M. Augustin et al. “A computationally efficient physiologically comprehensive 3D–0D closed-loop model of the heart and circulation”. In: *Computer Methods in Applied Mechanics and Engineering* 386 (Dec. 2021), p. 114092. DOI: [10.1016/j.cma.2021.114092](https://doi.org/10.1016/j.cma.2021.114092).
- [2] Blausen. “Medical Gallery of Blausen Medical 2014”. In: *[[WikiJournal of Medicine—WikiJournal of Medicine]]* 1.2 (Aug. 29, 2014). DOI: [10.15347/WJM/2014.010](https://doi.org/10.15347/WJM/2014.010).
- [3] Piero Colli-Franzone et al. “Mathematical and numerical methods for reaction-diffusion models in electrocardiology”. In: *Modeling of Physiological Flows*. Springer Milan, 2012, pp. 107–141. DOI: [10.1007/978-88-470-1935-5\\_5](https://doi.org/10.1007/978-88-470-1935-5_5).
- [4] M. J. Curtis. “The Heart and Cardiovascular System”. In: *Cardiovascular Research* 26.7 (July 1992), 720b–720b. DOI: [10.1093/cvr/26.7.720b](https://doi.org/10.1093/cvr/26.7.720b).
- [5] William A. Newman Dorland. “Dorland’s Illustrated Medical Dictionary”. Dorland’s Medical Dictionary. ISBN: [9781455709854](https://doi.org/9781455709854). Elsevier Health Sciences, 2011.
- [6] TSE Eriksson et al. “Influence of myocardial fiber/sheet orientations on left ventricular mechanical contraction”. In: *Mathematics and Mechanics of Solids* 18.6 (May 2013), pp. 592–606. DOI: [10.1177/1081286513485779](https://doi.org/10.1177/1081286513485779).
- [7] Flavio Fenton et al. “Cardiac arrhythmia”. In: *Scholarpedia* 3.7 (2008), p. 1665. DOI: [10.4249/scholarpedia.1665](https://doi.org/10.4249/scholarpedia.1665).
- [8] Arthur C. Guyton et al. “Textbook of Medical Physiology”. ISBN: [978-0-7216-0240-0](https://doi.org/978-0-7216-0240-0). Elsevier Saunders, 2006. 1160 pp.
- [9] Maarten H. G. Heusinkveld et al. “Large vessels as a tree of transmission lines incorporated in the CircAdapt whole-heart model: A computational tool to examine heart-vessel interaction”. In: *PLOS Computational Biology* 15.7 (July 2019). Ed. by Alison Marsden, e1007173. DOI: [10.1371/journal.pcbi.1007173](https://doi.org/10.1371/journal.pcbi.1007173).
- [10] Siew Yen Ho et al. “Atrial structure and fibres: morphologic bases of atrial conduction”. In: *Cardiovascular Research* 54.2 (May 2002), pp. 325–336. DOI: [10.1016/S0008-6363\(02\)00226-2](https://doi.org/10.1016/S0008-6363(02)00226-2).
- [11] Gareth Wyn Jones et al. “Modeling growth in biological materials”. en. In: *SIAM Rev. Soc. Ind. Appl. Math.* 54.1 (Jan. 2012), pp. 52–118. DOI: <https://doi.org/10.1137/080731785>.
- [12] Agata Krawczyk-Ozog et al. “Anatomy of the mitral subvalvular apparatus”. In: *The Journal of Thoracic and Cardiovascular Surgery* 155.5 (May 2018), pp. 2002–2010. DOI: [10.1016/j.jtcvs.2017.12.061](https://doi.org/10.1016/j.jtcvs.2017.12.061).
- [13] JOOST LUMENS et al. “MODELING VENTRICULAR INTERACTION: A MULTISCALE APPROACH FROM SARCOMERE MECHANICS TO CARDIOVASCULAR SYSTEM HEMODYNAMICS”. In: *Biocomputing 2008. WORLD SCIENTIFIC*, Dec. 2007, pp. 378–389. DOI: [10.1142/9789812776136\\_0037](https://doi.org/10.1142/9789812776136_0037).
- [14] Paul D. Morris et al. “Computational fluid dynamics modelling in cardiovascular medicine”. In: *Heart* 102 (2015), pp. 18–28. DOI: [10.1136/heartjnl-2015-308044](https://doi.org/10.1136/heartjnl-2015-308044).
- [15] S Nazari et al. “Patterns of systolic stress distribution on mitral valve anterior leaflet chordal apparatus. A structural mechanical theoretical analysis”. In: *J Cardiovasc Surg (Torino)* 41.2 (2000). PMID: [10901521](https://pubmed.ncbi.nlm.nih.gov/10901521/), pp. 193–202.
- [16] David J. Paterson Neil Herring. “Levick’s Introduction to Cardiovascular Physiology, Sixth Edition”. Elsevier, 1991. DOI: [10.1016/c2013-0-06523-1](https://doi.org/10.1016/c2013-0-06523-1).
- [17] Charles S. Peskin. “Fiber architecture of the left ventricular wall: An asymptotic analysis”. In: *Communications on Pure and Applied Mathematics* 42.1 (Jan. 1989), pp. 79–113. DOI: [10.1002/cpa.3160420106](https://doi.org/10.1002/cpa.3160420106).
- [18] Alfio Quarteroni et al. “Integrated Heart—Coupling multiscale and multi-physics models for the simulation of the cardiac function”. In: *Computer Methods in Applied Mechanics and Engineering* 314 (Feb. 2017), pp. 345–407. DOI: [10.1016/j.cma.2016.05.031](https://doi.org/10.1016/j.cma.2016.05.031).
- [19] Gregory A. Roth et al. “Global Burden of Cardiovascular Diseases and Risk Factors, 1990–2019”. In: *Journal of the American College of Cardiology* 76 (2020), pp. 2982–3021. DOI: [10.1016/j.jacc.2020.11.010](https://doi.org/10.1016/j.jacc.2020.11.010).

- [20] K.S. Saladin. “**Anatomy & Physiology: The Unity of Form and Function**”. McGraw-Hill, 2012.
- [21] D.D. Streeter et al. “**Three dimensional fiber orientation in the mammalian left ventricular wall**”. In: *Cardiovascular System Dynamics*. Ed. by J. Baan et al. CRID: [10.1053/stcs.2001.29953](https://doi.org/10.1053/stcs.2001.29953). Cambridge: M.I.T. Press, 1978, pp. 73–84.
- [22] Fyodor A. Syomin et al. “**Multiscale simulation of the effects of atrioventricular block and valve diseases on heart performance**”. In: *International Journal for Numerical Methods in Biomedical Engineering* 35.7 (June 2019). DOI: [10.1002/cnm.3216](https://doi.org/10.1002/cnm.3216).
- [23] Francisco Torrent-Guasp et al. “**The Structure and Function of the Helical Heart and Its Buttress Wrapping. I. The Normal Macroscopic Structure of the Heart**”. In: *Seminars in Thoracic and Cardiovascular Surgery* 13.4 (Oct. 2001), pp. 301–319. DOI: [10.1053/stcs.2001.29953](https://doi.org/10.1053/stcs.2001.29953).
- [24] Francisco Torrent-Guasp et al. “**Towards new understanding of the heart structure and function**”. In: *European Journal of Cardio-Thoracic Surgery* 27.2 (Feb. 2005), pp. 191–201. DOI: [10.1016/j.ejcts.2004.11.026](https://doi.org/10.1016/j.ejcts.2004.11.026).
- [25] N. Townsend et al. “**Cardiovascular disease in Europe: epidemiological update 2016**.” In: *European heart journal* 37 42 (2016), pp. 3232–3245. DOI: [10.1093/eurheartj/ehw334](https://doi.org/10.1093/eurheartj/ehw334).

---

## The ADAVN model

---

## Contents of the chapter

---

1	Introduction	33
2	The Reduced ADAVN Model	34
2.1	Comprehensive Vascular Model Overview	34
2.2	Arterial-Venous Connectivity	35
3	The Mathematical Model	38
3.1	One-Dimensional Blood Flow Equations	38
3.2	The Tube Law of Arteries	38
3.3	The Tube Law of Veins	39
3.4	Conservation of Mass and Energy at Bifurcations and Junctions	39
3.5	Other Components of the Mathematical Model	39
3.6	Coupling Conditions	42
4	High-Order Finite Volume Solver for 1D Blood Flow Simulations	43
4.1	Introduction	43
4.2	The Mathematical Model [20]	43
4.3	Mathematical Reformulation: Well-Balancing and Hyperbolization [20]	44
4.4	Numerical Scheme	47
5	Boundary Conditions and Coupling Methods	54
5.1	Computation of Fluctuations Along Junctions	54
5.2	Ghost Cell Filling for Spatial Reconstruction	56
5.3	Prescribing Pressure or Flow and Coupling to Lumped Models	57

---

## 1 Introduction

In the scenario considered in this project, we are modeling blood flow in a network of vessels as the one shown in [Figure 2.1](#). Often, a blood vessel network will be truncated for various reasons:

- ▷ anatomical constraints;
- ▷ focus on a specific, limited part of the vascular network;
- ▷ limitations in extracting vessel network data from medical images;
- ▷ the computational cost or complexity of modeling extensive portions of the cardiovascular system.

After understanding that truncated vessel networks are commonly used, we can identify the types of boundary and coupling conditions necessary when working with blood vessel networks. A typical scenario involves prescribing a variable at a terminal point of the network ([Figure 2.1](#)). This occurs when available pressure or flow tracings, obtained through medical imaging, are set at an inlet or outlet point of the vessel network. In this context, we need to define appropriate boundary conditions at node  $V$  in [Figure 2.1](#). Another common situation involves coupling conditions at terminal network points (boundaries  $T_i$ , with  $i = 1, 2, 3$  in [Figure 2.1](#)). These are where one-dimensional vessels connect to lumped-parameter models, which describe peripheral circulation not included in the vessel network. Lastly, we discuss the coupling of multiple vessels at regions  $J_j$ , with  $j = 1, 2$ , in [Figure 2.1](#). This coupling point is somewhat artificial because we are dealing with one- or zero-dimensional models. If a 3D model is used, these coupling points would not require boundary conditions.

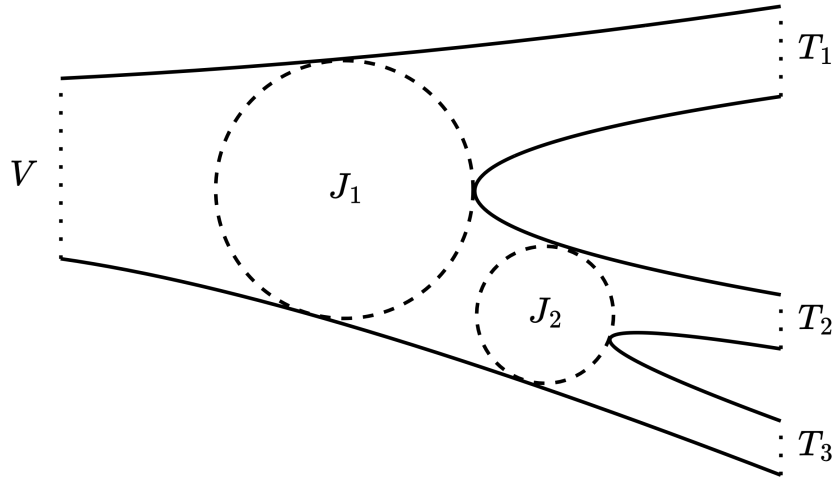


**Figure 2.1:** Schematic representation of a generic vessel network.  $V$  denotes a network location where a variable is to be prescribed,  $T_i$ , with  $i = 1, 2, 3$  correspond to terminal network points to be coupled to lumped-parameter models and  $J_i$ , with  $i = 1, 2$  represent bifurcation/junction regions [16].

Note that assuming a one-dimensional blood flow model allows us to shift from the scenario in [Figure 2.1](#) to that in [Figure 2.2](#), where we deal with one-dimensional domains. We aim to set boundary conditions at points like  $V$  and coupling conditions at points such as  $J_j$  or  $T_i$ .

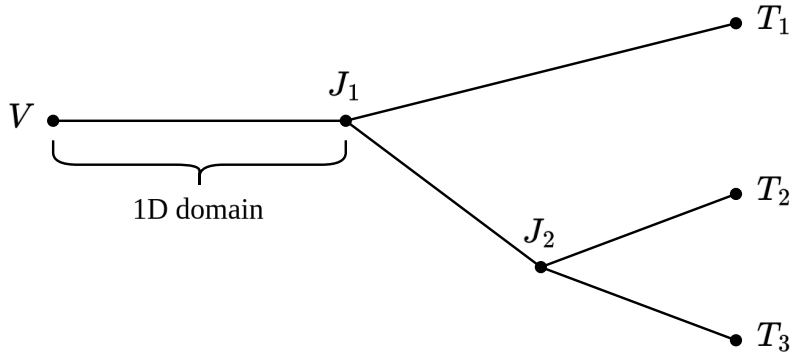


**Figure 2.2:** One-dimensional counterpart of the generic vessel network depicted in [Figure 2.1](#).  $V$  denotes a network location where a variable is to be prescribed,  $T_i$ , with  $i = 1, 2, 3$  correspond to terminal network points to be coupled to lumped-parameter models and  $J_i$ , with  $i = 1, 2$  represent bifurcation/junction points at which coupling conditions for multiple 1D domains have to be computed [16].

## 2 The Reduced ADAVN Model

In this work, we use a reduced version of the ADANV model [21]. The reduced version used here was developed by Caterina Dalmaso as part of her PhD thesis, and allows faster simulations, which is achieved by simplifying anatomical and physiological details without compromising the overall accuracy of the model. The model was calibrated by Caterina Dalmaso to reproduce as faithfully as possible the waveforms generated by the full ADANV model, particularly in regions proximal to the heart. Additionally, Caterina made significant modifications by adding veins and coronary arteries to the ADAN86 framework.

### 2.1 Comprehensive Vascular Model Overview

As shown in [Figure 2.3](#), the model includes:

- ▷ 86 primary systemic arteries and terminal arteries: these are identical to the vessels previously incorporated in the ADAN86 model [3];
- ▷ 23 coronary arteries: these additional vessels are consistent with those found in the full ADAVN model, representing a left-dominant vascular topology.
- ▷ 189 veins: these include the same vessels as the full ADAVN model, with 58 cerebral veins and 13 coronary veins (plus the coronary sinus). Veins containing valves and Starling resistors were automatically segmented to maintain the total vessel length, preserving the original count of 30 valves and 53 Starling resistors as in the ADAVN model.

The vessels are categorized into 61 anatomical regions. These regions are organized as follows:

- ▷ Head: Encephalon, brain, cerebellum, pons, dura mater, scalp, face, neck.
- ▷ Right upper limb: Right shoulder, right arm, right forearm, right hand.
- ▷ Left upper limb: Left shoulder, left arm, left forearm, left hand.
- ▷ Trunk: Aorta, aortic arch, thoracic aorta, abdominal aorta, chest, coronaries, right coronaries, left coronaries, sternum, abdomen, diaphragm, right suprarenal, left suprarenal,

liver, stomach, spleen, pancreas, right kidney, left kidney, intestine, dorsum, spinal, spinal cord, cervical spinal cord, thoracic spinal cord, lumbar spinal cord, lumbar region, cauda equina, pelvis.

- ▷ Right lower limb: Right gluteal region, right hip, right thigh, right knee, right leg, right foot.
- ▷ Left lower limb: Left gluteal region, left hip, left thigh, left knee, left leg, left foot.

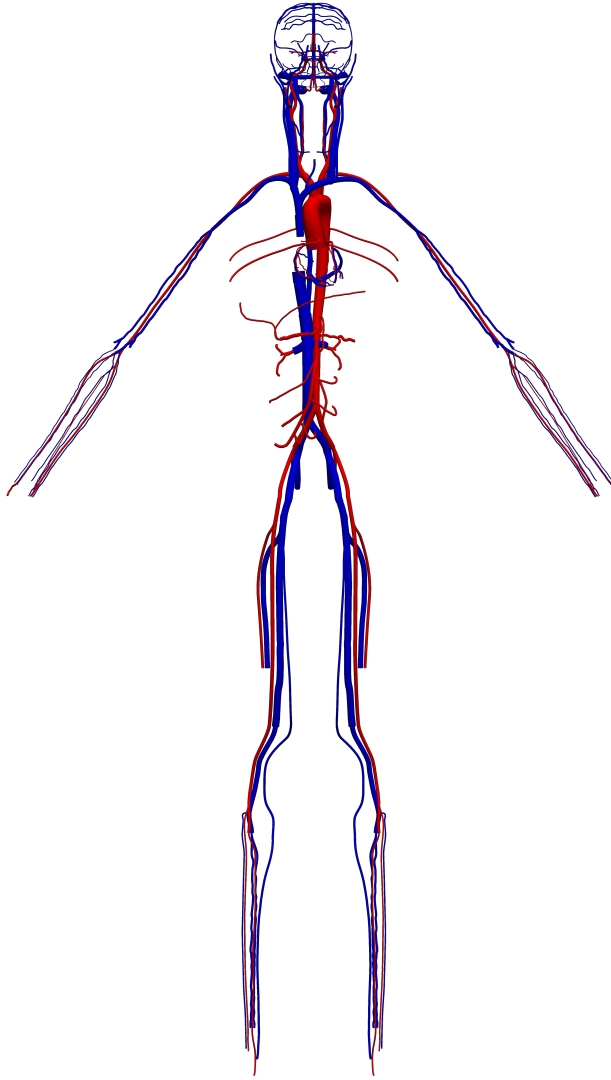


**Figure 2.3:** Full ADAVN vessel network: in red we depict arteries, in blue veins [4].

In contrast to the ADAVN model, this model maintains a complexity in the arterial system comparable to that of the venous system; therefore, the main difference is the reduction in the anatomical detail of the arterial system. A key distinction is that each terminal artery can connect to more than two terminal veins; for instance, in the head, a single artery may be connected to up to 11 veins. The coronary vessels remain identical in both models.

## 2.2 Arterial-Venous Connectivity

In this section, we outline the arterial-venous connectivity across different vascular districts, for a detailed description of the connections between veins and arteries see [Chapter 7](#). Similar to

the approach used in the ADAVN model, we operated under the following assumptions:

- ▷ Each terminal artery connects to an arterial bed, which in turn can connect to multiple veins. In this model, more than two veins can be connected to a single terminal artery (as seen in ADAVN86), while in the ADAVN model, this number was limited to two.
- ▷ Each terminal vein is connected to a venular bed, capable of receiving blood from multiple arteries.
- ▷ The establishment of connectivity was primarily based on the proximity of terminal arteries to terminal veins, striving to closely replicate the connectivity patterns defined in the ADAVN model.

Coronary vessels were excluded from this section, as their connectivity remains identical to that in the ADAVN model. Additionally, the liver was also excluded, given that only a single vein is present in this region.

### **Arterial System**

The arterial system explored in this study is a reduced version of the ADAN model [2]. This model was developed by using data derived from classic anatomical references [5] and depicts a typical male vascular anatomy. The creation process involved converting 2D vascular illustrations from [5] into a 3D model, utilizing a digital human skeleton as a structural framework. The model encompasses arteries identified in [15], adhering to established anatomical nomenclature.

To define the arterial vessels in three dimensions, cubic splines were employed using Autodesk 3ds Max (2010 version) with the digital skeleton as a base. The model includes nearly all arteries named according to anatomical conventions, resulting in a total of 1,598 identified arteries. Additionally, the model features perforating vessels that extend blood supply to peripheral regions. It integrates 28 specific organs (e.g., kidneys, liver, heart) along with 116 vascular territories, covering distributed organs such as muscles and skin.

### **Venous System**

The venous network in the ADAVN model comprises the largest veins found in the human body. In total, 189 veins are represented, responsible for draining blood from 66 vascular regions. Since the venous system is less detailed than the arterial system, most peripheral veins in the model are mapped to multiple vascular territories or organs, following the structure defined by the ADAN model. The delineation of the venous network followed the same methodology as the arterial system. Initially, only cerebral and coronary veins were fully included in the model, while the rest of the venous system was represented through the main vessels.

The great saphenous veins (GSVs) and the anterior and posterior tibial veins are responsible for draining the lower limbs, directing blood to the popliteal veins and subsequently to the femoral veins (FVs). The external iliac veins (EIVs) collect blood from the GSVs and FVs, merging with the internal iliac veins to form the common iliac veins, which then direct blood to the inferior vena cava (IVC). The IVC also channels blood from the splanchnic circulation towards the right atrium.

For the upper limbs, blood is drained by the radial, ulnar, and anterior interosseous veins, which converge into the brachial veins. These, in turn, flow into the axillary vein and the subclavian veins (SVs). The SVs, along with the external jugular vein (EJV), internal jugular vein (IJV), and vertebral vein (VV), carry blood to the brachiocephalic veins (BrVs). The left BrV also collects blood from the thyroid regions via the inferior thyroid vein.

### Cerebral and Coronary Veins

The cerebral veins play a critical role in draining blood from the brain. The ADAVN model includes 58 cerebral veins, which cover cortical veins, deep veins such as the internal cerebral veins, Rosenthal veins, and ophthalmic veins. The superior sagittal sinus (SSS) drains blood from the medial and lateral parts of the cortex, covering the occipital, parietal, and prefrontal superior cerebral veins. Meanwhile, the inferior sagittal sinus (ISS) runs along the corpus callosum, channeling blood from the central brain areas.

The coronary veins directly drain blood from the heart into the right atrium. The model represents 13 coronary veins along with the coronary sinus. The coronary sinus gathers blood from smaller veins of the heart, including the posterior interventricular vein, the left ventricular vein, the oblique vein of the left atrium, and the great cardiac vein (GCV). The small cardiac vein (SCV) collects blood from various right heart veins such as the anterior vein of the right ventricle, along with other marginal, atrial, and ventricular veins.

### Arterial-Venous Connectivity

The following criteria and hypotheses were established to define the connectivity between arterial and venous peripheral beds:

- Each terminal artery is linked to an arteriolar bed, which can then connect to multiple venous beds.
- Similarly, each terminal vein is connected to a venular bed, capable of receiving blood from various arterial beds.
- Connectivity was determined based on established knowledge of tributary and emissary vessels within vascular territories, particularly in the brain circulation and coronary circulation. In cases where specific information was unavailable, connectivity was inferred based on the proximity of terminal arteries to terminal veins.
- The interaction between arteriolar and venular beds is modeled as a purely resistive element to represent capillary resistance.

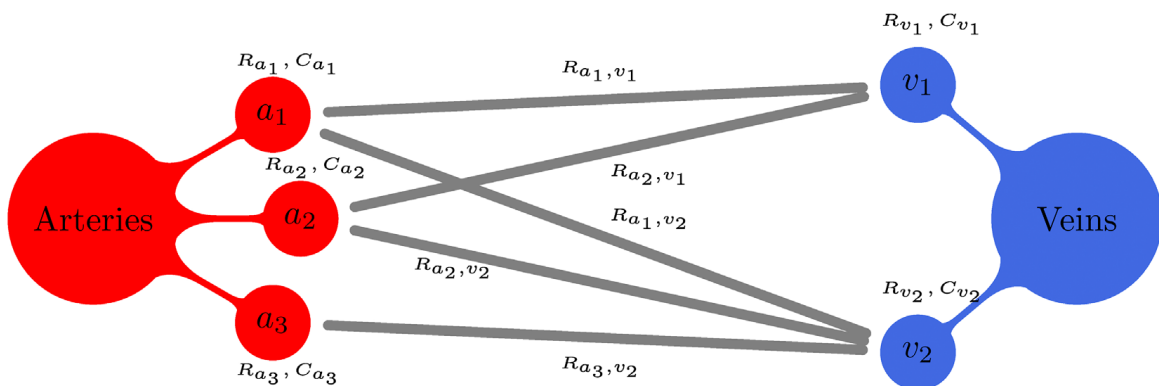


**Figure 2.4:** Schematic illustration for a generic peripheral circulation model in ADAVN. Terminal arteries  $a_i$ ,  $i = 1, 2, 3$ , give rise to three arteriolar/capillary compartments (with corresponding compliances  $C_{a_i}$  and proximal resistances  $R_{a_i}$ ). On the other hand, terminal veins  $v_j$ ,  $j = 1, 2$ , define two venous compartments (with corresponding compliances  $C_{v_j}$  and proximal resistances  $R_{v_j}$ ). Moreover, arterio-venous connections define arterio-venous resistances  $R_{a_i,v_j}$ . Image adapted from [21] with permission from the corresponding author.

Consider the connectivity model depicted in [Figure 2.4](#), which includes three terminal arteriolar districts ( $a_1, a_2, a_3$ ) and two terminal venular districts ( $v_1$  and  $v_2$ ). The model presents the following:

- Arteriolar bed  $a_1$  supplies venular beds  $v_1$  and  $v_2$  with corresponding capillary resistances  $R_{a_1,v_1}$  and  $R_{a_1,v_2}$ .
- Arteriolar bed  $a_2$  also connects to venular beds  $v_1$  and  $v_2$ , with corresponding capillary resistances  $R_{a_2,v_1}$  and  $R_{a_2,v_2}$ .
- Arteriolar bed  $a_3$  supplies venular bed  $v_2$ , with a corresponding capillary resistance  $R_{a_3,v_2}$ .

Consequently, in this model:

- Venular bed  $v_1$  receives blood from arteriolar beds  $a_1$  and  $a_2$ .
- Venular bed  $v_2$  receives blood from arteriolar beds  $a_1, a_2$ , and  $a_3$ .

The complete definition of the connectivity pattern for all terminal arteries and venous vessels is detailed in the accompanying sections.

## 3 The Mathematical Model

### 3.1 One-Dimensional Blood Flow Equations

Classical one-dimensional blood flow equations describe the evolution of lumen area  $A$ , flow rate  $q$ , and pressure  $p$  in space and time as:

$$\begin{cases} \partial_t A + \partial_x q = 0, \\ \partial_t q + \partial_x \left( \frac{q^2}{A} \right) + A \partial_x p = -\frac{f}{\rho}, \end{cases} \quad (2.1)$$

where  $f(x, t) = 8\pi\mu\frac{q}{A}$  is the friction force per unit length for a Poiseuille flow profile,  $\mu$  is the fluid viscosity, and  $\rho$  is the fluid density. The first equation represents mass conservation, while the second describes momentum balance. The relationship between pressure, wall strain, and strain rate is given by:

$$p(x, t) = p_{\text{ext}}(x, t) + p_{\text{tm}}(x, t). \quad (2.2)$$

Here,  $p_{\text{ext}}(x, t)$  accounts for external pressure exerted by surrounding tissues or fluids, while  $p_{\text{tm}}$  represents the transmural pressure, i.e., the stress-supported pressure within the vessel wall. This pressure,  $p_{\text{tm}}$ , differs between arteries and veins.

### 3.2 The Tube Law of Arteries

For arteries, the following tube law is employed:

$$p_{\text{tm}}^{\text{art}} = \frac{\pi R_0 h_0}{A} \left[ E_e \epsilon + E_c \epsilon_r \ln(e^\chi + 1) + \frac{K_m^{\text{art}}}{2\sqrt{AA_0}} \frac{\partial A}{\partial t} \right] + p_0^{\text{art}}, \quad (2.3)$$

where  $R_0 = R_0(x)$  is the vessel radius at a reference state,  $A_0 = A_0(x)$  is the cross-sectional area,  $h_0 = h_0(x)$  is the wall thickness,  $E_e = E_e(x)$  and  $E_c = E_c(x)$  are the effective Young's moduli of elastin and collagen fibers respectively, and  $K_m$  is the viscoelastic parameter. Furthermore, the deformation state  $\chi$  is given by:

$$\chi = \frac{\epsilon - \epsilon_0}{\epsilon_r}, \quad (2.4)$$

where  $\epsilon_0 = \epsilon_0(A_0)$  is the deformation state for which 50% of collagen fibers are activated,  $\epsilon_r = \epsilon_r(A_0)$  is the standard deviation of fiber activation, and  $\epsilon = \epsilon(A, A_0)$  is the current deformation state, defined as:

$$\epsilon = \sqrt{\frac{A}{A_0}} - 1. \quad (2.5)$$

### 3.3 The Tube Law of Veins

For veins, we utilize a tube law tailored for collapsible tubes, which has been employed in models that offer a 1D description of the venous system [24]. Specifically, the law is expressed as:

$$p_{tm}^{ven} = K \left[ \left( \frac{A}{A_0} \right)^m - \left( \frac{A}{A_0} \right)^n \right] + \frac{K_m}{A_0 \sqrt{A}} \frac{\partial A}{\partial t} + p_0^{ven}, \quad (2.6)$$

where  $K$  represents the effective stiffness of the vessel wall,  $m = 10$  and  $n = -3/2$  are coefficients responsible for characterizing the passive stiffening and collapse of the vessel.

### 3.4 Conservation of Mass and Energy at Bifurcations and Junctions

At vessel junctions and bifurcations, conservation of mass and energy is enforced through:

$$\sum_{k=1}^{N_p} g_k q_k = 0, \quad (2.7)$$

$$p_1 + \frac{1}{2} \rho u_1^2 = p_k + \frac{1}{2} \rho u_k^2, \quad k = 2, \dots, N_p, \quad (2.8)$$

where  $N_p$  is the number of vessels converging at a junction, and  $g_k = 1$  if the  $k$ -vessel shares an outlet node with the junction, while  $g_k = -1$  if the shared node is an inlet,  $u_1$  is the velocity in the first vessel at the bifurcation or junction, and  $u_k$  refers to the velocities in the other vessels involved. (2.7) ensures mass conservation, requiring no net change in mass at the junction, while (2.8) imposes continuity of total pressure. Satisfying both conditions ensures energy conservation, as the energy flux equals the product of flow rate  $q$  and total pressure  $p + \frac{1}{2} \rho u^2$ .

### 3.5 Other Components of the Mathematical Model

The following section outlines additional mathematical aspects of the model employed. Since these details are not central to the main objectives of this thesis, they are presented in a sequential manner without extensive elaboration. The goal is to provide a concise overview while maintaining focus on the primary contributions of the research.

#### Peripheral Beds

In the current model, there is no one-to-one correspondence between arterial and venous terminals in one-dimensional networks.

Peripheral circulation is divided into two compartments: a proximal compartment (associated with arteriolar/capillary circulation) and a distal compartment (associated with venules/small veins). Due to this modeling choice, each terminal artery is linked to a proximal compartment, which in turn connects to  $N_{ven}^\theta$  distal compartments. Similarly, each terminal vein is linked to a distal compartment, which connects to  $N_{art}^\theta$  proximal compartments. This configuration is illustrated in Figure 3, providing a specific example. The proximal compartment is connected to the distal compartment via a proximal resistance  $R_a$ . The distal compartment is then connected to the corresponding terminal vein via a distal resistance  $R_v$ , and the two compartments

are connected by a resistance  $R_{a,v}$ .

Peripheral circulation is modeled as a series of elastic compartments capable of storing blood and dissipating energy through friction, utilizing standard RCR lumped parameter models. In such models, pressure is expressed as a linear function of volume:

$$p_\theta = \frac{V_\theta}{C_\theta} + p_{\text{ext},\theta}, \quad (2.9)$$

where  $C_\theta$  is the compliance of compartment  $\theta$ ,  $p_{\text{ext},\theta}$  is the external pressure acting on this compartment, and  $V_\theta$  is the volume of the compartment. The rate of change of  $V_\theta$  over time is defined by the principle of mass conservation:

$$\dot{V}_\theta = q_{\text{in},\theta} - q_{\text{out},\theta}. \quad (2.10)$$

For proximal compartments,  $q_{\text{in},a_i}$  is computed by enforcing mass and energy conservation at the interface between the one-dimensional terminal artery outlet and the lumped-parameter model. The same applies for  $q_{\text{out},v_j}$ , which is calculated by applying coupling conditions that ensure mass conservation and momentum balance at the interface between the terminal vein inlet and the lumped parameter model. The flow leaving proximal arterial compartments is computed as:

$$q_{\text{out},a_i} = \sum_{l=1}^{N_{\text{ven},i}} \frac{p_{a_i} - p_{v_l}}{R_{a_i,v_l}}. \quad (2.11)$$

In turn, the flow entering a venous compartment is computed as:

$$q_{\text{in},v_j} = \sum_{l=1}^{N_{\text{art},j}} \frac{p_{a_l} - p_{v_j}}{R_{a_l,v_j}}. \quad (2.12)$$

## Coronary Beds

The method for defining the arterio-venous connections within the coronary peripheral beds follows the same principles outlined earlier. However, the mathematical model implemented here has been adapted to capture the unique characteristics of blood flow dynamics within the cardiac microcirculation. In this context, rather than using a simple resistance  $R_{a,v}$  to connect the proximal and distal compartments, the circuit illustrated in [25] is employed.

In practical terms, the peripheral vascular bed is conceptualized as being divided into three distinct layers: the sub-epicardium, the midwall, and the sub-endocardium. Each of these layers is further divided into two regions, each possessing its own compliance and corresponding volume. Additionally, each layer incorporates three variable resistances, which are dependent on the volume of the respective compartment region and are influenced by the intramyocardial pressure. As outlined by [25], the volumes for each layer of a given compartment are determined by:

$$V_{i,\lambda} = V_{i,\lambda}^0 + C_{i,\lambda} p_{i,\lambda}^{\text{tm}}, \quad (2.13)$$

where the volume  $V_{i,\lambda}$  for each region of the myocardium is calculated. According to [25], the Coronary Extravascular Pressure (CEP) is given by:

$$\text{CEP}_{\lambda,\phi} = p_{\text{out},\phi} + w_\lambda (p_{\text{ch},\phi} - p_{\text{out},\phi}), \quad (2.14)$$

where  $\phi$  represents regions such as the right atrium (RA), right ventricle (RV), left atrium (LA), left ventricle (LV), and interventricular septum (IVS). The weights  $w_\lambda$  for the sub-endocardium,

midwall, and sub-epicardium are 5/6, 1/2, and 1/6 respectively. For free walls, the pressure values  $p_{\text{out},\phi}$  are taken from the specific regions, and for the interventricular septum,  $p_{\text{out},\phi}$  is set to  $p_{\text{RV}}$ . Additionally, the chamber pressure  $p_{\text{ch},\phi}$  is the pressure within the chamber whose wall is perfused by the respective compartment. For the IVS, this is set to  $p_{\text{LV}}$ , while for free walls, the choice is straightforward.

Finally, the Subendocardial Ischemia Pressure (SIP) is defined as:

$$\text{SIP}_\phi = \alpha_{\text{SIP}} \left( \frac{p_{\text{ch},\phi}}{V_{\text{ch},\phi} - V_{\text{ch},\phi}^0} \right), \quad (2.15)$$

with  $\alpha_{\text{SIP}} = 8.2$ , and the chamber is selected similarly to how it is chosen for CEP calculations. Each coronary vascular territory includes nine resistances denoted as  $R_{i,\lambda}^j$ , with  $i \in \{1, m, 2\}$  and  $\lambda \in \{\text{sub-epi, midwall, sub-endo}\}$ . The relationship between resistance and volume, as proposed by [25], is as follows:

$$R_\lambda^j = R_{\lambda,0}^j \left( \frac{V_{\lambda,0}^j}{V_\lambda^j} \right)^2, \quad (2.16)$$

where  $R_{\lambda,0}^j$  is the nominal resistance for a reference volume  $V_{\lambda,0}^j$ . The resistance for the midwall  $R_\lambda^m$  is defined as:

$$R_\lambda^m = R_{\lambda,0}^m \left[ \frac{3}{4} \left( \frac{V_{\lambda,0}^1}{V_\lambda^1} \right)^2 + \frac{1}{4} \left( \frac{V_{\lambda,0}^2}{V_\lambda^2} \right)^2 \right], \quad (2.17)$$

where  $V_\lambda^j$  and  $V_\lambda^m$  are compartment volumes corresponding to zero transmural pressure.

### Intracranial Pressure

To account for the interaction between cerebral vasculature and intracranial pressure (ICP), the model developed by [29] has been adopted. It is important to note that this model was initially integrated with a one-dimensional representation of the arterial and venous circulatory systems. The rate of change of intracranial pressure over time is expressed as:

$$\dot{p}_{\text{ICP}} = \frac{1}{C_{\text{ICP}}} \left( \dot{V}_{\text{cbv}} + q_{\text{gen}} - q_{\text{abs}} \right), \quad (2.18)$$

where  $V_{\text{cbv}}$  represents the cerebral blood volume,  $q_{\text{gen}}$  and  $q_{\text{abs}}$  denote the generation and absorption rates of cerebrospinal fluid respectively, and  $C_{\text{ICP}}$  is the compliance of the cranio-spinal cavity, defined by:

$$C_{\text{ICP}} = \frac{1}{k_{\text{ICP}} p_{\text{ICP}}}, \quad (2.19)$$

with  $k_{\text{ICP}}$  being an experimentally determined coefficient. In this study, since pathological changes to the baseline state are not considered,  $q_{\text{gen}}$  is assumed to equal  $q_{\text{abs}}$ .

### Starling Resistors

It is essential to incorporate specific non-linear resistances near the junction where intracranial veins connect to dural sinuses. These non-linear resistances, known as Starling resistors (SR), provide a mechanism that decouples downstream hemodynamic conditions from the state of the intracranial veins, particularly when the pressure in the dural sinuses is lower than the intracranial pressure. We adopt a model based on the valve model proposed by [25]. Starling resistors are implemented as lumped parameter models positioned between two one-dimensional

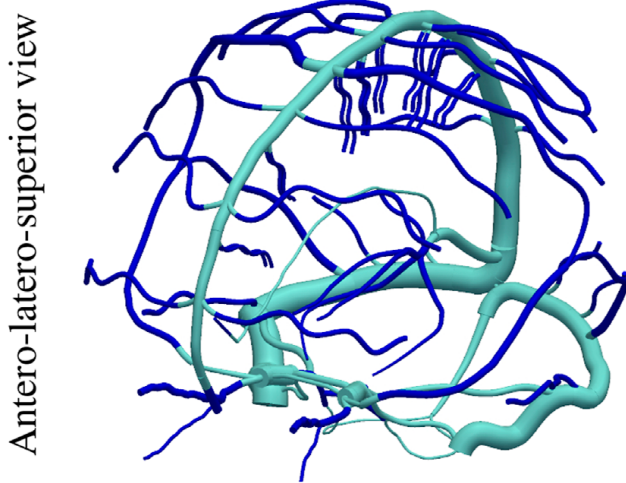


**Figure 2.5:** Position of Starling-resistor elements in the cerebral venous network, dividing the vascular network into intracranial cerebral veins (dark blue) and extracranial dural sinuses (light blue). Image adapted from [21] with permission from the corresponding author.

segments, specifically at the junction where intracranial veins meet dural sinuses (refer to [Figure 2.5](#)). The rate of change of flow through the SR is described by:

$$\dot{q}_\omega = \frac{1}{L_\omega} (p_{\text{up},\omega} - \dot{p}_{\text{down},\omega} - B_\omega q_\omega |q_\omega|), \quad (2.20)$$

where  $B_\omega$  and  $L_\omega$  are calculated as for valves (see [21]). While  $p_{\text{up},\omega}$  denotes the pressure in the upstream vessel, the downstream pressure is determined by:

$$\dot{p}_{\text{down},\omega} = (p_{\text{down},\omega} - p_{\text{ext},\omega}) \zeta_\omega + p_{\text{ext},\omega}, \quad (2.21)$$

which is dependent on the state of the SR, represented by  $\zeta_\omega$ . For an open SR, the downstream pressure is the pressure driving the flow across the SR, whereas for a closed or collapsed SR, the driving pressure is the external pressure, which, in the case of cerebral vessels, corresponds to the intracranial pressure. The rate of change of  $\zeta_\omega$  is defined as:

$$\zeta_\omega = \begin{cases} K_{\text{so},\omega} (1 - \zeta_\omega) \Delta p_\omega, & \text{if } \Delta p_\omega \geq 0, \\ K_{\text{sc},\omega} \zeta_\omega \Delta p_\omega, & \text{if } \Delta p_\omega < 0, \end{cases} \quad (2.22)$$

where  $K_{\text{so},\omega}$  and  $K_{\text{sc},\omega}$  are constants representing the SR's opening and closing dynamics, respectively. Additionally,  $\Delta p_\omega = p_{\text{down},\omega} - p_{\text{ext},\omega}$ .

### 3.6 Coupling Conditions

The coupling conditions outlined in (2.7) and (2.8) are not the only relationships used to connect one-dimensional domains at bifurcation or junction points. Additional coupling conditions are necessary, particularly those involving generalized Riemann invariants. These invariants are quantities preserved along the characteristics of hyperbolic systems of partial differential equations. They are employed to link one-dimensional domains to peripheral circulation models (such as those for terminal arteries and veins), the right atrium (for inferior and superior caval veins), and the aortic valve (for the ascending aorta). In all these scenarios, generalized Riemann invariants, along with other conditions that enforce mass and energy conservation at a discrete level, are utilized to compute the coupling conditions. These topics, along with a more detailed explanation of their significance and implementation, will be addressed further in [Section 5](#).

## 4 High-Order Finite Volume Solver for 1D Blood Flow Simulations

### 4.1 Introduction

The increasing complexity of vessel networks in one-dimensional blood flow models, driven by enhanced anatomical details and automated peripheral vasculature generation, has led to a pressing need for highly efficient numerical solvers.

This section presents the finite volume solver employed for the one-dimensional blood flow simulations based on the model described in this thesis, which is a reduced version of the model originally developed by Caterina Dalmaso (see [Chapter 2](#)). The solver offers high-order space-time accuracy and incorporates local time stepping (LTS).

The solver integrates three core components:

- ▷ a high-order finite volume numerical scheme,
- ▷ an advanced numerical solution treatment at network junctions,
- ▷ an accurate LTS strategy.

This methodology has been proposed and tested through empirical convergence tests in [\[20\]](#). In that work, the LTS scheme is also tested on arterial networks with varying levels of complexity and spatial scale heterogeneity, including one-dimensional segments ranging from a few tens to several thousands and vessel lengths from sub-millimeter to tens of centimeters, to evaluate its computational efficiency.

### 4.2 The Mathematical Model [\[20\]](#)

We will here reformulate the model in order to account for the geometrical and mechanical properties of arterial vessels, and we will perform a hyperbolic reformulation of the advection-diffusion-reaction equation.

#### One dimensional Blood Flow Model

For ease of reading, we restate system [\(2.1\)](#) here using a notation that will be useful in the subsequent discussion:

$$\begin{cases} \partial_t A + \partial_x q = 0, \\ \partial_t q + \partial_x \left( \hat{\alpha} \frac{q^2}{A} \right) + \frac{A}{\rho} \partial_x p = f. \end{cases} \quad (2.23)$$

Here, the coefficient  $\hat{\alpha}$  is a momentum correction factor related to the velocity profile used. In this context, we adopt  $\hat{\alpha} = 1$ . For a detailed discussion and various options for the velocity profile function  $s$ , see [\[14\]](#). For a Poiseuille flow, which refers to a fully-developed axisymmetric flow in a straight vessel, the friction force  $f$  is given by:

$$f = -8\pi \frac{\mu}{\rho} \frac{q}{A}. \quad (2.24)$$

#### Tube Law and Constitutive Law

To complete system [\(2.23\)](#), we incorporate a tube law that links  $p$  to  $A$  and other variables:

$$p(x, t) = p_r(x, t) + \zeta(x, t). \quad (2.25)$$

Here,  $p_r(x, t) = p_0 + \delta p_{\text{ext}}(x, t)$  represents a homeostatic equilibrium pressure  $p_0$ , with  $\delta p_{\text{ext}}(x, t)$  denoting fluctuations due to external tissues. As for the system (2.23), we restate the constitutive law using a similar notation, as:

$$\zeta(x, t) = \frac{\pi R_0 h_0}{A_d} \left[ E_e \left( \sqrt{\frac{A}{A_0}} - 1 \right) + E_c \epsilon_r \ln(e^{\chi(A)} + 1) + \frac{K_m}{2\sqrt{A A_0}} \partial_t A \right], \quad (2.26)$$

where  $R_0 = R_0(x)$  is the vessel radius in the reference state, linked to the reference cross-sectional area  $A_0 = A_0(x)$ , and  $h_0 = h_0(x)$  is the wall thickness at the reference state.  $E_e = E_e(x)$  and  $E_c = E_c(x)$  are the effective Young's modulus of elastin and collagen, respectively, while  $K_m$  is the effective viscoelastic parameter. The parameter  $A_d$  can be set to  $A_d = 3/4 A_0$  or alternatively  $A_d = A$ , depending on the desired constitutive model. The first choice yields a constitutive law which shows a linear dependence of the elastic component of pressure with respect to the vessel radius [1]; the second choice yields to a tube law that considers the incompressibility of the vessel wall, hence the reduction of wall thickness as the vessel wall is stretched [2].

It should be noted that while the constitutive model is presented here for the specific system in use, the numerical method implemented is designed to handle more generic tube laws. This flexibility allows the method to be applied to a wide range of constitutive models, beyond the specific cases presented here.

The expression of  $\chi = \chi(A)$  is:

$$\chi(A) = \frac{\epsilon(A) - \epsilon_0}{\epsilon_r}, \quad (2.27)$$

where  $\epsilon_0$  is the deformation state at which 50% of collagen fibers are activated,  $\epsilon_r$  is the standard deviation of the fiber activation state distribution, and  $\epsilon(A)$  is the current deformation state, given by:

$$\epsilon(A) = \sqrt{\frac{A}{A_0}} - 1. \quad (2.28)$$

We consider here the vessel wall composition in terms of elastin, collagen, and smooth muscle cells with the following relationships:

$$E_e = E_E W_E, \quad E_c = E_C W_C, \quad K_m = K_M W_M, \quad (2.29)$$

where  $E_E$  and  $E_C$  are the Young's modulus of elastin and collagen, respectively, and  $K_M$  is the viscoelastic parameter of smooth muscle cells. The terms  $W_E$ ,  $W_C$ , and  $W_M$  represent the fractions of elastin, collagen, and smooth muscle cells in the vessel wall.

### 4.3 Mathematical Reformulation: Well-Balancing and Hyperbolization [20]

Utilizing the mass conservation equation from (2.23), we can substitute the time derivative of  $A$  in (2.26) with the spatial derivative of the flow  $q$ . Furthermore, expanding the spatial derivative of pressure in the momentum equation from (2.23) yields a set of advection-diffusion-reaction equations. We then introduce an auxiliary variable  $\theta$  and a relaxation time  $T > 0$ , such that in the limit, the following holds:

$$\theta \rightarrow \partial_x q, \quad T \rightarrow 0 \quad (2.30)$$

by defining:

$$\partial_t \theta = \frac{1}{T} (\partial_x q - \theta). \quad (2.31)$$

Therefore,  $\zeta(x, t)$  becomes:

$$\zeta(x, t) = \frac{\pi R_0 h_0}{A_d} \left[ E_e \left( \sqrt{\frac{A}{A_0}} - 1 \right) + E_c \epsilon_r \ln(e^{\chi(A)} + 1) - \frac{K_m}{2\sqrt{AA_0}} \theta \right], \quad (2.32)$$

where we have replaced  $\partial_x q = \theta$ . This approximation introduces an error dependent on the relaxation time  $T$  (see [17] for more details), which provides criteria for selecting  $T$  to ensure the numerical scheme's accuracy for the original advection-diffusion-reaction system.

Parameters in (2.32) are spatially variable. Therefore, their spatial derivative is:

$$\partial_x \zeta = \zeta_A \partial_x A + \zeta_\theta \partial_x \theta + \zeta_{A_0} \partial_x A_0 + \zeta_{h_0} \partial_x h_0 + \zeta_{E_e} \partial_x E_e + \zeta_{E_c} \partial_x E_c + \partial_x p_r, \quad (2.33)$$

where  $\zeta_\alpha = \partial \zeta / \partial \alpha$  with  $\alpha = A, \theta, A_0, h_0, E_e, E_c$ . Spatially varying coefficients in  $\zeta$  lead to geometric source terms in the momentum balance equation. The development of explicit numerical schemes that accurately handle these source terms is a challenging task. In the following, we adopt the approach proposed in [28] for one-dimensional blood flow, applying it to system (2.23) with the tube law (2.32) in [18].

We consider the trivial evolution equations:

$$\partial_t \alpha = 0, \quad (2.34)$$

with  $\alpha = A_0, h_0, E_e, E_c$ , and:

$$\partial_t p_r = F(x, t), \quad (2.35)$$

where  $F(x, t)$  is prescribed. Then, we have:

$$\partial_t \mathbf{Q} + \mathbf{A}(\mathbf{Q}) \partial_x \mathbf{Q} = \mathbf{S}(\mathbf{Q}), \quad (2.36)$$

where the state vector is:

$$\mathbf{Q} = [A, q, \theta, A_0, h_0, E_e, E_c, p_r]^T, \quad (2.37)$$

and the coefficient matrix  $\mathbf{A}(\mathbf{Q})$  is:

$$\mathbf{A}(\mathbf{Q}) = \begin{pmatrix} 0 & 1 & 0 & 0 & 0 & 0 & 0 & 0 \\ c^2 - u^2 & 2u & \frac{A}{\rho} \zeta_\theta & \frac{A}{\rho} \zeta_{A_0} & \frac{A}{\rho} \zeta_{h_0} & \frac{A}{\rho} \zeta_{E_e} & \frac{A}{\rho} \zeta_{E_c} & \frac{A}{\rho} \\ 0 & -\frac{1}{T} & 0 & 0 & 0 & 0 & 0 & 0 \\ 0 & 0 & 0 & 0 & 0 & 0 & 0 & 0 \\ 0 & 0 & 0 & 0 & 0 & 0 & 0 & 0 \\ 0 & 0 & 0 & 0 & 0 & 0 & 0 & 0 \\ 0 & 0 & 0 & 0 & 0 & 0 & 0 & 0 \\ 0 & 0 & 0 & 0 & 0 & 0 & 0 & 0 \end{pmatrix}, \quad (2.38)$$

with  $c = \sqrt{\frac{A}{\rho} \zeta_A}$  and  $u = \frac{q}{A}$ .

The source vector  $\mathbf{S}(\mathbf{Q})$  is:

$$\mathbf{S}(\mathbf{Q}) = \left[ 0, f, -\frac{\theta}{T}, 0, 0, 0, 0, F \right]^T. \quad (2.39)$$

Full details of the eigenstructure of system (2.36) are provided in [22]. Here, only the necessary information for constructing the numerical scheme is presented. System (2.36) with coefficient matrix (2.38) is hyperbolic if:

$$\zeta_A - \frac{\zeta_\theta}{T} > 0, \quad (2.40)$$

with eigenvalues:

$$\lambda_1 = u - c_T, \quad \lambda_2 = \lambda_3 = \lambda_4 = \lambda_5 = \lambda_6 = \lambda_7 = 0, \quad \lambda_8 = u + c_T, \quad (2.41)$$

where:

$$c_T = \sqrt{c^2 - \frac{A\zeta_\theta}{\rho T}}, \quad (2.42)$$

and linearly independent eigenvectors.

Characteristic fields associated to  $\lambda_i$ , for  $i = 1, 8$ , have been shown to be genuinely nonlinear for physiological parameter and state variables ranges [20]. The Riemann invariants for the characteristic field associated to  $\lambda_1$  are:

$$\Gamma_1^1 = u + \int_{\hat{A}}^A \frac{\tilde{c}_T(\xi)}{\xi} d\xi, \quad \Gamma_1^2 = \theta + \frac{A}{T}, \quad \Gamma_1^3 = A_0, \quad \Gamma_1^4 = h_0, \quad \Gamma_1^5 = E_e, \quad \Gamma_1^6 = E_c, \quad \Gamma_1^7 = p_r, \quad (2.43)$$

with

$$\tilde{c}_T(A) = c_T(A, \tilde{\theta}(A)) \quad (2.44)$$

and

$$\tilde{\theta}(A) = \hat{\theta} + \frac{\hat{A} - A}{T}, \quad (2.45)$$

where  $\hat{A}$  and  $\hat{\theta}$  are reference values. Similarly, the Riemann invariants for the characteristic field associated to  $\lambda_8$  are:

$$\Gamma_8^1 = u - \int_{\hat{A}}^A \frac{\tilde{c}_T(\xi)}{\xi} d\xi, \quad \Gamma_8^2 = \theta + \frac{A}{T}, \quad \Gamma_8^3 = A_0, \quad \Gamma_8^4 = h_0, \quad \Gamma_8^5 = E_e, \quad \Gamma_8^6 = E_c, \quad \Gamma_8^7 = p_r. \quad (2.46)$$

Characteristic fields associated with  $\lambda_i$ , for  $i = 2, \dots, 7$ , are linearly degenerate. They correspond to a stationary contact discontinuity at  $x/t = 0$ , arising from changes in the parameters of  $\zeta$ . The Riemann invariants for these fields are:

$$\Gamma_1^{LD} = p + \frac{1}{2}\rho u^2 = \text{constant} \quad (2.47)$$

and

$$\Gamma_2^{LD} = q = \text{constant}. \quad (2.48)$$

System (2.36) is hyperbolic under appropriate assumptions, allowing the use of numerical schemes designed for hyperbolic PDEs. However, it is important to note that the relaxation time  $T$  can be small, causing the resulting source term to become stiff. Consequently, the numerical scheme selected to solve (2.36) must be capable of handling such source terms.

In [17] is indicated that to ensure the formulation error is smaller than the discretization error, the following relation must be satisfied:

$$\Delta := \frac{T}{(\Delta x)^p} \frac{1 - 2^{1-\frac{1}{2}}}{2^{p-\frac{1}{2}} - 1} = O(1), \quad (2.49)$$

where  $p$  is the order of accuracy of the numerical scheme, and  $\Delta x$  is the characteristic size of the computational cells.

## 4.4 Numerical Scheme

### Path-Conservative Numerical Scheme

The numerical scheme used falls under the category of path-conservative schemes [26]. Initially proposed in [11] for conservative systems, it was later adapted for non-conservative systems in [7, 12].

We begin by detailing the discretization of (2.36) within a single one-dimensional domain (vessel). For simplicity, we consider the domain corresponding to the  $j$ -th vessel and omit the index  $j$ , noting that all quantities defined here are local to the  $j$ -th vessel. This also applies to the time iteration index  $n = n_j$  due to the use of an LTS strategy. The dependence on  $n$  and other vessel-related quantities on  $j$  will only be highlighted when necessary for clarity.

The spatial domain is divided into computational cells  $T_i = [x_{i-\frac{1}{2}}, x_{i+\frac{1}{2}}]$ , with  $i = 1, \dots, N_j$ , where  $N_j$  represents the number of cells. To construct a finite volume-type scheme, we integrate (2.36) in space and time within the control volume  $V_i^n = [x_{i-\frac{1}{2}}, x_{i+\frac{1}{2}}] \times [t^n, t^{n+1}]$ , leading to:

$$\mathbf{Q}_i^{n+1} = \mathbf{Q}_i^n - \frac{1}{\Delta x_i} \int_{t^n}^{t^{n+1}} \int_{x_{i-\frac{1}{2}}}^{x_{i+\frac{1}{2}}} \mathbf{A}(\mathbf{Q}) \partial_x \mathbf{Q} dx dt - \frac{\Delta t^n}{\Delta x_i} \left( \mathbf{D}_{i+\frac{1}{2}}^- + \mathbf{D}_{i-\frac{1}{2}}^+ \right) + \Delta t^n \mathbf{S}_i, \quad (2.50)$$

where

$$\mathbf{Q}_i^n = \frac{1}{\Delta x_i} \int_{x_{i-\frac{1}{2}}}^{x_{i+\frac{1}{2}}} \mathbf{Q}(x, t^n) dx, \quad (2.51)$$

and

$$\mathbf{S}_i = \frac{1}{\Delta t^n \Delta x_i} \int_{t^n}^{t^{n+1}} \int_{x_{i-\frac{1}{2}}}^{x_{i+\frac{1}{2}}} \mathbf{S}(\mathbf{Q}(x, t)) dx dt \quad (2.52)$$

and

$$\mathbf{D}_{i+\frac{1}{2}}^\pm = \frac{1}{\Delta t^n} \int_{t^n}^{t^{n+1}} D_{i+\frac{1}{2}}^\pm \left( \mathbf{Q}_{i+\frac{1}{2}}^-(t), \mathbf{Q}_{i+\frac{1}{2}}^+(t), \Psi \left( \mathbf{Q}_{i+\frac{1}{2}}^-(t), \mathbf{Q}_{i+\frac{1}{2}}^+(t), s \right) \right) dt. \quad (2.53)$$

Here,  $\Delta x_i = x_{i+\frac{1}{2}} - x_{i-\frac{1}{2}}$ ,  $\Delta t^n = t^{n+1} - t^n$ , and  $\mathbf{Q}_{i+\frac{1}{2}}^\pm(t)$  are the locally evolved data at the cell interface,  $D_{i+\frac{1}{2}}^\pm \left( \mathbf{Q}_{i+\frac{1}{2}}^-(t), \mathbf{Q}_{i+\frac{1}{2}}^+(t), \Psi \left( \mathbf{Q}_{i+\frac{1}{2}}^-(t), \mathbf{Q}_{i+\frac{1}{2}}^+(t), s \right) \right)$  represents fluctuations, analogous to numerical fluxes in finite volume schemes for hyperbolic systems in conservative form. The path  $\Psi \left( \mathbf{Q}_{i+\frac{1}{2}}^-(t), \mathbf{Q}_{i+\frac{1}{2}}^+(t), s \right)$  is used to define these fluctuations.

To achieve a high-order numerical scheme, the integrals in (2.50) must be performed with high accuracy. The numerical scheme used belongs to a family of high-order schemes that perform three substeps at each local time step:

- ▷ Piecewise polynomial spatial reconstruction using current time data:  $\mathbf{Q}_i^n \rightarrow \mathbf{w}_i^n = \mathbf{w}_i(x, t^n)$ ,
- ▷ Local space-time prediction:  $\mathbf{w}_i(x, t^n) \rightarrow \mathbf{Q}_i^{ST}(x, t)$ ,
- ▷ Fully explicit data evolution:  $\mathbf{Q}_i^n \rightarrow \mathbf{Q}_i^{n+1}$ .

We now proceed with the description of each of these steps.

### First Order Fluctuations

Fluctuations in (2.53) result from solving a Riemann problem at the interfaces of computational cells. We use a modified Dumbser-Osher-Toro (DOT) Riemann solver [6], as proposed in [23].

In the DOT solver, fluctuations are computed as:

$$D_{i+\frac{1}{2}}^{\pm} = \frac{1}{2} \int_0^1 \left[ \mathbf{A} \left( \Psi \left( \mathbf{Q}_{i+\frac{1}{2}}^-, \mathbf{Q}_{i+\frac{1}{2}}^+, s \right) \right) \pm \left| \mathbf{A} \left( \Psi \left( \mathbf{Q}_{i+\frac{1}{2}}^-, \mathbf{Q}_{i+\frac{1}{2}}^+, s \right) \right) \right| \right] \frac{\partial \Psi}{\partial s} ds, \quad (2.54)$$

with the absolute value operator of a matrix defined as:

$$|\mathbf{A}| = \mathbf{R} |\Lambda| \mathbf{R}^{-1}, \quad |\Lambda| = \text{diag}(|\lambda_1|, |\lambda_2|, \dots, |\lambda_N|), \quad (2.55)$$

where  $\mathbf{R}$  is the matrix composed of the right eigenvectors of (2.38),  $\mathbf{R}^{-1}$  is its inverse, and  $N$  is the number of state variables in the underlying hyperbolic system of PDEs. The path  $\Psi = \Psi(\mathbf{Q}^-, \mathbf{Q}^+, s)$ , with  $0 \leq s \leq 1$ , is a Lipschitz continuous function connecting the left state  $\mathbf{Q}^-$  to the right state  $\mathbf{Q}^+$  in phase space, satisfying:

$$\Psi(\mathbf{Q}^-, \mathbf{Q}^+, 0) = \mathbf{Q}^-, \quad \Psi(\mathbf{Q}^-, \mathbf{Q}^+, 1) = \mathbf{Q}^+. \quad (2.56)$$

The path proposed in [6] is the segment path:

$$\Psi(\mathbf{Q}_{i+\frac{1}{2}}^-, \mathbf{Q}_{i+\frac{1}{2}}^+, s) = \mathbf{Q}_{i+\frac{1}{2}}^- + s \left( \mathbf{Q}_{i+\frac{1}{2}}^+ - \mathbf{Q}_{i+\frac{1}{2}}^- \right). \quad (2.57)$$

However, it was shown in [23] that for some problems, the path must be better characterized to obtain a well-balanced scheme, i.e., a scheme that accurately reproduces both steady and unsteady states. Following [23], we consider a path using the segment path for all variables except for the cross-sectional area  $A$ :

$$\Psi(\mathbf{Q}_{i+\frac{1}{2}}^-, \mathbf{Q}_{i+\frac{1}{2}}^+, s) = \begin{pmatrix} \underline{A}(s) \\ \underline{q}(s) \\ \underline{\theta}(s) \\ \underline{A}_0(s) \\ \underline{h}_0(s) \\ \underline{E}_e(s) \\ \underline{E}_c(s) \\ \underline{p}_r(s) \end{pmatrix} = \begin{pmatrix} \zeta(s)^{-1} \\ q_{i+\frac{1}{2}}^- + s(q_{i+\frac{1}{2}}^+ - q_{i+\frac{1}{2}}^-) \\ \theta_{i+\frac{1}{2}}^- + s(\theta_{i+\frac{1}{2}}^+ - \theta_{i+\frac{1}{2}}^-) \\ A_{0,i+\frac{1}{2}}^- + s(A_{0,i+\frac{1}{2}}^+ - A_{0,i+\frac{1}{2}}^-) \\ h_{0,i+\frac{1}{2}}^- + s(h_{0,i+\frac{1}{2}}^+ - h_{0,i+\frac{1}{2}}^-) \\ E_{e,i+\frac{1}{2}}^- + s(E_{e,i+\frac{1}{2}}^+ - E_{e,i+\frac{1}{2}}^-) \\ E_{c,i+\frac{1}{2}}^- + s(E_{c,i+\frac{1}{2}}^+ - E_{c,i+\frac{1}{2}}^-) \\ p_{r,i+\frac{1}{2}}^- + s(p_{r,i+\frac{1}{2}}^+ - p_{r,i+\frac{1}{2}}^-) \end{pmatrix}. \quad (2.58)$$

The path  $\underline{\zeta}(s)$  for relation (2.26) is defined as:

$$\underline{\zeta}(s) = \underline{\Gamma}(s) - \underline{p}_r(s), \quad (2.59)$$

where  $\underline{\Gamma}(s)$  is:

$$\underline{\Gamma}(s) = \tilde{\Gamma}_{1,i+\frac{1}{2}}^{LD,-} + s \left( \tilde{\Gamma}_{1,i+\frac{1}{2}}^{LD,+} - \tilde{\Gamma}_{1,i+\frac{1}{2}}^{LD,-} \right) \quad (2.60)$$

and

$$\tilde{\Gamma}_1^{LD} = p_r + \zeta_e, \quad (2.61)$$

with  $\zeta_e$  being equal to  $\zeta$  for  $K_m = 0$ .  $\tilde{\Gamma}_1^{LD}$  is in fact  $\Gamma_1^{LD}$  for  $q = 0 \forall x$ , which implies  $\theta = 0$ . Once  $\underline{\zeta}(s)$  is known, we compute  $\underline{A}(s)$  from (2.26) using a globally convergent Newton method.

Relations (2.59) and (2.60) ensure that the numerical scheme preserves stationary solutions exactly. In fact,  $\underline{\Gamma}(s)$  is constant for  $q = 0$  because:

$$\tilde{\Gamma}_{1,i+\frac{1}{2}}^{LD,+} = \tilde{\Gamma}_{1,i+\frac{1}{2}}^{LD,-}. \quad (2.62)$$

In this scenario, the resulting path parameterizes the integral curve that connects two states on either side of the stationary contact discontinuity (for more details see [23]). The integral in (2.54) for the DOT solver using path (2.58) is computed numerically and is given by:

$$D_{i+\frac{1}{2}}^{\pm} = \frac{1}{2} \sum_{c=1}^C \omega_c \left[ \mathbf{A} \left( \Psi \left( \mathbf{Q}_{i+\frac{1}{2}}^{-}, \mathbf{Q}_{i+\frac{1}{2}}^{+}, s_c \right) \right) \pm \left| \mathbf{A} \left( \Psi \left( \mathbf{Q}_{i+\frac{1}{2}}^{-}, \mathbf{Q}_{i+\frac{1}{2}}^{+}, s_c \right) \right) \right| \frac{\partial \Psi}{\partial s} \Big|_{s=s_c} \right], \quad (2.63)$$

where  $\omega_c$  and  $s_c$  are the  $c$ -th weight and coordinate of a Gaussian quadrature rule with  $C$  points. We use  $C = 3$  for all computations.

Note that, due to our choice for path (2.58), the vector  $\frac{\partial \Psi}{\partial s}$  cannot be taken out of the integral (2.54), as done when using the segment path (2.57) in [6]. Derivatives for most variables are straightforward, except for  $\underline{A}(s)$ , which is an implicit function of  $\zeta$ . Therefore, its derivative at each quadrature point  $s = s_c$  is computed as:

$$\begin{aligned} \frac{\partial \underline{A}}{\partial s}(s_c) &= \left[ \frac{\partial \zeta}{\partial s}(s_c) - \frac{\partial \zeta}{\partial \underline{A}_0} \Big|_{s=s_c} \frac{\partial \underline{A}_0}{\partial s}(s_c) - \frac{\partial \zeta}{\partial \underline{h}_0} \Big|_{s=s_c} \frac{\partial \underline{h}_0}{\partial s}(s_c) \right. \\ &\quad \left. - \frac{\partial \zeta}{\partial \underline{E}_e} \Big|_{s=s_c} \frac{\partial \underline{E}_e}{\partial s}(s_c) - \frac{\partial \zeta}{\partial \underline{E}_c} \Big|_{s=s_c} \frac{\partial \underline{E}_c}{\partial s}(s_c) \right] \left( \frac{\partial \zeta}{\partial \underline{A}} \Big|_{s=s_c} \right)^{-1}. \end{aligned} \quad (2.64)$$

### Piecewise Polynomial Spatial Reconstruction

To achieve high-order accurate spatial reconstruction, we employ the weighted essentially non-oscillatory methodology proposed in [10] and also discussed in [8]. Initially, we introduce reference coordinates  $0 \leq \xi \leq 1$  defined by  $x = x_{i-\frac{1}{2}} + \xi \Delta x_i$ . Working in a reference space, we use a generic reconstruction polynomial  $\mathbf{w}_h^n$  instead of the specific polynomial  $\mathbf{w}_i^n$ . For an order  $k$  scheme, at each time level  $t^n$ , we reconstruct element-wise polynomials of the type:

$$\mathbf{w}_h(\xi, t^n) = \sum_{l=1}^{M+1} \psi_l(\xi) \hat{\mathbf{w}}_l(t^n) = \psi_l(\xi) \hat{\mathbf{w}}_l(t^n), \quad (2.65)$$

where  $M = k - 1$  is the polynomial degree of the spatial reconstruction,  $\psi_l(\xi), l = 1, \dots, M+1$ , are the corresponding basis functions, and  $\hat{\mathbf{w}}_l(t^n), l = 1, \dots, M+1$ , are the expansion coefficients at time  $t = t^n$ . Note that we have introduced the Einstein summation convention, implying summation over repeated indices; this convention will be used for the rest of the dissertation. The spatial reconstruction is performed on a set of stencils defined as:

$$S_i^s = \bigcup_{e=i-L}^{i+R} T_e, \quad (2.66)$$

where  $L = L(M, s)$  and  $R = R(M, s)$  are the stencil extents to the left and right, respectively. For odd-order schemes, we use three stencils: a central stencil ( $s = 1, L = R = \frac{M}{2}$ ), a fully left-sided stencil ( $s = 2, L = M, R = 0$ ), and a fully right-sided stencil ( $s = 3, L = 0, R = M$ ). For even-order schemes, we use four stencils, two of which are central ( $s = 0, L = \lfloor \frac{M}{2} \rfloor + 1, R = \lfloor \frac{M}{2} \rfloor$ ) and ( $s = 1, L = \lfloor \frac{M}{2} \rfloor, R = \lfloor \frac{M}{2} \rfloor + 1$ ), and two fully left- and right-sided as defined before.

To compute the reconstructed polynomial  $\mathbf{w}_h^n(\xi, t^n)$  for element  $T_i$ , we require integral conservation for all elements  $T_j$  within the stencil  $S_i^s$ , that is:

$$\int_{T_j} \mathbf{w}_h^S(\xi, t^n) d\xi = \hat{\mathbf{w}}_i^S(t^n) \int_{T_j} \psi_l(\xi) d\xi = \mathbf{Q}_j^n \quad \forall T_j \in S_i^s. \quad (2.67)$$

The last equivalence leads to a linear system for the unknown coefficients  $\hat{\mathbf{w}}_l^s(t^n)$ . The coefficients  $\hat{\mathbf{w}}_l(t^n)$  are then computed as:

$$\hat{\mathbf{w}}_l(t^n) = \sum_{s=1}^{N_s} \omega_s \hat{\mathbf{w}}_l^s(t^n), \quad (2.68)$$

where  $N_s$  is the number of stencils used. The nonlinear weights  $\omega_s$  are determined by the relations:

$$\omega_s = \frac{\tilde{\omega}_s}{\tilde{\omega}_0 + \tilde{\omega}_{-k} + \tilde{\omega}_k}, \quad \tilde{\omega}_s = \frac{\lambda_s}{(\sigma_s + \epsilon)^r}. \quad (2.69)$$

The oscillation indicators  $\sigma_s$  are computed as:

$$\sigma_s = \sum_{l=1}^M \int_0^1 \left( \frac{\partial^l}{\partial \xi^l} \mathbf{w}_h^s(\xi, t^n) \right)^2 d\xi. \quad (2.70)$$

Parameters  $\epsilon$  and  $r$  are constants, typically  $\epsilon = 10^{-14}$  and  $r = 8$  [13]. For linear weights  $\lambda_s$ , typical values are  $\lambda_0 = 10^5$ ,  $\lambda_{-k} = 1$ , and  $\lambda_k = 1$ . These parameters ensure accurate reconstruction in smooth regions and non-oscillatory reconstruction in regions with sharp gradients due to the nonlinear dependence of the reconstruction operator on the oscillation indicator  $\sigma_s$ . Note that to maintain the well-balanced nature of the numerical scheme, it is essential that the spatial reconstruction preserves this property. Thus, if the reconstruction stencil data corresponds to a stationary solution, the reconstruction polynomial should also correspond to that stationary solution. To achieve this, we perform spatial reconstruction based on deviations from a hypothetical stationary solution. Following what was done in [23], instead of directly reconstructing the cross-sectional area  $A$  of the  $i$ -th computational cell, we compute:

$$\delta A_j^n = A_j^n - A_j^s \left( \tilde{\Gamma}_{1,i}^{LD} \right) \quad \forall T_j \in S_i^s, \quad (2.71)$$

where  $A_j^s \left( \tilde{\Gamma}_{1,i}^{LD} \right)$  is obtained by solving (2.61) with  $\tilde{\Gamma}_{1,i}^{LD}$  for each computational cell. The reconstruction operator is then applied to (2.71), yielding the final polynomial for the area  $A$ :

$$\hat{A}_i(\xi, t^n) = A_i^n + \delta \hat{A}_i^n(\xi), \quad (2.72)$$

where  $\hat{A}_i(\xi, t^n)$  is the first component of  $\mathbf{w}_i^n$ .

### Local Space-Time Predictor: Dumbser-Enaux-Toro Solver

Once the spatial reconstruction is available, we can define a generalized Riemann problem (GRP) at the cell interface  $x = x_{i+\frac{1}{2}}$  (locally at  $x = 0$ ):

$$\begin{cases} \partial_t \mathbf{Q} + \mathbf{A}(\mathbf{Q}) \partial_x \mathbf{Q} = \mathbf{S}(\mathbf{Q}), & x \in \mathcal{R}, \quad t > t^n, \\ \mathbf{Q}(x, 0) = \begin{cases} \mathbf{w}_i(x, t^n) & \text{if } x < 0, \\ \mathbf{w}_{i+1}(x, t^n) & \text{if } x > 0, \end{cases} \end{cases} \quad (2.73)$$

where  $\mathbf{w}_i(x, t^n)$  and  $\mathbf{w}_{i+1}(x, t^n)$  are piecewise polynomials on either side of the cell interface. The GRP solution, which is time-dependent at the interface, will be used to evaluate the integrals in (2.53).

We employ the Dumbser-Enaux-Toro (DET) GRP solver [11] for this purpose. This solver handles local data evolution on both sides of the cell interface to generate space-time predictions

$(\mathbf{w}_h \rightarrow \mathbf{Q}_h^{ST})$  and resolves classical Riemann problems at points along  $x/t = 0$  where the GRP solution is required. Generally, the GRP solution is needed at quadrature points for computations in (2.53). For spatial reconstruction, we use  $\mathbf{Q}_h^{ST}$  to refer to a general space-time prediction rather than a specific space-time polynomial  $\mathbf{Q}_i^{ST,n} = \mathbf{Q}_i^{ST}(x, t)$ , defined in  $V_i^n$ . A notable aspect of the DET solver is the time evolution of initial data on both sides of the interface using a space-time local DG predictor, which provides a local space-time polynomial  $\mathbf{Q}_h^{ST}$  to be used later in (2.53) and (2.52).

We start by transforming system (2.36) to a reference space-time element  $T_E = [0, 1] \times [0, 1]$  with reference coordinates  $\xi$  and  $\tau$ , related to the physical domain by  $x = x_{i-\frac{1}{2}} + \Delta x_i \xi$  and  $t = t^n + \Delta t^n \tau$ . The resulting system is:

$$\partial_\tau \mathbf{Q}_h^{ST} + \mathbf{A}^* \partial_\xi \mathbf{Q}_h^{ST} = \mathbf{S}^*, \quad (2.74)$$

with modified Jacobian and source term vector

$$\mathbf{A}^* = \frac{\Delta t^n}{\Delta x_i} \mathbf{A}(\mathbf{Q}_h^{ST}), \quad \mathbf{S}^* = \Delta t^n \mathbf{S}(\mathbf{Q}_h^{ST}).$$

To simplify the notation, we introduce the following operators:

$$[a, b]^\tau = \int_0^1 a(\xi, \tau) b(\xi, \tau) d\xi, \quad \langle a, b \rangle_{T_E} = \int_0^1 \int_0^1 a(\xi, \tau) b(\xi, \tau) d\xi d\tau. \quad (2.75)$$

Next, we multiply (2.74) by a space-time basis function  $\theta = \theta(\xi, \tau)$  and integrate over the reference element  $T_E$ . Using integration by parts for the time derivative term, we obtain:

$$[\theta, \mathbf{Q}_h^{ST}]^1 - \langle \partial_\tau \theta, \mathbf{Q}_h^{ST} \rangle_{T_E} + \langle \theta, \mathbf{A}^* \partial_\xi \mathbf{Q}_h^{ST} \rangle_{T_E} = [\theta, \mathbf{w}_h]^0 + \langle \theta, \mathbf{S}^* \rangle_{T_E}. \quad (2.76)$$

We use the same space-time basis functions  $\theta$  for  $\mathbf{Q}_h^{ST}$ ,  $\mathbf{A}^* \partial_\xi \mathbf{Q}_h^{ST}$ , and  $\mathbf{S}^*$ , so that:

$$\mathbf{Q}_h^{ST}(\xi, \tau) = \sum_{l=1}^{(M+1)^2} \theta_l \hat{\mathbf{Q}}_l, \quad \mathbf{A}^* \partial_\xi \mathbf{Q}_h^{ST}(\xi, \tau) = \sum_{l=1}^{(M+1)^2} \theta_l \widehat{\mathbf{A}^* \partial_\xi \mathbf{Q}_l}, \quad \mathbf{S}^*(\xi, \tau) = \sum_{l=1}^{(M+1)^2} \theta_l \widehat{\mathbf{S}^*}_l, \quad (2.77)$$

where  $\widehat{\mathbf{S}^*}_l = \Delta t^n \mathbf{S}(\hat{\mathbf{Q}}_l)$ .

The expansion coefficients  $\hat{\mathbf{Q}}_l$ , for  $l = 1, 2, \dots, (M+1)^2$ , are obtained using a fixed-point iteration procedure; see [11] for details. At each iteration step, we solve the system:

$$([\theta_k, \theta_l]^1 - \langle \partial_\tau \theta_k, \theta_l \rangle_{T_E}) \hat{\mathbf{Q}}_l^{m+1} - \langle \theta_k, \theta_l \rangle_{T_E} \widehat{\mathbf{S}^*}_l^{m+1} = [\theta_k, \psi_l]^0 \hat{\mathbf{w}}_l - \langle \theta_k, \theta_l \rangle_{T_E} \widehat{\mathbf{A}^* \partial_\xi \mathbf{Q}_l}^m, \quad (2.78)$$

for  $k = 1, 2, \dots, (M+1)^2$ .

The solution to the GRP at time  $t \in [t^n, t^{n+1}]$  is obtained by solving a classical Riemann problem using the space-time reconstructed states extrapolated to both sides of the cell interface. The space-time average of the source term (2.52) and the non-conservative product space-time average in (2.50) are computed via numerical integration using  $\mathbf{Q}_h^{ST}$  and a quadrature rule of appropriate accuracy. For space polynomials  $\mathbf{w}_h$  and space-time polynomials  $\mathbf{Q}_h^{ST}$ , we use a nodal basis function, with space and space-time nodes given by Gaussian quadrature points and the space and space-time basis functions being the Lagrange interpolation polynomials passing through these points.

### Local Time-Stepping Algorithm

Since we employ a one-step fully explicit numerical scheme, it is crucial to ensure that the Courant-Friedrichs-Lowy (CFL) condition is satisfied within each computational cell. Previous works addressing LTS techniques for numerical schemes of this nature [9] allowed each computational cell to evolve in time based on its local stability criteria, as they considered only a single spatial domain. In contrast, the approach considered in this thesis deals with multiple domains (vessels) sharing boundary nodes (junctions). The computational cost of evaluating (2.53) at junctions is significantly higher than at internal cell interfaces. Hence, we set local time steps to balance the stability limit of the computational scheme and the number of partial time integrals required to compute fluctuations (2.53) along junctions.

Assuming we are working with a network of  $N_v$  vessels, we initialize the local time step for the  $j$ -th vessel as follows:

$$\Delta t_j^0 = \frac{\Delta t_{\max}}{2^{k_j^0}}, \quad (2.79)$$

with

$$k_j^0 = \left\lceil \frac{\log\left(\frac{\Delta t_{\max}}{\widetilde{\Delta t}_j^0}\right)}{\log(2)} \right\rceil, \quad (2.80)$$

where  $\widetilde{\Delta t}_j^0$  is the vessel time step at  $t_j^0$  given by the CFL condition of the scheme for the current state. Generally, the time step  $\widetilde{\Delta t}_j^{n_j}$  is computed as:

$$\widetilde{\Delta t}_j^{n_j} = \frac{\text{CFL} \cdot \tilde{\lambda}_j^{n_j}}{\Delta x_j}, \quad (2.81)$$

with  $n_j$  being the time step iteration of the  $j$ -th vessel and

$$\tilde{\lambda}_j^{n_j} = \max_{i=1,\dots,N_j} (|u_{j,i}^{n_j}| + c_T (A_{j,i}^{n_j}, \theta_{j,i}^{n_j})), \quad (2.82)$$

where  $N_j$  is the number of computational cells in the  $j$ -th vessel. Note that  $\Delta t_{\max}$  can either be user-defined or adaptively determined during the simulation. The current true stability limit of each vessel is calculated using (2.81) and the local time step is updated according to **Algorithm 1**. When the current CFL number exceeds the user-defined value, the local time step is reduced.

Moreover, when the local CFL number is lower than the user-defined value, the local time step might be increased. While the local time step reduction has no implications in the synchronization of the solution at junctions, in the case of time step increase special care is needed. In fact, local time step increase is allowed only if the new time level is a multiple of  $\Delta t_{\max}$ . Otherwise, the new time level will not match the synchronization criteria defined by choosing local time steps using (2.79).

This time step computation approach implies that each vessel  $v_j$ ,  $j = 1, \dots, N_v$ , evolves with its local time step. Practically, for the  $j$ -th vessel to transition from  $t_j^{n_j}$  to  $t_j^{n_j+1}$ , the following update criterion must be satisfied:

$$t_j^{n_j} + \Delta t_j^{n_j} \leq \min_{m=1,\dots,N_{j,\text{neigh}}} (t_m^{n_m} + \Delta t_m^{n_m}), \quad (2.83)$$

where  $N_{j,\text{neigh}}$  denotes the set of vessels sharing a junction with the  $j$ -th vessel. This ensures that the information required to compute (2.53) at the boundaries of the  $j$ -th vessel is available throughout the entire time step.

---

**Algorithm 1** Local time step update algorithm. See [Subsection 4.4](#) for further details.

---

```

1: procedure UPDATE( $\Delta t_j^{n_j}$ )
2:    $CFL_{\text{loc}} = \tilde{\lambda}_j^n \frac{\Delta t_j^{n_j}}{\Delta x_j}$ 
3:    $\Delta t_{\text{loc}} = \Delta t_j^{n_j}$ 
4:    $k_{\text{loc}} = k_j^{n_j}$ 
5:   if  $CFL_{\text{loc}} > CFL$  then
6:     while  $CFL_{\text{loc}} > CFL$  do
7:        $k_{\text{loc}} \leftarrow k_{\text{loc}} + 1$ 
8:        $\Delta t_{\text{loc}} \leftarrow \min \left\{ \Delta t_{\text{max}}, \frac{\Delta t_{\text{max}}}{2^{k_{\text{loc}}}} \right\}$ 
9:        $CFL_{\text{loc}} \leftarrow \tilde{\lambda}_j^{n_j} \frac{\Delta t_{\text{loc}}}{\Delta x_j}$ 
10:      end while
11:       $\Delta t_j^{n_j} \leftarrow \Delta t_{\text{loc}}$ 
12:       $k_j^{n_j} \leftarrow k_{\text{loc}}$ 
13:    else
14:      while  $CFL_{\text{loc}} < CFL$  do
15:         $k_{\text{loc}} \leftarrow k_{\text{loc}} - 1$ 
16:         $\Delta t_{\text{loc}} \leftarrow \min \left\{ \Delta t_{\text{max}}, \frac{\Delta t_{\text{max}}}{2^{k_{\text{loc}}}} \right\}$ 
17:         $CFL_{\text{loc}} \leftarrow \tilde{\lambda}_j^{n_j} \frac{\Delta t_{\text{loc}}}{\Delta x_j}$ 
18:      end while
19:       $k_{\text{loc}} \leftarrow k_{\text{loc}} + 1$ 
20:       $\Delta t_{\text{loc}} \leftarrow \min \left\{ \Delta t_{\text{max}}, \frac{\Delta t_{\text{max}}}{2^{k_{\text{loc}}}} \right\}$ 
21:      if  $\text{mod}(t_j^{n_j} + \Delta t_{\text{loc}}, \Delta t_{\text{max}}) = 0$  then
22:         $\Delta t_j^{n_j} \leftarrow \Delta t_{\text{loc}}$ 
23:         $k_j^{n_j} \leftarrow k_{\text{loc}}$ 
24:      end if
25:    end if
26: end procedure

```

---

To illustrate the time evolution of the numerical solution in a network of vessels, consider [Figure 2.6](#). This example shows a data evolution sequence using (2.79) for time step computation. Initially, all vessels share the same time level, and local time steps remain constant during the interval shown in [Figure 2.6](#). We assume boundaries of vessels not involved in the junction are of a different type and evolve independently of other one-dimensional domains. Boundary conditions may arise from lumped parameter models or inflow boundary conditions. Referring to the LTS evolution example in [Figure 2.6](#), at  $t_j^0$ , each vessel completes its prediction, indicated by dashed lines, enabling vessel 2 to update since all necessary information to compute (2.53) is available for  $[t_2^0, t_2^0 + \Delta t_2^0]$ . Additionally, updating vessel 2 involves storing part of the time integral (2.53) in an auxiliary memory variable for vessels 1 and 3. Once vessel 2 performs its prediction for  $[t_2^1, t_2^1 + \Delta t_2^1]$ , both vessels 1 and 2 can update to their next time level. This procedure continues similarly until vessel 3's solution can be updated.

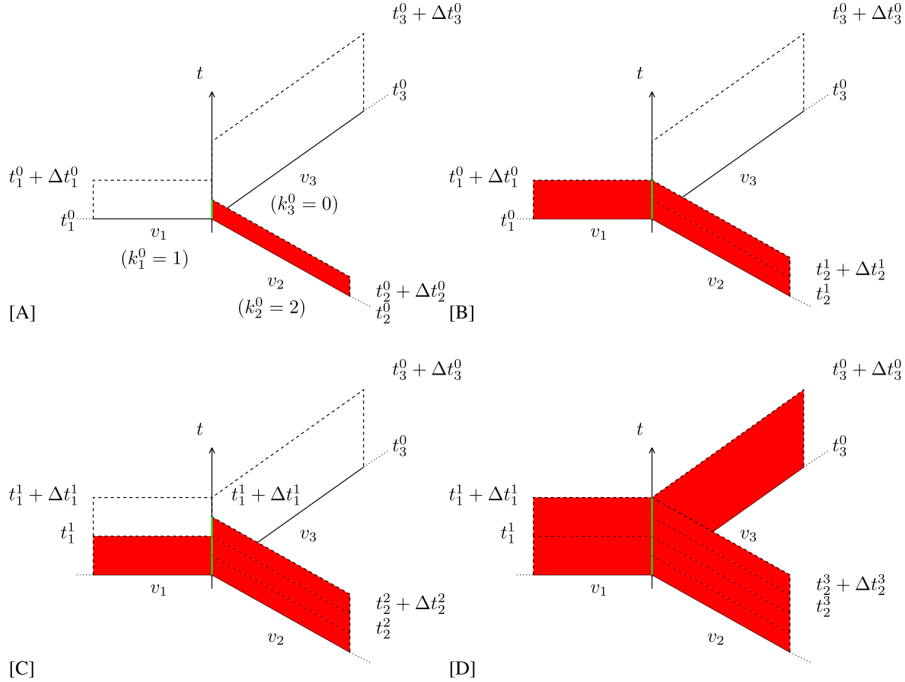


**Figure 2.6:** Schematic representation of the numerical solution at three vessels sharing a node (junction). The space-time prediction is represented by dashed lines, whereas red-filled rectangles indicate a full local timestep update. Moreover, the green lines show the time interval for which fluctuation (2.53), or a part of it, has been computed for all vessels. At  $t_1^0 = t_2^0 = t_3^0$ , available predictions allow for the computation of (2.53) between  $t_2^0$  and  $t_2^1$  (panel A) and the consequent update of vessel  $v_2$ . Next, after a new prediction for vessel  $v_2$  is available, time integral (2.53) between  $t_2^1$  and  $t_2^2$  is computed and therefore both vessels  $v_1$  and  $v_2$  can update their state to the next time level (panel B). Analogous explanations are valid for panels C and D. Image adapted from [20] with permission from the corresponding author.

## 5 Boundary Conditions and Coupling Methods

### 5.1 Computation of Fluctuations Along Junctions

For internal cell interfaces within the one-dimensional domain, classical Riemann problems are solved at appropriate quadrature points for time integration in (2.53). The initial conditions for these Riemann problems are provided by space-time predictions. However, for boundary cell interfaces at junctions, the predicted states are only available on one side of the interface. In such cases, fluctuations are computed as:

$$\mathbf{D}_{j,1-\frac{1}{2}}^+ = \frac{1}{\Delta t_j^{n_j}} \int_{t_j^{n_j}}^{t_j^{n_j+1}} D_{j,1-\frac{1}{2}}^+ \left( \mathbf{Q}_{j,1-\frac{1}{2}}^*(t), \mathbf{Q}_{j,1}^{ST}(0,t), \boldsymbol{\Psi} \right) dt, \quad (2.84)$$

for a cell interface located at  $x_j = 0$ , and as:

$$\mathbf{D}_{j,N_j+\frac{1}{2}}^- = \frac{1}{\Delta t_j^{n_j}} \int_{t_j^{n_j}}^{t_j^{n_j+1}} D_{N_j+\frac{1}{2}}^- \left( \mathbf{Q}_{j,N_j}^{ST}(L_j,t), \mathbf{Q}_{j,N_j+\frac{1}{2}}^*(t), \boldsymbol{\Psi} \right) dt, \quad (2.85)$$

for a cell interface located at  $x_j = L$ .  $\mathbf{Q}_{j,1}^{ST}(0,t)$  and  $\mathbf{Q}_{j,N_j}^{ST}(L_j,t)$  are the predicted space-time polynomials delivered by the DET solver, whereas  $\mathbf{Q}_{j,1-\frac{1}{2}}^*$  and  $\mathbf{Q}_{j,N_j+\frac{1}{2}}^*$  still need to be defined. Using the LTS technique, integrals in (2.84) and (2.85) are computed as the sum of partial time

integrals. Consider the case depicted in **Figure 2.7**, related to the first stage of the update sequence shown in **Figure 2.6**. Here, three vessels share the junction  $P$ . Red dots indicate the quadrature points for the space-time basis, where space-time predictions are readily available for a second-order scheme. Thus, the necessary information for computing the boundary cell fluctuation for vessel 2 is available. By using a Gauss-Lobatto rule, space-time predictions for vessels 1 and 3 are obtained by evaluating the space-time polynomials at the necessary quadrature points (shown as green squares in **Figure 2.7**). As proposed in [19] for elastic

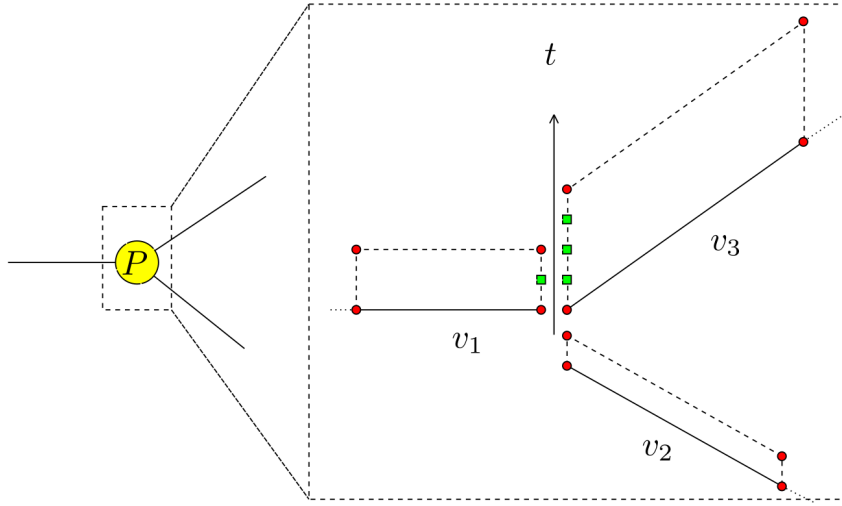


**Figure 2.7:** Schematic representation of the numerical solution at three vessels sharing node  $P$  (junction). The space-time prediction is represented by dashed lines, red nodes indicate the quadrature nodes for the space-time basis in the case of a second order scheme, green squares show locations where the space-time polynomials have to be evaluated to compute the time integration of fluctuations (2.53). Image adapted from [20] with permission from the corresponding author.

vessels and extended in [22] for system (2.36), for each quadrature point at a junction shared by  $N_P$  vessels, a Riemann problem can be defined at time  $t_c$  as follows (no repeated summation implied):

$$\begin{cases} \partial_t \mathbf{Q}_j + \mathbf{A}_j(\mathbf{Q}_j) \partial_x \mathbf{Q}_j = \mathbf{S}_j(\mathbf{Q}_j), & x_j \in \mathcal{R}, t > t_c, \\ \mathbf{Q}_j(t_c) = \mathbf{Q}_{j,\hat{i}}^{ST}(x_j^b, t_c), \end{cases} \quad (2.86)$$

for  $j = 1, \dots, N_P$ . Moreover,  $\hat{i} = 1$  if the shared vertex is located at  $x_j^b = 0$ , whereas  $\hat{i} = N_j$  if  $x_j^b = L_j$ . Assuming sub-critical flow ( $u/c_T < 1$ ), the self-similar solution to (2.86) consists of  $2N_P$  constant states, where  $N_P$  states are the initial condition states provided by the one-dimensional vessels  $\mathbf{Q}_{j,\hat{i}}^{ST}(x_j^b, t_c)$ , with  $j = 1, \dots, N_P$ , while the remaining states  $\mathbf{Q}_{j,\tilde{i}}^*$ , with  $\tilde{i} = 1 - \frac{1}{2}$  if  $x_j^b = 0$  and  $\tilde{i} = N_j + \frac{1}{2}$  if  $x_j^b = L_j$ , are states connected to initial condition states via nonlinear waves (shocks or rarefactions) and among themselves via the linearly degenerate stationary contact discontinuity. Wave relations linking the previously mentioned states in phase space are given by generalized Riemann invariants (2.43), (2.46), (2.47), and (2.48). As proposed in [22], since system (2.36) cannot be recast in conservative form [17], a two-rarefaction Riemann solver is implemented for (2.86). The unknown state vectors  $\mathbf{Q}_{j,i}^*$ ,  $j = 1, \dots, N_P$ , are

computed by solving the following system of  $3N_P$  nonlinear equations:

$$\begin{cases} \sum_{j=1}^{N_P} g_{P,j} A_{j,\tilde{i}}^* u_{j,\tilde{i}}^* = 0, \\ p(A_{1,\tilde{i}}^*, \theta_{1,\tilde{i}}^*) + \frac{1}{2}\rho(u_{1,\tilde{i}}^*)^2 - p(A_{j,\tilde{i}}^{ST}, \theta_{j,\tilde{i}}^{ST}) - \frac{1}{2}\rho(u_{j,\tilde{i}}^{ST})^2 = 0, \quad j = 2, \dots, N_P, \\ u_{j,\tilde{i}}^* - u_{j,\tilde{i}}^{ST}(x_j^b, t_c) + g_{P,j} \beta_j = 0, \quad j = 1, \dots, N_P, \\ \theta_{j,\tilde{i}}^* + \frac{A_{j,\tilde{i}}^*}{T_j} - \theta_{j,\tilde{i}}^{ST}(x_j^b, t_c) - \frac{A_{j,\tilde{i}}^{ST}(x_j^b, t_c)}{T_j} = 0, \quad j = 1, \dots, N_P. \end{cases} \quad (2.87)$$

Here,  $\beta_j$  is defined as:

$$\beta_j = \int_{A_{j,\tilde{i}}^{ST}(x_j^b, t_c)}^{A_{j,\tilde{i}}^*} \frac{\tilde{c}_T(\xi)}{\xi} d\xi, \quad (2.88)$$

and  $g_{P,j}$  is the auxiliary function:

$$g_{P,j} = \begin{cases} 1, & \text{if } x_{P,j} = L_j, \\ -1, & \text{if } x_{P,j} = 0, \end{cases} \quad (2.89)$$

where  $x_{P,j}$  is the local coordinate of the  $j$ -th vessel, evaluated at vertex P and  $L_j$  is the vessel length. Note that  $T$ , the relaxation time, can be different in each vessel. Summarizing, if space-time predictions for all  $N_P$  vessels sharing a node are available at time  $t_c$ , then a Riemann problem at a junction can be defined and solved, yielding states  $\mathbf{Q}_{j,\tilde{i}}^*(t_c)$ , needed for the computation of first order fluctuations at specified quadrature points in (2.84) and (2.85). The particular form of fluctuations (2.84) and (2.85) derive from considerations found in [26]. In practice, when the Godunov states of a Riemann problem are available for the computation of a fluctuation, only the Godunov state and the initial condition to the right of the initial discontinuity are needed to compute the positive fluctuation, whereas for the negative fluctuation the corresponding Godunov state and the initial data to the left of the discontinuity are needed.

## 5.2 Ghost Cell Filling for Spatial Reconstruction

At time  $t_j^n$ , the weighted essentially non-oscillatory reconstruction procedure requires the state variable values at  $M$  ghost cells on each side of the one-dimensional domain. We employ the methodology introduced in [22]. To accurately approximate the solution outside the one-dimensional domain, which is necessary for computing cell averages at ghost cells, a Taylor series expansion around the internal vertex  $P$ , shared by the  $j$ -th vessel, is used. For a local spatial coordinate  $\epsilon$  with its origin at the internal vertex  $P$ , the extrapolated state vector is:

$$\mathbf{Q}_j^g(\epsilon, t_j^{n_j}) = \mathbf{Q}_{j,\tilde{i}}^*(t_j^{n_j-1} + \Delta t_j^{n_j-1}) + \sum_{r=1}^M \frac{1}{r!} \partial_x^{(r)} \mathbf{Q}_{j,\tilde{i}}^*(t_j^{n_j-1} + \Delta t_j^{n_j-1}) \epsilon^r, \quad (2.90)$$

where  $\mathbf{Q}_{j,\tilde{i}}^*(t_j^{n_j-1} + \Delta t_j^{n_j-1})$  is the solution of the Riemann problem at a junction (2.86) for initial conditions provided by the DET solver prediction from the previous time step. For  $n_j = 0$ , the initial condition is used to assign  $\mathbf{Q}_{j,\tilde{i}}^*(t_j^{n_j-1} + \Delta t_j^{n_j-1})$  and its spatial derivatives. The spatial derivatives required in (2.90) are computed using a procedure inspired by the Tiratev-Toro generalized Riemann problem solver [27], where spatial derivatives are derived from a linearized version of the original PDE system. Therefore,  $\partial_x \mathbf{Q}_{j,\tilde{i}}^*(t_j^{n_j-1} + \Delta t_j^{n_j-1})$  are

computed by solving the following Riemann problem:

$$\begin{cases} \partial_t \left( \partial_x^{(r)} \mathbf{Q}_k \left( t_j^{n_j-1} + \Delta t_j^{n_j-1} \right) \right) + \bar{\mathbf{A}}_p \partial_x \left( \partial_x^{(r)} \mathbf{Q}_k \left( t_j^{n_j-1} + \Delta t_j^{n_j-1} \right) \right) + \Delta t_j^{n_j-1} = 0, & x \in \mathcal{R}, t > t_j^{n_j-1}, \\ \partial_x^{(r)} \mathbf{Q}_k \left( t_j^{n_j-1} + \Delta t_j^{n_j-1} \right) = \partial_x^{(r)} \mathbf{Q}_{k,\hat{i}}^{ST} \left( x_j^b, t_j^{n_j-1} + \Delta t_j^{n_j-1} \right), \end{cases} \quad (2.91)$$

for  $k = 1, \dots, N_P$ , with  $\bar{\mathbf{A}}_k$  as the linearized Jacobian:

$$\bar{\mathbf{A}}_k = \mathbf{A} \left( \mathbf{Q}_{k,\hat{i}}^* \left( t_j^{n_j-1} + \Delta t_j^{n_j-1} \right) \right). \quad (2.92)$$

Note that we use index  $k$  instead of  $j$  to highlight that, to compute spatial gradients for the  $j$ -th vessel, we solve a linear Riemann problem involving the spatial gradients of the predicted space-time polynomials of all vessels shared by junction  $P$ , evaluated at time  $t_j^{n_j-1} + \Delta t_j^{n_j-1}$ . Initial conditions for (2.91) are directly taken from the implicit DG prediction of the previous time step by recursively making the following *ansatz*:

$$\widehat{\langle \theta_k, \theta_l \rangle \partial_\xi^{(r)} \mathbf{Q}_l} = \langle \theta_k, \partial_\xi \theta_l \rangle \widehat{\partial_\xi^{(r-1)} \mathbf{Q}_l} \quad k = 1, \dots, (M+1)^2, \quad (2.93)$$

with  $r = 1, \dots, M$  and  $l = 1, 2, \dots, (M+1)^2$ . Note that the matrix  $\langle \theta_k, \theta_l \rangle^{-1} \langle \theta_k, \partial_\xi \theta_l \rangle$  is computed only once, so that the spatial derivatives are obtained via a simple matrix-vector product. Note that the computational cost of solving the Riemann problem for the linearized system is relatively modest, requiring the solution of  $M$  linear systems of  $3N_P$  unknowns.

### 5.3 Prescribing Pressure or Flow and Coupling to Lumped Models

Additional boundary conditions must be assigned to a network of one-dimensional vessels. Specifically, one may need to prescribe pressure or flow rate at a specific location (e.g., inflow at the root of the aorta) or couple terminal vessels to lumped parameter models. Typically, the prescribed quantity concerns only one component of the state vector (2.37). In all scenarios, the constancy of Riemann invariants across rarefaction waves is used to determine the missing state variables' values. For example, consider the  $j$ -th vessel connected to an RCR lumped parameter model, shown in [Figure 2.8](#), at  $x_j = L_j$ . The governing equation of the lumped parameter model is:

$$\frac{dP_{\text{lumped}}}{dt} = \frac{1}{C} (Q_{\text{in}} - Q_{\text{out}}), \quad (2.94)$$

where  $P_{\text{lumped}}$  is the compartment pressure and  $C$  is the compliance. Equation (2.94) is discretized as:

$$P_{\text{lumped}}^{n+1} = P_{\text{lumped}}^n + \frac{\Delta t_j^{n_j}}{C} \left( Q_{\text{in}}^n - \frac{P_{\text{lumped}}^n - P_{\text{out}}}{R_d} \right), \quad (2.95)$$

with  $R_d$  being the distal resistance and  $P_{\text{out}}$  the outflow pressure, given. Flow  $Q_{\text{in}}$  is computed as follows. First, note that in order to compute (2.85), states  $\mathbf{Q}_{j,N_j+\frac{1}{2}}^*(t)$  must be available at each quadrature point for time integrals, while states  $\mathbf{Q}_{j,N_j}^{ST}(L_j, t)$  are delivered by the space-time prediction illustrated in [Subsection 4.4](#). In order to compute  $\mathbf{Q}_{j,N_j+\frac{1}{2}}^*(t_c)$ , at each quadrature point with corresponding time  $t_c$ , we solve the following system of non-linear equations:

$$\begin{cases} A_{j,N_j+\frac{1}{2}}^* u_{N_j+\frac{1}{2},j}^* - \frac{p(A_{j,N_j+\frac{1}{2}}^*) - P_{\text{lumped}}^n}{R_p} = 0, \\ u_{j,N_j+\frac{1}{2}}^* - u_{j,N_j}^{ST}(L_j, t_c) + \beta_j = 0, \\ \theta_{j,N_j+\frac{1}{2}}^* + \frac{A_{j,N_j+\frac{1}{2}}^*}{T_j} - \theta_{j,N_j}^{ST}(L_j, t_c) - \frac{A_{j,N_j}^{ST}(L_j, t_c)}{T_j} = 0, \end{cases} \quad (2.96)$$

where  $R_p$  is the proximal resistance. Finally,  $Q_{in}^n$  is computed as the time integral of  $\mathbf{Q}_{j,N_j+\frac{1}{2}}^*(t)$  in the interval  $[t_j^n, t_j^{n_j} + \Delta t_j^{n_j}]$ .

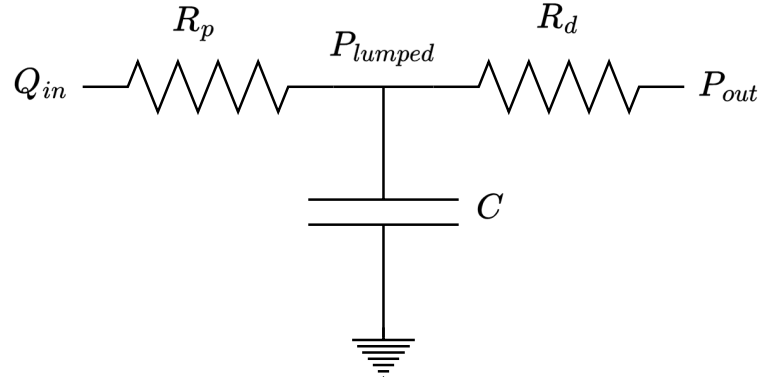


**Figure 2.8:** RCR lumped parameter model.  $P_{lumped}$  is the compartment pressure,  $C$  is the compliance,  $R_p$  and  $R_d$  are the proximal and distal resistances,  $P_{out}$  is the outflow pressure and  $Q_{in}$  is the blood inflow. Image adapted from [20] with permission from the corresponding author.

### Local Time-Stepping Solver Algorithm

In [Algorithm 2](#) we report a description of the LTS solver proposed.

---

#### Algorithm 2 LTS solver algorithm

---

```

1: procedure SOLVE_NETWORK
2:   Input:  $N_v$  vessels with  $N_j$  junctions,  $t_{\text{ini}}$  to  $t_{\text{end}}$ 
3:   for  $j = 1$  to  $N_v$  do
4:     Set initial condition
5:     Set initial time  $t_j^0 = t_{\text{ini}}$ 
6:     Set initial local time steps  $\Delta t_j^{n_j}$  using (2.79)
7:     Set  $\text{UPD}_j = 1$ 
8:   end for
9:   Set  $\text{FINISH} = 0$ 
10:  while  $\text{FINISH} \neq 1$  do
11:    for  $j = 1$  to  $N_v$  do
12:      if  $\text{UPD}_j = 1$  then
13:        Perform spatial reconstruction
14:        Update  $\Delta t_j^{n_j}$  (Algorithm 1)
15:        Perform space-time prediction
16:         $\text{UPD}_j \leftarrow 0$ 
17:      end if
18:    end for
19:    for  $j = 1$  to  $N_j$  do
20:      Compute partial integral of (2.53) for time intervals where information is avail-
         able
21:    end for
22:    for  $j = 1$  to  $N_v$  do
23:      if boundary fluctuation integrals have been computed up to  $t_j^n + \Delta t_j^n$  then
24:        Assign other boundary conditions
25:        Update solution for the  $j$ -th vessel
26:        Update local iteration:  $n_j \leftarrow n_j + 1$ 
27:        Update local time:  $t^{n_j} \leftarrow t^{n_j-1} + \Delta t_j^{n_j-1}$ 
28:         $\text{UPD}_j \leftarrow 1$ 
29:      end if
30:    end for
31:    if  $t_j^{n_j} = t_{\text{end}} \quad \forall j \in N_v$  then
32:       $\text{FINISH} \leftarrow 1$ 
33:    end if
34:  end while
35: end procedure

```

---



---

# Bibliography

---

- [1] Jordi Alastruey et al. “**Pulse wave propagation in a model human arterial network: Assessment of 1-D visco-elastic simulations against in vitro measurements**”. In: *Journal of Biomechanics* 44.12 (Aug. 2011), pp. 2250–2258. DOI: [10.1016/j.jbiomech.2011.05.041](https://doi.org/10.1016/j.jbiomech.2011.05.041).
- [2] Pablo J. Blanco et al. “**An Anatomically Detailed Arterial Network Model for One-Dimensional Computational Hemodynamics**”. In: *IEEE Transactions on Biomedical Engineering* 62.2 (Feb. 2015), pp. 736–753. DOI: [10.1109/tbme.2014.2364522](https://doi.org/10.1109/tbme.2014.2364522).
- [3] Pablo J. Blanco et al. “**On the anatomical definition of arterial networks in blood flow simulations: comparison of detailed and simplified models**”. In: *Biomechanics and Modeling in Mechanobiology* 19.5 (Feb. 2020), pp. 1663–1678. DOI: [10.1007/s10237-020-01298-4](https://doi.org/10.1007/s10237-020-01298-4).
- [4] Caterina Dalmaso. *Preliminary Documentation for ADAVN86*. Tech. rep. Trento (TN): Università degli Studi di Trento, 2024.
- [5] Wolfgang Dauber. “**Pocket Atlas of Human Anatomy by Feneis**”. 5th. New York, United States: Thieme Medical Publishers, 2007.
- [6] Michael Dumbser et al. “**A Simple Extension of the Osher Riemann Solver to Non-conservative Hyperbolic Systems**”. In: *Journal of Scientific Computing* 48.1–3 (July 2010), pp. 70–88. DOI: [10.1007/s10915-010-9400-3](https://doi.org/10.1007/s10915-010-9400-3).
- [7] Michael Dumbser et al. “**ADER schemes on unstructured meshes for nonconservative hyperbolic systems: Applications to geophysical flows**”. In: *Computers & Fluids* 38.9 (Oct. 2009), pp. 1731–1748. DOI: [10.1016/j.compfluid.2009.03.008](https://doi.org/10.1016/j.compfluid.2009.03.008).
- [8] Michael Dumbser et al. “**ADER-WENO finite volume schemes with space–time adaptive mesh refinement**”. In: *Journal of Computational Physics* 248 (Sept. 2013), pp. 257–286. DOI: [10.1016/j.jcp.2013.04.017](https://doi.org/10.1016/j.jcp.2013.04.017).
- [9] Michael Dumbser et al. “**An arbitrary high-order Discontinuous Galerkin method for elastic waves on unstructured meshes - V. Local time stepping and p-adaptivity**”. In: *Geophysical Journal International* 171.2 (Nov. 2007), pp. 695–717. DOI: [10.1111/j.1365-246X.2007.03427.x](https://doi.org/10.1111/j.1365-246X.2007.03427.x).
- [10] Michael Dumbser et al. “**Arbitrary high order non-oscillatory finite volume schemes on unstructured meshes for linear hyperbolic systems**”. In: *Journal of Computational Physics* 221.2 (Feb. 2007), pp. 693–723. DOI: [10.1016/j.jcp.2006.06.043](https://doi.org/10.1016/j.jcp.2006.06.043).
- [11] Michael Dumbser et al. “**Finite volume schemes of very high order of accuracy for stiff hyperbolic balance laws**”. In: *Journal of Computational Physics* 227.8 (Apr. 2008), pp. 3971–4001. DOI: [10.1016/j.jcp.2007.12.005](https://doi.org/10.1016/j.jcp.2007.12.005).
- [12] Michael Dumbser et al. “**FORCE schemes on unstructured meshes II: Non-conservative hyperbolic systems**”. In: *Computer Methods in Applied Mechanics and Engineering* 199.9–12 (Jan. 2010), pp. 625–647. DOI: [10.1016/j.cma.2009.10.016](https://doi.org/10.1016/j.cma.2009.10.016).
- [13] Michael Dumbser et al. “**High order space–time adaptive ADER-WENO finite volume schemes for non-conservative hyperbolic systems**”. In: *Computer Methods in Applied Mechanics and Engineering* 268 (Jan. 2014), pp. 359–387. DOI: [10.1016/j.cma.2013.09.022](https://doi.org/10.1016/j.cma.2013.09.022).
- [14] Luca Formaggia et al. “**One-dimensional models for blood flow in arteries**”. In: *Journal of Engineering Mathematics* 47.3/4 (Dec. 2003), pp. 251–276. DOI: [10.1023/B:ENGI.0000007980.01347.29](https://doi.org/10.1023/B:ENGI.0000007980.01347.29).
- [15] William Jr Hood. “**Regional venous drainage of the human heart**”. In: *Br. Heart J.* 30 (1968), pp. 105–109. DOI: [10.1136/hrt.30.1.105](https://doi.org/10.1136/hrt.30.1.105).
- [16] Eleuterio Toro Lucas Omar Müller. Manuscript in preparation, consulted in unpublished version from 2024.
- [17] Gino I. Montecinos et al. “**Hyperbolic reformulation of a 1D viscoelastic blood flow model and ADER finite volume schemes**”. In: *Journal of Computational Physics* 266 (June 2014), pp. 101–123. DOI: [10.1016/j.jcp.2014.02.013](https://doi.org/10.1016/j.jcp.2014.02.013).
- [18] Lucas Mueller et al. “**Consistent treatment of viscoelastic effects at junctions in one-dimensional blood flow models**”. In: *Jour-*

- nal of Computational Physics* 314 (Mar. 2016). DOI: [10.1016/j.jcp.2016.03.012](https://doi.org/10.1016/j.jcp.2016.03.012).
- [19] Lucas O. Müller et al. “**A high order approximation of hyperbolic conservation laws in networks: Application to one-dimensional blood flow**”. In: *Journal of Computational Physics* 300 (2015), pp. 423–437. DOI: <https://doi.org/10.1016/j.jcp.2015.07.056>.
- [20] Lucas O. Müller et al. “**A high-order local time stepping finite volume solver for one-dimensional blood flow simulations: application to the ADAN model**”. In: *International Journal for Numerical Methods in Biomedical Engineering* 32.10 (Jan. 2016), pp. 1538–1555. DOI: [10.1002/cnm.2761](https://doi.org/10.1002/cnm.2761).
- [21] Lucas O. Müller et al. “**An anatomically detailed arterial-venous network model. Cerebral and coronary circulation**”. In: *Frontiers in Physiology* 14 (June 2023). DOI: [10.3389/fphys.2023.1162391](https://doi.org/10.3389/fphys.2023.1162391).
- [22] Lucas O. Müller et al. “**Consistent treatment of viscoelastic effects at junctions in one-dimensional blood flow models**”. In: *Journal of Computational Physics* 314 (June 2016), pp. 167–193. DOI: [10.1016/j.jcp.2016.03.012](https://doi.org/10.1016/j.jcp.2016.03.012).
- [23] Lucas O. Müller et al. “**Well-balanced high-order solver for blood flow in networks of vessels with variable properties**”. In: *International Journal for Numerical Methods in Biomedical Engineering* 29.12 (July 2013), pp. 1388–1411. DOI: [10.1002/cnm.2580](https://doi.org/10.1002/cnm.2580).
- [24] Jonathan P. Mynard et al. “**One-dimensional haemodynamic modeling and wave dynamics in the entire adult circulation**”. In: *Annals of Biomedical Engineering* 43.6 (June 2015). Erratum in: *Ann Biomed Eng.* 2016 Apr;44(4):1324. doi: 10.1007/s10439-016-1564-z., pp. 1443–1460. DOI: [10.1007/s10439-015-1313-8](https://doi.org/10.1007/s10439-015-1313-8).
- [25] Jonathan P. Mynard et al. “**Scalability and in vivo validation of a multiscale numerical model of the left coronary circulation**”. In: *American Journal of Physiology-Heart and Circulatory Physiology* 306.4 (Feb. 2014), H517–H528. DOI: [10.1152/ajpheart.00603.2013](https://doi.org/10.1152/ajpheart.00603.2013).
- [26] Carlos Parés. “**Numerical methods for non-conservative hyperbolic systems: a theoretical framework**”. In: *SIAM Journal on Numerical Analysis* 44.1 (Jan. 2006), pp. 300–321. DOI: [10.1137/050628052](https://doi.org/10.1137/050628052).
- [27] E. F. Toro et al. “**Solution of the Generalized Riemann Problem for Advection-Reaction Equations**”. In: *Proceedings: Mathematical, Physical and Engineering Sciences* 458.2018 (2002), pp. 271–281.
- [28] Eleuterio F. Toro et al. “**Flow in Collapsible Tubes with Discontinuous Mechanical Properties: Mathematical Model and Exact Solutions**”. In: *Communications in Computational Physics* 13.2 (2013), pp. 361–385. DOI: [10.4208/cicp.210611.240212a](https://doi.org/10.4208/cicp.210611.240212a).
- [29] Mauro Ursino. “**A mathematical study of human intracranial hydrodynamics part 1—The cerebrospinal fluid pulse pressure**”. In: *Annals of Biomedical Engineering* 16.4 (July 1988), pp. 379–401. DOI: [10.1007/bf02364625](https://doi.org/10.1007/bf02364625).

---

## The CircAdapt model

---

## Contents of the chapter

---

1	Introduction to the Model . . . . .	65
2	Tube Module . . . . .	66
	2.1    The CircAdapt Formulation . . . . .	66
3	Sarcomere Module . . . . .	68
	3.1    The CircAdapt Formulation . . . . .	68
4	Chamber Module . . . . .	70
	4.1    The CircAdapt Formulation . . . . .	70
5	TriSeg Model of Ventricular Interaction . . . . .	72
	5.1    The CircAdapt Formulation . . . . .	72
6	Pericardial Mechanics . . . . .	74
	6.1    The CircAdapt Formulation . . . . .	74
7	Periphery . . . . .	74
	7.1    The CircAdapt Formulation . . . . .	74
8	Connecting the Modules . . . . .	75
	8.1    Volume Change of Inflow Arteries and Outflow Veins . . . . .	75
9	Valve Dynamics . . . . .	75
	9.1    The CircAdapt Formulation . . . . .	75
10	Solving the ODE System . . . . .	77
	10.1   Introduction to the Numerical Analysis . . . . .	77
	10.2   Analysis of One-step Methods . . . . .	78
	10.3   The Zero-Stability . . . . .	79
	10.4   Convergence Analysis for the Forward Euler Method . . . . .	80
	10.5   The Absolute Stability of the Forward Euler Method . . . . .	81
	10.6   Example of Instability for the Forward Euler Method . . . . .	82
	10.7   Systems of ODEs . . . . .	82
11	Limitations of the CircAdapt Model . . . . .	84
	11.1   Educational Origins and Purpose . . . . .	84
	11.2   Mass Conservation . . . . .	84
	11.3   Negative Pressures . . . . .	84
	11.4   Defects Activation . . . . .	84

---

## 1 Introduction to the Model

CircAdapt [2] is a lumped 0D model representing the heart and the vascular system. A distinctive feature is its ability to support real-time simulation of cardiovascular dynamics across a wide range of physiological and pathological scenarios.

As depicted in [Figure 3.1](#), the cardiovascular system is modeled as a series of interconnected modules: a tube module for the systemic and pulmonary arteries and veins ([Section 2](#)); a chamber module for the actively contracting left and right atria and ventricles ([Section 4](#)), with myofiber mechanics and contraction detailed in a sarcomere module ([Section 3](#)); it also includes mechanical interaction between ventricles through the inter-ventricular septum [7]; a valve module representing the aortic, mitral, pulmonary, and tricuspid valves ([Section 9](#)); a module for systemic and pulmonary peripheral microvasculatures ([Section 7](#)); and a module accounting for pericardial effects ([Section 6](#)). These modules are connected through flows over valves and venous-atrial inlets [3].

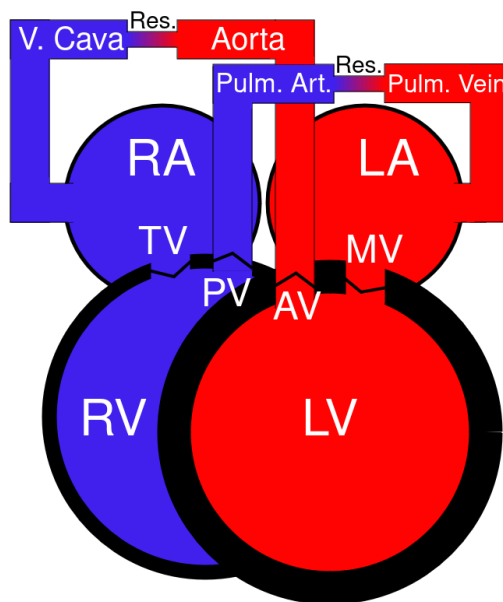


**Figure 3.1:** Schematic representation of the cardiovascular system in the CircAdapt model.

The entire model consists of a system of ordinary differential equations (ODEs) in state variables with respect to time, forming a system similar to earlier models of the whole circulation [8, 9, 10, 12, 13]. In summary, cavity pressures and volumes are interconnected in the following way: volumes affect cavity wall areas, which then determine the strain of the myofibers in the wall. This strain is used to calculate myofiber stress, which generates wall tension in each cardiac wall. Using Laplace's law, transmural pressure is calculated from wall tension and curvature for each wall. Cavity pressures are obtained by adding transmural pressures to the intra-pericardial pressure around the myocardial walls. These cavity pressures are then used to update flow over valves and intra-cavitory volumes.

A significant advantage of this modular design is that each simple 0D module can be easily swapped with a more complex model. To understand the modularity of the model, see [Figure 3.2](#). For a circuit representation of the model, see [Figure 3.3](#).

In what follows, we will use the formulation proposed in [3].

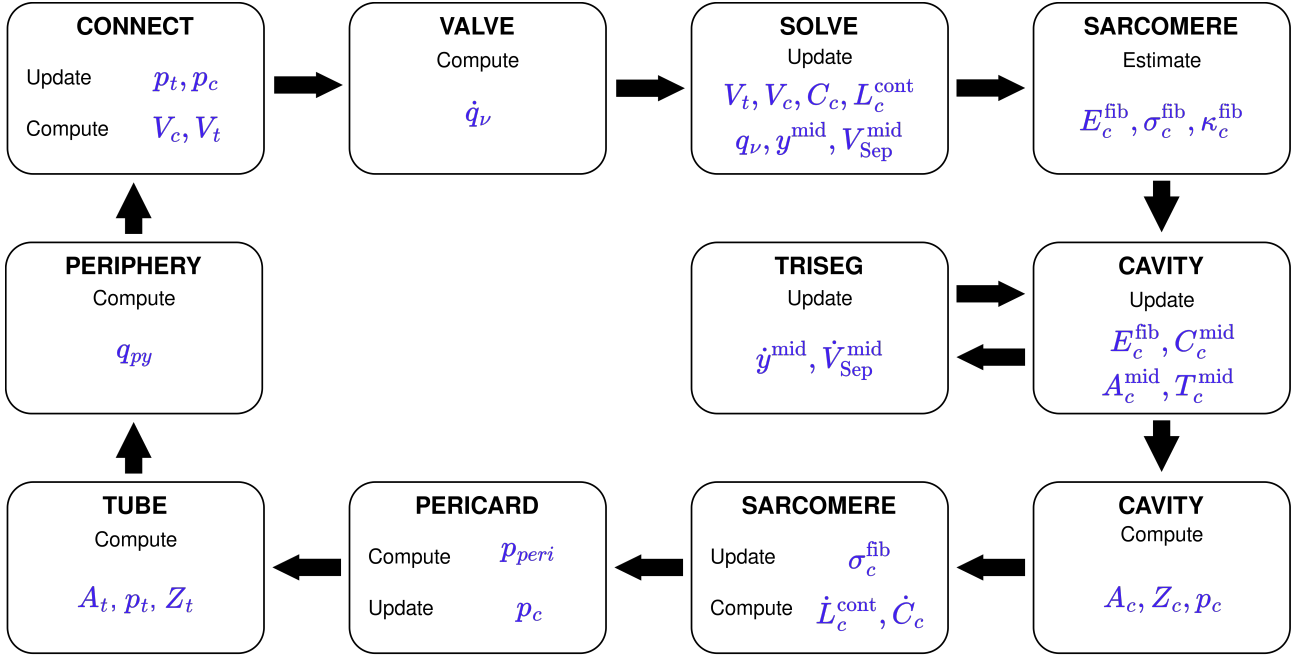


**Figure 3.2:** The CircAdapt model connects tubes ( $t$ ), cavities ( $c$ ), valves ( $v$ ), and pulmonary and systemic periphery ( $py$ ). In each timestep the ODE system is solved to update the ODE variables, i.e., volumes of tubes ( $V_t$ ) and cavities ( $V_c$ ); sarcomere contractility ( $C_c$ ) and sarcomere length ( $L_c^{cont}$ ) for each of the cavities and the septum; flow over valves ( $q_v$ ); and septal midwall volume ( $V_{Sep}^{mid}$ ) and radius ( $y_{mid}$ ). In the following steps the updated variables are used to compute current pressures ( $p_c$ ,  $p_t$ ), cross sectional areas ( $A_c$ ,  $A_t$ ), and impedances ( $Z_c$ ,  $Z_t$ ) for tubes and cavities; fiber strain ( $E_c^{fib}$ ), fiber stiffness ( $\kappa_c^{fib}$ ), and fiber stress ( $\sigma_c^{fib}$ ) for the sarcomeres of each cavity and the septum; midwall curvature ( $C_c^{mid}$ ), midwall area ( $A_c^{mid}$ ), and midwall tension ( $T_c^{mid}$ ) for each cavity and the septum; pericardial pressure  $p_{peri}$ ; and flow over the systemic and pulmonary periphery  $q_{py}$ . Image based on [3].

## 2 Tube Module

### 2.1 The CircAdapt Formulation

The tube module represents the entrance of a flexible blood vessel, which propagates a pressure-flow wave component added to a constant flow [2]. This module is used to simulate the most important blood vessels: aorta (AO), arteria pulmonalis (AP), venae cavae (VC), and venae pulmonales (VP). For the entire section we will consider  $t \in \{\text{AO}, \text{AP}, \text{VC}, \text{VP}\}$ .

The lumen cross-sectional area is computed as

$$A_t = \frac{V_t}{l_t}, \quad (3.1)$$

where  $V_t$  is the cavity volume and  $l_t$  is the length of the vessel segment.

The average extension of the fibers in the wall  $\lambda_t$  is computed using a model of a tube with a fibrous wall as in [1], and it is given by

$$\lambda_t = \left(1 + 2\frac{V_t}{V_t^{\text{wall}}}\right)^{1/3} = \left(1 + 2\frac{A_t}{A_t^{\text{wall}}}\right)^{1/3}, \quad (3.2)$$

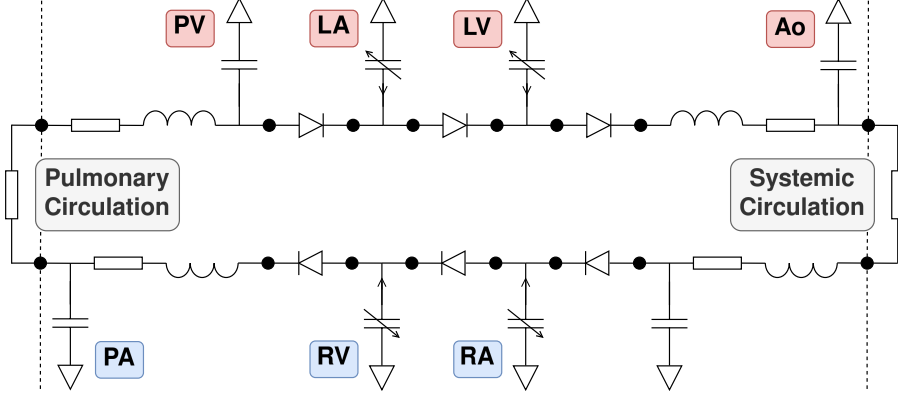


**Figure 3.3:** Schematic diagram of the CircAdapt model in circuit form. Image based on [3].

where  $A_t^{\text{wall}}$  is the wall cross-sectional area and  $V_t^{\text{wall}} = A_t^{\text{wall}}l_t$  is the wall volume. Cavity pressure depends on  $\lambda_t$  with the relation:

$$p_t = \frac{\sigma_t(\lambda_t)}{\lambda_t^3}, \quad (3.3)$$

where  $\sigma_t$  is the mean Cauchy fiber stress, which is modeled, as seen in [1], by the constitutive equation

$$\sigma_t(\lambda_t) = \sigma_t^{\text{ref}} \cdot \left( \frac{\lambda_t}{\lambda_t^{\text{ref}}} \right)^{k_t}, \quad (3.4)$$

where  $k_t$  is a stiffness parameter,  $\lambda_t^{\text{ref}} = \left(1 + 2\frac{V_t^{\text{ref}}}{V_t^{\text{wall}}}\right)^{1/3}$  and  $\sigma_t^{\text{ref}} = p_t^{\text{ref}}(\lambda_t^{\text{ref}})^3$  are the fiber extension and fiber state at normal physiological reference state, respectively; and  $p_t^{\text{ref}}$  is the reference tube pressure.

By combining what has been obtained above, the current tube pressure is computed as

$$p_t = p_t^{\text{ref}} \left( \frac{\lambda_t}{\lambda_t^{\text{ref}}} \right)^{k-3} = p_t^{\text{ref}} \left( \frac{V_t^{\text{wall}} + 2V_t}{V_t^{\text{wall}} + 2V_t^{\text{ref}}} \right)^{\frac{k-3}{3}} = p_t^{\text{ref}} \left( \frac{A_t^{\text{wall}} + 2A_t}{A_t^{\text{wall}} + 2A_t^{\text{ref}}} \right)^{\frac{k-3}{3}}, \quad (3.5)$$

where  $A_t^{\text{ref}}$  is the initial cross sectional area and  $V_t^{\text{ref}} = A_t^{\text{ref}}l_t$  is the initial vessel volume. Finally, the compliance is computed as:

$$\begin{aligned} \frac{1}{C_t} &= \frac{dp_t}{dV_t} \\ &= \frac{d}{dV_t} \left[ p_t^{\text{ref}} \left( \frac{V_t^{\text{wall}} + 2V_t}{V_t^{\text{wall}} + 2V_t^{\text{ref}}} \right)^{\frac{k-3}{3}} \right] \\ &= p_t^{\text{ref}} \frac{k-3}{3} \left( \frac{V_t^{\text{wall}} + 2V_t}{V_t^{\text{wall}} + 2V_t^{\text{ref}}} \right)^{\frac{k-3}{3}-1} \frac{2}{V_t^{\text{wall}} + 2V_t^{\text{ref}}} \\ &= \frac{2p_t(k-3)}{3(V_t^{\text{wall}} + 2V_t)} \\ &= \frac{2p_t(k-3)}{3l_t(A_t^{\text{wall}} + 2A_t)} \end{aligned} \quad (3.6)$$

The basic relation between characteristic wave impedance  $Z_t$ , compliance  $C_t$ , and inertance  $I_t$

$$Z_t^2 = \frac{I_t}{C_t} = \frac{\rho_b I_t}{A_t C_t} \quad (3.7)$$

yields

$$Z_t = \sqrt{\frac{2 \rho_b p_t l_t^2 (k - 3)}{3 V_t (V_t^{\text{wall}} + 2 V_t)}} = \sqrt{\frac{2 \rho_b p_t (k - 3)}{3 A_t (A_t^{\text{wall}} + 2 A_t)}} \quad (3.8)$$

where  $\rho_b$  is the blood density.

## 3 Sarcomere Module

### 3.1 The CircAdapt Formulation

The sarcomere contraction model is based on a modified Hill model [7, 14]. For the rest of this section we consider  $c \in \{\text{LV}, \text{RV}, \text{Sep}, \text{LA}, \text{RA}\}$ , with the left (LV) and right (RV) ventricle, the septum (Sep), and the left (LA) and right (RA) atrium [3].

#### Strain and Length

In CircAdapt, natural strain  $E_c^{\text{fib}}$  of the myofiber is estimated as

$$E_c^{\text{fib}} = \ln \left( \frac{L_c^s}{L_c^{\text{s,ref}}} \right), \quad (3.9)$$

from which the total sarcomere length  $L_c^s$  is computed as

$$L_c^s = L_c^{\text{s,ref}} \exp(E_c^{\text{fib}}), \quad (3.10)$$

where  $L_c^{\text{s,ref}}$  is a constant describing the reference sarcomere length. The sarcomere is supposed to be composed of a contractile element of length  $L_c^{\text{cont}}$  in series with an elastic element of length  $L_c^{\text{elast}} = L_c^s - L_c^{\text{cont}}$ .

#### Sarcomere Active Stress

Sarcomere contracting length  $L_c^{\text{cont}}$  varies over time according to the law:

$$\begin{aligned} \dot{L}_c^{\text{cont}} &= \frac{dL_c^{\text{cont}}}{dt} \\ &= v^{\max} \left[ \frac{L_c^s - L_c^{\text{cont}}}{L_c^{\text{elast,iso}}} - 1 \right], \end{aligned} \quad (3.11)$$

where  $L_c^{\text{elast,iso}}$ , a constant, is the length of the series elastic element during isovolumetric contraction and  $v^{\max}$ , a constant, is the maximum velocity of contraction.

The fundamental equation for contractility  $C_c$ , which characterizes the density of cross-bridge formation within the fibers of the patch (the region within the heart muscle where contraction and cross-bridge formation happens), is

$$\begin{aligned} \dot{C}_c &= \frac{dC_c}{dt} \\ &= f_c^{\text{rise}}(t) C_c^s(L_c^{\text{cont}}) - f_c^{\text{decay}}(t) C_c. \end{aligned} \quad (3.12)$$

In (3.12), sarcomere contractility rises according to the function  $f_c^{\text{rise}}$ , which represents a phenomenological rate of cross-bridge formation within the patch and is expressed as

$$\begin{aligned} f_c^{\text{rise}}(t) &= \frac{1}{t_c^{\text{rise}}} 0.02 x_c^3 (8 - x_c)^2 \exp(-x_c), \\ x_c(t) &= \min \left( 8, \max \left( 0, \frac{t - t_c^{\text{act}}}{t_c^{\text{rise}}} \right) \right), \end{aligned} \quad (3.13)$$

depending on the time of onset of activation of the patch,  $t_c^{\text{act}}$ , and the rising time

$$t_c^{\text{rise}} = 0.55 \tau^R t_c^{\text{act,ref}}, \quad (3.14)$$

where  $\tau^R$  is a constant and  $t_c^{\text{act,ref}}$  is the reference duration of contraction for initial fiber length. Sarcomere contractility in (3.12) decays according to the function  $f_c^{\text{decay}}$ , which is expressed as

$$\begin{aligned} f_c^{\text{decay}}(t) &= \frac{1}{2t_c^{\text{decay}}} \left[ 1 + \sin \left( \text{sign}(y_c) \min \left( \frac{\pi}{2}, |y_c| \right) \right) \right], \\ y_c(t) &= \frac{t - t_c^{\text{act}} - t_c^{\text{act,dur}}}{t_c^{\text{decay}}}, \end{aligned} \quad (3.15)$$

which depends on the decay time

$$t_c^{\text{decay}} = 0.33 \tau^D t_c^{\text{act,ref}}, \quad (3.16)$$

where  $\tau^D$  is a constant and  $t_c^{\text{act,dur}}$  is the duration of contraction of the fiber that lengthens with sarcomere length:

$$t_c^{\text{act,dur}} = (0.65 + 1.0570 L_c^{\text{norm}}) t_c^{\text{act,ref}}. \quad (3.17)$$

The normalized sarcomere length for active contraction  $L_c^{\text{norm}}$  is computed as

$$L_c^{\text{norm}} = \max \left( 0.0001, \frac{L_c^{\text{cont}}}{L_c^{\text{act0,ref}}} - 1 \right), \quad (3.18)$$

where  $L_c^{\text{act0,ref}}$  is the zero active stress sarcomere length.

In (3.12),  $C_c^s$  describes the increase in cross-bridge formation with intrinsic sarcomere length due to an increase in available binding sites,

$$C_c^s(L_c^{\text{cont}}) = \tanh(0.75 \cdot 9.1204 (L_c^{\text{norm}})^2). \quad (3.19)$$

Contractility  $C_c$  (3.12) and sarcomere contracting length  $L_c^{\text{cont}}$  (3.11) are used to compute the actively generated fiber stress

$$\sigma_c^{\text{fib,act}} = L_c^{\text{act0,ref}} \sigma^{\text{act,max}} C_c L_c^{\text{norm}} \frac{L_c^s - L_c^{\text{cont}}}{L_c^{\text{elast,iso}}}, \quad (3.20)$$

where  $L_c^{\text{act0,ref}}$ ,  $\sigma^{\text{act,max}}$ ,  $L_c^{\text{elast,iso}}$  are constants.

### Sarcomere Passive Stress

In the model the passive stress  $\sigma_c^{\text{fib,pas}}$  is considered to consist of two components:

$$\sigma_c^{\text{fib,pas}} = \sigma_c^{\text{fib,tit}} + \sigma_c^{\text{fib,ecm}}. \quad (3.21)$$

Here,  $\sigma_c^{\text{fib,tit}}$  is the stress arising from cellular structures such as titin, a highly abundant structural protein of the sarcomere, anchoring to the Z-disc, and  $\sigma_c^{\text{fib,ecm}}$  is the stress arising from the extracellular matrix (ECM). Both depend on the passive fiber stretch which is computed as

$$\lambda_c^{\text{pas}} = \frac{L_c^s}{L_c^{\text{pas0,ref}}}, \quad (3.22)$$

where  $L_c^{\text{pas0,ref}}$  is the sarcomere length with zero passive stress and  $L_c^s$  is the total sarcomere length (3.10). We can compute

$$\sigma_c^{\text{fib,tit}} = 0.01 \sigma^{\text{act,max}} \left( (\lambda_c^{\text{pas}})^{k^{\text{tit}}} - 1 \right), \quad (3.23)$$

where  $\sigma^{\text{act,max}}$  is the maximal isometric stress and the constant exponent is expressed as

$$k^{\text{tit}} = 2 \frac{L^{s,\text{ref}}}{dL^{s,\text{pas}}}. \quad (3.24)$$

The ECM is modeled as being stiffer than the myocyte contribution using

$$\sigma_c^{\text{fib,ecm}} = 0.0349 \sigma^{\text{pas,max}} ((\lambda_c^{\text{pas}})^{10} - 1), \quad (3.25)$$

where  $\sigma^{\text{pas,max}}$  is an empirical parameter.

### Sarcomere Total Stress

Total myofiber stress  $\sigma_c^{\text{fib}}$  is the sum of an active (3.20) and a passive (3.21) stress component:

$$\sigma_c^{\text{fib}} = \sigma_c^{\text{fib,act}} + \sigma_c^{\text{fib,pas}}. \quad (3.26)$$

Sarcomere stiffness  $\kappa_c^{\text{fib}}$  is computed as the derivative of total fiber stress (3.26) with respect to fiber strain (3.9):

$$\kappa_c^{\text{fib}} = \frac{\partial \sigma_c^{\text{fib}}}{\partial E_c^{\text{fib}}} = \frac{\partial \sigma_c^{\text{fib,act}}}{\partial E_c^{\text{fib}}} + \frac{\partial \sigma_c^{\text{fib,pas}}}{\partial E_c^{\text{fib}}}, \quad (3.27)$$

where

$$\begin{aligned} \frac{\partial \sigma_c^{\text{fib,act}}}{\partial E_c^{\text{fib}}} &= L^{\text{act0,ref}} \sigma^{\text{act,max}} C_c L_c^{\text{norm}} \frac{L_c^s}{L_{\text{elast,iso}}}, \\ \frac{\partial \sigma_c^{\text{fib,pas}}}{\partial E_c^{\text{fib}}} &= 0.01 k^{\text{tit}} \sigma^{\text{act,max}} (\lambda_c^{\text{pas}})^{k^{\text{tit}}} + 0.0349 \cdot 10 \sigma^{\text{pas,max}} (\lambda_c^{\text{pas}})^{10}. \end{aligned} \quad (3.28)$$

## 4 Chamber Module

### 4.1 The CircAdapt Formulation

In CircAdapt, a chamber module represents a cavity with a wall that contains myofibers [2]. An actively contracting chamber  $c \in \{\text{LV, RV, LA, RA}\}$  is modeled using the state variables volume  $V_c$ , the length of the contractile element of the sarcomere  $L_c^{\text{cont}}$  (3.11), and the contractility  $C_c$  (3.12). Volume changes driven by inflow and outflow of blood induce changes in midwall volume  $V_c^{\text{mid}}$  and area  $A_c^{\text{mid}}$  [3].

Note that the ventricles are modeled using the TriSeg formulation, see [Section 5](#).

### Sphere Mechanics

Midwall volume  $V_c^{\text{mid}}$  is estimated as

$$V_c^{\text{mid}} = V_c + \frac{1}{2} V_c^{\text{wall}}, \quad (3.29)$$

where  $V_c^{\text{wall}}$  is the constant wall volume. If it is not set to a specific value, the wall volume is estimated by extruding the sphere enclosing the cavity volume  $V_c$  by a constant wall thickness  $h_c^{\text{wall}}$ . Chambers are modeled as closed spheres, thus, the following equations result from volume and surface formulas for spheres

$$C_c^{\text{mid}} = \left( \frac{4\pi}{3V_c^{\text{mid}}} \right)^{1/3}, \quad (3.30)$$

$$A_c^{\text{mid,tot}} = \frac{4\pi}{(C_c^{\text{mid}})^2}, \quad (3.31)$$

$$A_c^{\text{mid}} = A_c^{\text{mid,tot}} - A_c^{\text{mid,dead}}, \quad (3.32)$$

where  $C_c^{\text{mid}}$  is the midwall curvature; and  $A_c^{\text{mid,dead}}$  is non-contractile area, i.e., valve openings and orifices.

### Update Fiber Strain

The natural fiber strain  $E_c^{\text{fib}}$  is calculated as

$$E_c^{\text{fib}} = \frac{1}{2} \ln \left( \frac{A_c^{\text{mid}}}{A_c^{\text{mid,ref}}} \right), \quad (3.33)$$

where  $A_c^{\text{mid,ref}}$  is the surface area in the reference state, see [14].

Cross-sectional area  $A_c$  of chambers is estimated as

$$\begin{aligned} A_c &= \frac{V_c + 0.1V_c^{\text{wall}}}{l_c}, \\ l_c &= 2(V_c^{\text{mid}})^{1/3}, \end{aligned} \quad (3.34)$$

where  $l_c$  is the long-axis length of the cavity.

The characteristic wave impedance  $Z_c$  is approximated according to (3.7), see also [2], and by applying the chain rule:

$$Z_c = \frac{1}{5A_c} \sqrt{\rho_b l_c |\kappa_c^{\text{mid}}|}, \quad (3.35)$$

where the sheet stiffness is computed as

$$\kappa_c^{\text{mid}} = \frac{\partial T_c^{\text{mid}}}{\partial A_c^{\text{mid}}} = \frac{V_c^{\text{wall}}}{4(A_c^{\text{mid}})^2} \left( \frac{\partial \sigma_c^{\text{fib}}}{\partial E_c^{\text{fib}}} - 2\sigma_c^{\text{fib}} \right) = \frac{V_c^{\text{wall}}}{4(A_c^{\text{mid}})^2} (\kappa_c^{\text{fib}} - 2\sigma_c^{\text{fib}}) \quad (3.36)$$

and  $\kappa_c^{\text{fib}}$  is the updated fiber stiffness, see (3.27).

### Conservation of Energy

The midwall tension  $T_c^{\text{mid}}$  and midwall area  $A_c^{\text{mid}}$  are connected to fiber stress  $\sigma_c^{\text{fib}}$  and strain  $E_c^{\text{fib}}$  through the law of conservation of energy.

With the law of Laplace we get:

$$T_c^{\text{mid}} dA_c^{\text{mid}} = \sigma_c^{\text{fib}} V_c^{\text{wall}} dE_c^{\text{fib}}, \quad (3.37)$$

and with (3.33) we get for the midwall tension:

$$T_c^{\text{mid}} = \frac{\sigma_c^{\text{fib}} V_c^{\text{wall}}}{2A_c^{\text{mid}}}. \quad (3.38)$$

The transmural pressure  $p_c^{\text{trans}}$  is finally computed as:

$$p_c^{\text{trans}} = 2T_c^{\text{mid}} C_c^{\text{mid}}. \quad (3.39)$$

Since external pressures are assumed to be zero, the transmural pressure coincides with the internal pressure of the contracting chamber:

$$p_c = p_c^{\text{trans}}. \quad (3.40)$$

## 5 TriSeg Model of Ventricular Interaction

### 5.1 The CircAdapt Formulation

Ventricular and septal midwall volumes are modeled as a ventricular composite [7] which is defined by the common radius  $y^{mid}$  of the wall junction and the enclosed midwall cap volumes, see [Figure 3.4](#) [3]. Midwall cap volumes of the right and the left ventricle are computed as

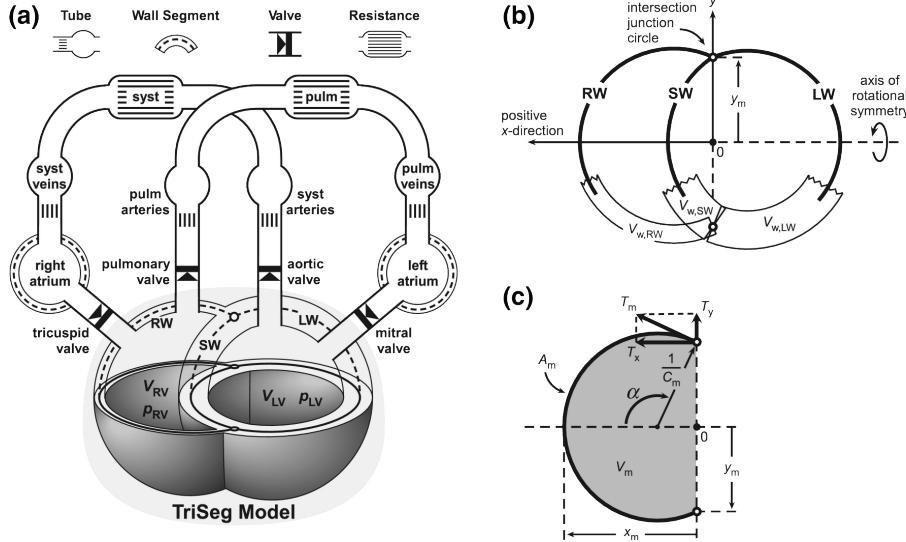


**Figure 3.4:** TriSeg model of septal and left and right ventricular mechanics. (a) The TriSeg model (gray shading) incorporated in the modular CircAdapt model of the systemic (Syst) and pulmonary (Pulm) circulations. (b) Cross-section of the ventricular composite. (c) Cross-section of a single wall segment through the axis of rotational symmetry. Image kindly provided by the corresponding author of [3].

$$V_{LV}^{mid} = -V_{LV} + V_{Sep}^{mid} - \frac{1}{2} (V_{LV}^{wall} + V_{Sep}^{wall}),$$

$$V_{RV}^{mid} = V_{RV} + V_{Sep}^{mid} + \frac{1}{2} (V_{RV}^{wall} + V_{Sep}^{wall}).$$

Here, the wall volumes of the left,  $V_{LV}^{wall}$ , and right ventricle,  $V_{RV}^{wall}$ , are constants. The blood pool volumes of the left,  $V_{LV}$ , and right ventricle,  $V_{RV}$ , are ODE variables as well as the radius  $y^{mid}$  and the septal midwall volume  $V_{Sep}^{mid}$ . Note that the sign of midwall volume  $V_c^{mid}$  is positive if wall curvature is convex to the positive  $x$ -direction and negative otherwise.

The distance  $x_c^{mid}$ , see [Figure 3.4](#), is then computed by the relation

$$V_c^{mid} = \frac{\pi}{6} x_c^{mid} ((x_c^{mid})^2 + 3(y^{mid})^2), \quad \text{for } c \in \{LV, RV, Sep\}, \quad (3.41)$$

hence

$$x_c^{mid} = q_c - \frac{(y^{mid})^2}{q_c}, \quad \text{with } q_c = \sqrt[3]{\sqrt{\left(\frac{3}{\pi} V_c^{mid}\right)^2 + (y^{mid})^6} + \frac{3}{\pi} V_c^{mid}}. \quad (3.42)$$

The midwall area and curvature are consequently computed

$$A_c^{mid} = \pi ((x_c^{mid})^2 + (y^{mid})^2), \quad \text{for } c \in \{LV, RV, Sep\},$$

$$C_c^{mid} = \frac{2x_c^{mid}}{(x_c^{mid})^2 + (y^{mid})^2}, \quad \text{for } c \in \{LV, RV, Sep\},$$

and used to calculate midwall tension  $T_c^{mid}$  (3.38). The axial  $T_c^X$  and radial  $T_c^Y$  tension components are computed using the laws of trigonometry

$$\begin{aligned} T_c^X &= T_c^{mid} \sin \alpha, & \text{with } \sin \alpha &= \frac{2x_c^{mid}y^{mid}}{(x_c^{mid})^2 + (y^{mid})^2}, & \text{for } c \in \{LV, RV, Sep\}, \\ T_c^Y &= T_c^{mid} \cos \alpha, & \text{with } \cos \alpha &= \frac{-(x_c^{mid})^2 + (y^{mid})^2}{(x_c^{mid})^2 + (y^{mid})^2}, & \text{for } c \in \{LV, RV, Sep\}. \end{aligned}$$

It is required that the total midwall tension at junctions is zero, i.e.,

$$f(y^{mid}, V_{Sep}^{mid}) := \left( \frac{T_{LV}^X + T_{RV}^X + T_{Sep}^X}{T_{LV}^Y + T_{RV}^Y + T_{Sep}^Y} \right) \stackrel{!}{=} 0. \quad (3.43)$$

Equation (3.43) is solved by an iterative Newton scheme

$$f'(y_k^{mid}, V_{k,Sep}^{mid}) \begin{pmatrix} \Delta y_k^{mid} \\ \Delta V_{k,Sep}^{mid} \end{pmatrix} = -f(y_k^{mid}, V_{k,Sep}^{mid}), \quad k = 1, 2, \dots \quad (3.44)$$

and the increments  $\Delta y_k^{mid}$  and  $\Delta V_{k,Sep}^{mid}$  are added to  $y_k^{mid}$  and  $V_{k,Sep}^{mid}$ . The solution of (3.44) in the first step, i.e., for  $k = 0$  is used to define the ODE updates for the septum

$$\dot{V}_{Sep}^{mid} = \frac{1}{\tau_{Sep}} \Delta V_{0,Sep}^{mid}, \quad \dot{y}^{mid} = \frac{1}{\tau_{Sep}} \Delta y_0^{mid}, \quad (3.45)$$

where  $\tau_{Sep}$  is a time constant. Consequently, the values for the tensions discussed above are updated and the scheme is iterated until convergence. Midwall volumes are updated by

$$V_c^{mid} = V_c + \frac{1}{2} (V_c^{wall} + V_{Sep}^{wall}), \quad (3.46)$$

the long-axis length  $l_c$  and cross-sectional area  $A_c$  and of the cavity are computed by

$$l_c = 2 \left( V_c^{mid} + \frac{1}{2} (V_c^{wall} + V_{Sep}^{wall}) \right)^{1/3}, \quad (3.47)$$

$$A_c = \frac{V_c^{mid} + \frac{1}{20} (V_c^{wall} + V_{Sep}^{wall})}{l_c}. \quad (3.48)$$

Finally, the wave impedance  $Z_c$  is computed according to (3.35) and the transmural pressure  $p_c^{trans}$  is computed as the total axial force

$$p_c^{trans} = 2 \frac{T_c^X}{y_c^{mid}}, \quad \text{for } c \in \{LV, RV, Sep\}. \quad (3.49)$$

Assuming the pressure surrounding the ventricular composite to be zero, internal chamber pressure for the ventricles is now found as

$$p_{LV} = -p_{LV}^{trans}, \quad p_{RV} = p_{RV}^{trans}. \quad (3.50)$$

## 6 Pericardial Mechanics

### 6.1 The CircAdapt Formulation

Due to the pericardium, the four cardiac chambers are supposed to have an additional pressure component [3]. The pressure  $p_{\text{peri}}$  exerted by the pericardial sac on the atria and ventricles is determined as a non-linear function of the pericardial volume  $V_{\text{peri}}$ , which is calculated as the sum of the blood pool and wall volumes of the four cardiac chambers:

$$V_{\text{peri}} = V_{\text{LV}} + V_{\text{RV}} + V_{\text{LA}} + V_{\text{RA}} + V_{\text{LV}}^{\text{wall}} + V_{\text{RV}}^{\text{wall}} + V_{\text{LA}}^{\text{wall}} + V_{\text{RA}}^{\text{wall}}, \quad (3.51)$$

$$p_{\text{peri}} = p_{\text{peri}}^{\text{ref}} \left( \frac{V_{\text{peri}}}{V_{\text{peri}}^{\text{ref}}} \right)^{k_{\text{peri}}}, \quad (3.52)$$

where  $p_{\text{peri}}^{\text{ref}}$  and  $V_{\text{peri}}^{\text{ref}}$  are constant reference pressure and volume, respectively, and  $k_{\text{peri}}$  defines the degree of non-linearity of the pressure-volume relation.

Cavity pressures are updated according to:

$$p_c = p_c + p_{\text{peri}}, \quad \text{for } c \in \{\text{LV, RV, LA, RA}\}. \quad (3.53)$$

## 7 Periphery

### 7.1 The CircAdapt Formulation

In the CircAdapt model, the peripheral vasculature in both the pulmonary and systemic circuits is represented as resistances. The pressure drop across these resistances, calculated as the difference between the inflow artery and outflow vein pressures, drives blood flow. This concept mirrors how vascular tone adjusts vessel diameter to regulate blood flow. CircAdapt also uses reference values and scaling factors to simulate the nonlinearity of arteriovenous resistances, similar to how autoregulation maintains steady blood flow despite pressure changes. This approach helps mimic the dynamic control of blood flow observed in physiological conditions [3].

#### Mathematical Formulation

Pulmonary (*pulm*) and systemic (*sys*) periphery are modeled as resistances. The current pressure drop  $\Delta p_{py}$ , for  $py \in \{\text{pulm, sys}\}$ , is computed as:

$$\Delta p_{py} = p_t^{\text{prox}} - p_t^{\text{dist}}, \quad (3.54)$$

hence as the difference of the pressures in the inflow artery  $p_t^{\text{prox}}$  and the outflow vein  $p_t^{\text{dist}}$ . Using this, the current flow over the periphery is

$$q_{py} = q_{py}^{\text{ref}} \left( r_{py} \left( \frac{\Delta p_{py}}{\Delta p_{py}^{\text{ref}}} \right) \right)^{k_{py}}, \quad (3.55)$$

where  $\Delta p_{py}^{\text{ref}}$  is the reference arteriovenous pressure drop;  $q_{py}^{\text{ref}}$  is the reference flow over the periphery;  $r_{py}$  is a scaling factor of the arteriovenous resistances; and  $k_{py}$  is a factor that accounts for the nonlinearity of the arteriovenous resistances.

## 8 Connecting the Modules

Now consider the modules discussed in [Section 2](#), [Section 3](#), [Section 4](#), [Section 6](#), and [Section 7](#). The CircAdapt model connects these modules as follows.

### 8.1 Volume Change of Inflow Arteries and Outflow Veins

Volume change of inflow arteries  $\dot{V}_t^{\text{prox}}$  and outflow veins  $\dot{V}_t^{\text{dist}}$  is updated by

$$\dot{V}_t^{\text{dist}}+ = q_{py}, \quad \dot{V}_t^{\text{prox}}+ = q_{py}. \quad (3.56)$$

Computation of time derivative of flow across valves and venous-atrial inlet requires as input the cross-sectional area of proximal and distal elements to the channel [3]. Hence we obtain:

$$\dot{V}_{c,t}^{\text{dist}}+ = q_v, \quad \dot{V}_{c,t}^{\text{prox}}+ = q_v, \quad (3.57)$$

and

$$p_{c,t}^{\text{prox}}+ = \dot{V}_{c,t}^{\text{prox}} Z_{c,t}^{\text{prox}}, \quad p_{c,t}^{\text{dist}}+ = \dot{V}_{c,t}^{\text{dist}} Z_{c,t}^{\text{dist}}. \quad (3.58)$$

## 9 Valve Dynamics

### 9.1 The CircAdapt Formulation

The pressure drop  $\Delta p_v$  across a valve results from the combined effects of inertial forces due to time-dependent acceleration and the Bernoulli effect [6] which, using  $v_v = q_v/A_v$ , leads to:

$$\Delta p_v = \rho_b \frac{l_v}{A_v} \dot{q}_v + \frac{\rho_b}{2} ((v_v^{\text{out}})^2 - (v_v^{\text{in}})^2), \quad (3.59)$$

where  $\rho_b$  is the density of blood,  $A_v$  is the current cross-sectional area of the valve, and  $l_v$  is the length of the channel with inertia [3]. It is estimated as

$$l_v = \sqrt{A_v^{\text{open}}}, \quad (3.60)$$

where  $A_v^{\text{open}}$  is the given cross-sectional area of the open valve.

For  $q_v \geq 0$ ,  $v_v^{\text{in}}$  refers to the velocity proximal to the valve, denoted as  $v_v^{\text{prox}}$ , while  $v_v^{\text{out}}$  represents the maximum blood velocity in the valve region, given by  $v_v^{\text{max}} = \max(v_v^{\text{dist}}, v_v, v_v^{\text{prox}})$ .

For  $q_v < 0$ , which is the case when the valve is leaking,  $v_v^{\text{in}}$  is the velocity distal to the valve, denoted as  $v_v^{\text{dist}}$ , and the outflow velocity,  $v_v^{\text{out}}$ , is the maximum blood velocity in the valve region, given by  $v_v^{\text{out}} = v_v^{\text{max}}$ .

Using the definition of  $v_v$  we can write

$$\Delta p_v = p_v^{\text{prox}} - p_v^{\text{dist}} = \alpha_v \dot{q}_v + \beta_v q_v^2 \quad (3.61)$$

where

$$\alpha_v = \rho_b \frac{l_v}{A_v}, \quad (3.62)$$

is the inertia of the channel.

The open or closed status of the valve depends on the pressure drop and flow. Valves are distinctly open or closed when both the pressure drop and flow direction are aligned. When

there is a forward pressure drop, the valve opens immediately. Conversely, with a backward pressure drop and forward flow, the valve closes gradually, governed by a continuous function.

$$\begin{aligned} A_v^{\text{closing}} &= \sqrt{\frac{x_v}{x_v^2 + \Delta p_v^2}} (A_v^{\text{open}} - A_v^{\text{leak}}) + A_v^{\text{leak}}, \\ x_v &= \frac{40 \rho_b q_v |q_v|}{(A_v^{\text{open}})^2}, \end{aligned} \quad (3.63)$$

where  $A_v^{\text{leak}}$  is the given valve cross-sectional area of the closed (regurgiting) valve. The current cross-sectional area of the valve is

$$A_v = \begin{cases} A_v^{\text{open}} & \text{for } \Delta p_v > 0, \\ A_v^{\text{leak}} & \text{for } \Delta p_v < 0 \text{ and } q_v < 0, \\ A_v^{\text{closing}} & \text{for } \Delta p_v < 0 \text{ and } q_v > 0. \end{cases} \quad (3.64)$$

We define

$$A_v^{\min} = \min(A_v^{\text{prox}}, A_v, A_v^{\text{dist}}), \quad (3.65)$$

where  $A_v^{\text{prox}}$  and  $A_v^{\text{dist}}$  are the cross-sectional areas of the proximal and distal cavities or tubes respectively, see (3.1), (3.34), and **Figure 3.5**. Using this,  $\beta_v$  is given as

$$\beta_v = \begin{cases} \frac{1}{2} \rho_b \left[ \left( \frac{1}{A_v^{\min}} \right)^2 - \left( \frac{1}{A_v^{\text{prox}}} \right)^2 \right] & \text{for } q_v \geq 0, \\ \frac{1}{2} \rho_b \left[ \left( \frac{1}{A_v^{\text{dist}}} \right)^2 - \left( \frac{1}{A_v^{\min}} \right)^2 \right] & \text{for } q_v < 0. \end{cases} \quad (3.66)$$

Flow over the valve is finally updated using (3.61) by

$$\dot{q}_v = \frac{\Delta p_v - \beta_v q_v^2}{\alpha_v}. \quad (3.67)$$

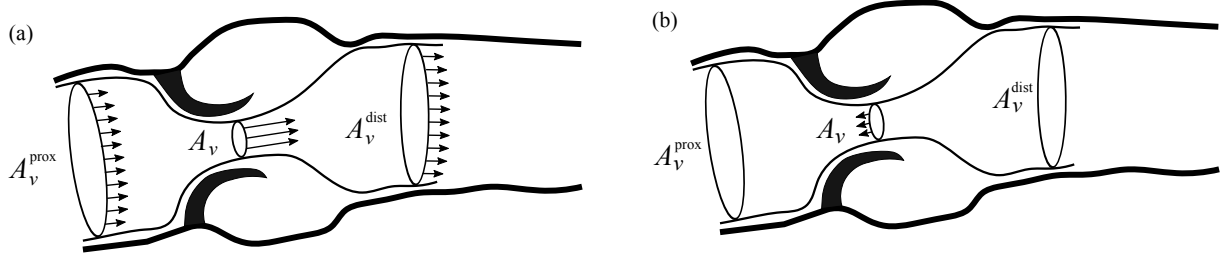


**Figure 3.5:** Schematic of the (a) open and (b) regurgitating valve. Image kindly provided by the corresponding author of [3].

## 10 Solving the ODE System

The system of 26 ordinary differential equations (ODE) is composed by:

- ▷ 8 ODEs: for each of the four tubes and the four cavities we get an ODE to update the volume using (3.56) and (3.57).
- ▷ 2 ODEs: for the septum we update midwall volume and the radius according to (3.45).
- ▷ 10 ODEs: for the sarcomeres of each cavity and the septum we update sarcomere contracting length and contractility using (3.11) and (3.12).
- ▷ 6 ODEs: for each of the four valves and the two outlets we update flow by (3.67).

The system of ordinary differential equations is solved using the forward Euler method, which will be explained in the remainder of this section.

### 10.1 Introduction to the Numerical Analysis

#### The Cauchy Problem

The Cauchy problem consists of finding the solution of an ODE, in the scalar or vector case, given suitable initial conditions [11]. In particular, in the scalar case, denoting by  $I$  an interval of  $\mathbb{R}$  containing the point  $t_0$ , the Cauchy problem associated with a first-order ODE reads:

**Definition 3.1** (Cauchy problem). Find a real-valued function  $y \in C^1(I)$ , such that

$$\begin{cases} y'(t) = f(t, y(t)), & t \in I, \\ y(t_0) = y_0, \end{cases} \quad (3.68)$$

where  $f(t, y)$  is a given real-valued function in the strip  $S = I \times (-\infty, +\infty)$ , which is continuous with respect to both variables.

Should  $f$  depend on  $t$  only through  $y$ , the differential equation is called *autonomous*. If  $f$  is continuous with respect to  $t$ , then the solution to eq. (3.68) satisfies

$$y(t) - y_0 = \int_{t_0}^t f(\tau, y(\tau)) d\tau. \quad (3.69)$$

Conversely, if  $y$  is defined by (3.69), then it is continuous in  $I$  and  $y(t_0) = y_0$ . Moreover, since  $y$  is a primitive of the continuous function  $f(\cdot, y(\cdot))$ ,  $y \in C^1(I)$  and satisfies the differential equation  $y'(t) = f(t, y(t))$ . Thus, if  $f$  is continuous, the Cauchy problem eq. (3.68) is equivalent to the integral equation (3.69).

#### One-Step Numerical Methods

Fix  $0 < T < +\infty$  and let  $I = (t_0, t_0 + T)$  be the integration interval and, correspondingly, for  $h > 0$ , let  $t_n = t_0 + nh$ , with  $n = 0, 1, 2, \dots, N_h$ , be the sequence of discretization nodes of  $I$  into subintervals  $I_n = [t_n, t_{n+1}]$ . The width  $h$  of such subintervals is called the *discretization stepsize*. Let  $u_j$  be the approximation at node  $t_j$  of the exact solution  $y(t_j)$ ; this solution will be denoted by  $y_j$ . Similarly,  $f_j$  denotes the value  $f(t_j, u_j)$ . We set  $u_0 = y_0$ .

**Definition 3.2** (One-step method). A numerical method for the approximation of problem (3.68) is called a *one-step method* if  $\forall n \geq 0$ ,  $u_{n+1}$  depends only on  $u_n$ . Otherwise, the scheme is called a *multistep method*.

**Definition 3.3** (Forward Euler Method). The *forward Euler method* is a one-step method defined as:

$$u_{n+1} = u_n + h f_n. \quad (3.70)$$

Hence,  $y'$  is approximated through a forward finite difference, which is a first-order approximation of the first derivative of  $y$  with respect to  $h$ .

**Definition 3.4.** A method is called *explicit* if  $u_{n+1}$  can be computed directly in terms of (some of) the previous values  $u_k$ ,  $k \leq n$ , *implicit* if  $u_{n+1}$  depends implicitly on itself through  $f$ .

Hence, the forward Euler method (3.70) is an explicit method.

## 10.2 Analysis of One-step Methods

Any one-step explicit method for the approximation of (3.68) can be cast in the concise form:

$$u_{n+1} = u_n + h \Phi(t_n, u_n, f_n; h), \quad 0 \leq n \leq N_h - 1, \quad u_0 = y_0, \quad (3.71)$$

where  $\Phi(\cdot, \cdot, \cdot; \cdot)$  is called an *increment function* [11]. Letting as usual  $y_n = y(t_n)$ , analogously to (3.71) we can write:

$$y_{n+1} = y_n + h \Phi(t_n, y_n, f(t_n, y_n); h) + \varepsilon_{n+1}, \quad 0 \leq n \leq N_h - 1, \quad (3.72)$$

where  $\varepsilon_{n+1}$  is the residual arising at the point  $t_{n+1}$  when we pretend that the exact solution “satisfies” the numerical scheme. We write the residual as:

$$\varepsilon_{n+1} = h \tau_{n+1}(h).$$

The quantity  $\tau_{n+1}(h)$  is called the *local truncation error* (LTE) at the node  $t_{n+1}$ . We define the *global truncation error* as:

$$\tau(h) = \max_{0 \leq n \leq N_h - 1} |\tau_{n+1}(h)|.$$

Notice that  $\tau(h)$  depends on the solution  $y$ .

The forward Euler method is a special instance of (3.71), where

$$\Phi(t_n, u_n, f_n; h) = f_n.$$

A one-step explicit scheme is fully characterized by its increment function  $\Phi$ . This function, in all the cases considered thus far, is such that

$$\lim_{h \rightarrow 0} \Phi(t_n, y_n, f(t_n, y_n); h) = f(t_n, y_n), \quad \forall t_n \geq t_0. \quad (3.73)$$

Property (3.73), together with the obvious relation  $y_{n+1} - y_n = hy'(t_n) + \mathcal{O}(h^2)$ ,  $\forall n \geq 0$ , allows one to obtain from (3.72) that  $\lim_{h \rightarrow 0} \tau_{n+1}(h) = 0$ ,  $0 \leq n \leq N_h - 1$ . In turn, this condition ensures that

$$\lim_{h \rightarrow 0} \tau(h) = 0,$$

which expresses the *consistency* of the numerical method (3.71) with the Cauchy problem (3.68). We can then write the following definition.

**Definition 3.5** (Consistent method). A method is said to be consistent if its LTE is infinitesimal with respect to  $h$ .

Then we can define the *order* as follows.

**Definition 3.6** (Order of a scheme). A scheme has order  $p$  if,  $\forall t \in I$ , the solution  $y(t)$  of the Cauchy problem (3.68) fulfills the condition

$$\tau(h) = \mathcal{O}(h^p) \quad \text{for } h \rightarrow 0. \quad (3.74)$$

Using Taylor expansions it can be proved that the forward Euler method has order 1.

### 10.3 The Zero-Stability

In view of the stability analysis, we consider the following problem [11].

**Definition 3.7** (Perturbed Cauchy problem). The *perturbed Cauchy problem* is defined as:

$$\begin{cases} z'(t) = f(t, z(t)) + \delta(t), & t \in I, \\ z(t_0) = y_0 + \delta_0, \end{cases} \quad (3.75)$$

where  $\delta_0 \in \mathbb{R}$  and  $\delta$  is a continuous function on  $I$ . Problem (3.75) is derived from (3.68) by perturbing both the initial datum  $y_0$  and the function  $f$ .

Let us now characterize the sensitivity of the solution  $z$  to those perturbations.

**Definition 3.8** (Stability and asymptotical stability for the Cauchy problem). Let  $I$  be a bounded set. The Cauchy problem (3.68) is *stable in the sense of Ljapunov* (or *stable*) on  $I$  if, for any perturbation  $(\delta_0, \delta(t))$  satisfying

$$|\delta_0| < \varepsilon, \quad |\delta(t)| < \varepsilon \quad \forall t \in I,$$

with  $\varepsilon > 0$  sufficiently small to guarantee that the solution to the perturbed problem (3.75) does exist, then

$$\exists C > 0 \text{ such that } |y(t) - z(t)| < C\varepsilon, \quad \forall t \in I. \quad (3.76)$$

The constant  $C$  depends in general on problem data  $t_0$ ,  $y_0$  and  $f$ , but not on  $\varepsilon$ .

If  $I$  has no upper bound we say that (3.68) is *asymptotically stable* if, as well as being Ljapunov stable in any bounded interval  $I$ , the following limit also holds

$$|y(t) - z(t)| \rightarrow 0, \quad \text{for } t \rightarrow +\infty, \quad (3.77)$$

provided that  $\lim_{t \rightarrow +\infty} |\delta(t)| = 0$ .

If (3.76) is satisfied with a constant  $C$  independent of  $h$ , we shall say that the numerical problem is zero-stable. Precisely:

**Definition 3.9** (Zero-stability of one-step methods). The numerical method (3.71) for the approximation of problem (3.68) is *zero-stable* if  $\exists h_0 > 0$ ,  $\exists C > 0$  such that  $\forall h \in (0, h_0]$ ,  $\forall \varepsilon > 0$  sufficiently small, if  $|\delta_n| \leq \varepsilon$ ,  $0 \leq n \leq N_h$ , then

$$|z_n^{(h)} - u_n^{(h)}| \leq C\varepsilon, \quad 0 \leq n \leq N_h, \quad (3.78)$$

where  $z_n^{(h)}$ ,  $u_n^{(h)}$  are respectively the solutions of the problems

$$\begin{cases} z_{n+1}^{(h)} = z_n^{(h)} + h \left[ \Phi(t_n, z_n^{(h)}, f(t_n, z_n^{(h)}); h) + \delta_{n+1} \right], \\ z_0^{(h)} = y_0 + \delta_0, \end{cases} \quad (3.79)$$

$$\begin{cases} u_{n+1}^{(h)} = u_n^{(h)} + h \Phi(t_n, u_n^{(h)}, f(t_n, u_n^{(h)}); h), \\ u_0^{(h)} = y_0, \end{cases} \quad (3.80)$$

for  $0 \leq n \leq N_h - 1$ .

Both constants  $C$  and  $h_0$  may depend on problem data  $t_0$ ,  $T$ ,  $y_0$  and  $f$ . Zero-stability thus requires that, in a bounded interval, (3.78) holds for any value  $h \leq h_0$ .

This property deals with the behavior of the numerical method in the limit case  $h \rightarrow 0$ . Property (3.78) ensures that the numerical method has a weak sensitivity with respect to small changes in the data.

The requirement for a numerical method to be stable primarily stems from the necessity to control the inevitable errors introduced by the finite precision of computer arithmetic. Indeed, if the numerical method were not zero-stable, the rounding errors made on  $y_0$  as well as in the process of computing  $f(t_n, u_n)$  would make the computed solution useless.

**Theorem 3.1** (Zero-stability). Consider the explicit one-step method (3.71) for the numerical solution of the Cauchy problem (3.68). Assume that the increment function  $\Phi$  is Lipschitz continuous with respect to the second argument, with constant  $\Lambda$  independent of  $h$  and of the nodes  $t_j \in [t_0, t_0 + T]$ , that is

$$\exists h_0 > 0, \exists \Lambda > 0 : \forall h \in (0, h_0]$$

$$|\Phi(t_n, u_n^{(h)}, f(t_n, u_n^{(h)}); h) - \Phi(t_n, z_n^{(h)}, f(t_n, z_n^{(h)}); h)| \leq \Lambda |u_n^{(h)} - z_n^{(h)}|, \quad 0 \leq n \leq N_h.$$

Then, method (3.71) is zero-stable.

In the specific case of the Euler method, checking the property of zero-stability can be done directly using the Lipschitz continuity of  $f$ .

## 10.4 Convergence Analysis for the Forward Euler Method

**Definition 3.10.** A method is said to be *convergent* if

$$\forall n = 0, \dots, N_h, \quad |u_n - y_n| \leq C(h),$$

where  $C(h)$  is an infinitesimal with respect to  $h$ . In that case, it is said to be *convergent with order p* if  $\exists C > 0$  such that  $C(h) = Ch^p$ .

The following theorem holds.

**Theorem 3.2** (Convergence). Under the same assumptions as in **Theorem 3.1**, we have

$$|y_n - u_n| \leq (|y_0 - u_0| + nh\tau(h))e^{nh\Lambda}, \quad 1 \leq n \leq N_h. \quad (3.81)$$

Therefore, if the consistency assumption (3.73) holds and  $|y_0 - u_0| \rightarrow 0$  as  $h \rightarrow 0$ , then the method is convergent. Moreover, if  $|y_0 - u_0| = \mathcal{O}(h^p)$  and the method has order  $p$ , then it is also convergent with order  $p$ .

A consistent and zero-stable method is thus convergent [11].

The convergence analysis for the forward Euler method now follows. In the first part of the proof we assume that any operation is performed in exact arithmetic and that  $u_0 = y_0$ . Denote by  $e_{n+1} = y_{n+1} - u_{n+1}$  the error at node  $t_{n+1}$  with  $n = 0, 1, \dots$  and notice that

$$e_{n+1} = (y_{n+1} - u_{n+1}^*) + (u_{n+1}^* - u_{n+1}),$$

where  $u_{n+1}^* = y_n + hf(t_n, y_n)$  is the solution obtained after one step of the forward Euler method starting from the initial datum  $y_n$ . Then

$$y_{n+1} - u_{n+1}^* = h\tau_{n+1}(h), \quad u_{n+1}^* - u_{n+1} = e_n + h[f(t_n, y_n) - f(t_n, u_n)].$$

As a consequence,

$$|e_{n+1}| \leq h|\tau_{n+1}(h)| + |e_n| + h|f(t_n, y_n) - f(t_n, u_n)| \leq h\tau(h) + (1 + hL)|e_n|,$$

$L$  being the Lipschitz constant of  $f$ . By recursion on  $n$ , we find

$$\begin{aligned} |e_{n+1}| &\leq [1 + (1 + hL) + \dots + (1 + hL)^n]h\tau(h) \\ &= \frac{(1 + hL)^{n+1} - 1}{L}\tau(h) \\ &\leq \frac{e^{L(t_{n+1}-t_0)} - 1}{L}\tau(h). \end{aligned}$$

The last inequality follows from noticing that  $1 + hL \leq e^{hL}$  and  $(n + 1)h = t_{n+1} - t_0$ . On the other hand, if  $y \in C^2(I)$ , the LTE for the forward Euler method is

$$\tau_{n+1}(h) = \frac{h}{2}y''(\xi), \quad \xi \in (t_n, t_{n+1}),$$

and thus,  $\tau(h) \leq (\frac{M}{2})h$ , where  $M = \max_{\xi \in I} |y''(\xi)|$ . In conclusion,

$$|e_{n+1}| \leq \frac{e^{L(t_{n+1}-t_0)} - 1}{L} \frac{M}{2}h, \quad \forall n \geq 0, \quad (3.82)$$

from which it follows that the error tends to zero with the same order as the local truncation error.

If also the rounding errors are accounted for, we can assume that the solution  $\bar{u}_{n+1}$ , actually computed by the forward Euler method at time  $t_{n+1}$ , is such that

$$\bar{u}_0 = y_0 + \zeta_0, \quad \bar{u}_{n+1} = \bar{u}_n + h f(t_n, \bar{u}_n) + \zeta_{n+1}, \quad (3.83)$$

having denoted the rounding error by  $\zeta_j$ , for  $j \geq 0$ . Problem (3.83) is an instance of (3.79), provided that we identify  $\zeta_{n+1}$  and  $\bar{u}_n$  with  $h\delta_{n+1}$  and  $z_n^{(h)}$  in (3.79), respectively. Combining **Theorem 3.1** and **Theorem 3.2** we get, instead of (3.82), the following error estimate

$$|y_{n+1} - \bar{u}_{n+1}| \leq e^{L(t_{n+1}-t_0)} \left[ |\zeta_0| + \frac{1}{L} \left( \frac{M}{2}h + \frac{\zeta}{h} \right) \right],$$

where  $\zeta = \max_{1 \leq j \leq n+1} |\zeta_j|$ . The presence of rounding errors does not allow, therefore, to conclude that as  $h \rightarrow 0$ , the error goes to zero. Actually, there exists an optimal (non-zero) value of  $h$ ,  $h_{\text{opt}}$ , for which the error is minimized. For  $h < h_{\text{opt}}$ , the rounding error dominates the truncation error and the error increases.

## 10.5 The Absolute Stability of the Forward Euler Method

The property of *absolute stability* is in some way specular to zero-stability, as far as the roles played by  $h$  and  $I$  are concerned [11]. Heuristically, we say that a numerical method is absolutely stable if, for  $h$  fixed,  $u_n$  remains bounded as  $t_n \rightarrow +\infty$ . This property, thus, deals with the asymptotic behavior of  $u_n$ , as opposed to a zero-stable method for which, for a fixed integration interval,  $u_n$  remains bounded as  $h \rightarrow 0$ .

For a precise definition, consider the linear Cauchy problem (that from now on, we shall refer to as the *test problem*)

$$\begin{cases} y'(t) = \lambda y(t), & t > 0, \\ y(0) = 1, \end{cases} \quad (3.84)$$

with  $\lambda \in \mathbb{C}$ , whose solution is  $y(t) = e^{\lambda t}$ . Notice that  $\lim_{t \rightarrow +\infty} |y(t)| = 0$  if  $\operatorname{Re}(\lambda) < 0$ .

**Definition 3.11** (Absolutely stable method). A numerical method for approximating (3.84) is *absolutely stable* if

$$|u_n| \rightarrow 0 \text{ as } t_n \rightarrow +\infty. \quad (3.85)$$

Let  $h$  be the discretization stepsize. The numerical solution  $u_n$  of (3.84) obviously depends on  $h$  and  $\lambda$ . Therefore, a method will be absolutely stable for certain values of  $h$  and  $\lambda$  and not for other values. More precisely, the *region of absolute stability* of the numerical method is defined as the subset of the complex plane

$$\mathcal{A} = \{z = h\lambda \in \mathbb{C} : (3.85) \text{ is satisfied}\}.$$

Thus,  $\mathcal{A}$  is the set of the values of the product  $h\lambda$  for which the numerical method furnishes solutions that decay to zero as  $t_n$  tends to infinity.

Regarding the forward Euler method: applying (3.70) to problem (3.84), yields  $u_{n+1} = u_n + h\lambda u_n$  for  $n \geq 0$ , with  $u_0 = 1$ . Proceeding recursively on  $n$  we get

$$u_n = (1 + h\lambda)^n, \quad n \geq 0.$$

Therefore, condition (3.85) is satisfied iff  $|1 + h\lambda| < 1$ , that is, if  $h\lambda$  lies within the unit circle with center at  $(-1, 0)$ . This amounts to requiring that

$$h\lambda \in \mathbb{C}^- \text{ and } 0 < h < -\frac{2\operatorname{Re}(\lambda)}{|\lambda|^2},$$

where

$$\mathbb{C}^- = \{z \in \mathbb{C} : \operatorname{Re}(z) < 0\}.$$

## 10.6 Example of Instability for the Forward Euler Method

Consider:

$$\begin{cases} y' = -2.3y, \\ y(0) = 1. \end{cases} \quad (3.86)$$

The exact solution of (3.86) is  $y(t) = e^{-2.3t}$ , which decays to zero as  $t \rightarrow \infty$ . However, if the Euler method is applied to this equation with step size  $h = 1$ , then the numerical solution is qualitatively wrong: it oscillates and grows (see [Figure 3.6](#)). If a smaller step size is used, for instance  $h = 0.7$ , then the numerical solution does decay to zero [4].

This implies that using this numerical method involves considering small step sizes to avoid similar instabilities.

## 10.7 Systems of ODEs

Let us consider the system of first-order ODEs

$$\mathbf{y}' = \mathbf{F}(t, \mathbf{y}), \quad (3.87)$$

where  $\mathbf{F} : \mathbb{R} \times \mathbb{R}^n \rightarrow \mathbb{R}^n$  is a given vector function and  $\mathbf{y} \in \mathbb{R}^n$  is the solution vector which depends on  $n$  arbitrary constants set by the  $n$  initial conditions

$$\mathbf{y}(t_0) = \mathbf{y}_0. \quad (3.88)$$

It is possible to write the solution to system (3.87) in closed form. A special case is where the system is linear and autonomous, that is

$$\mathbf{y}'(t) = A\mathbf{y}(t), \quad (3.89)$$

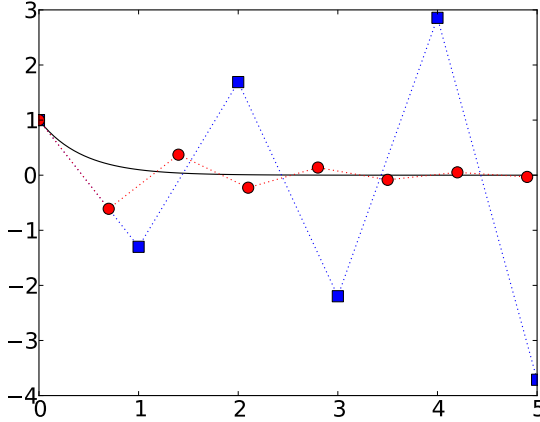


**Figure 3.6:** Solution of  $y' = -2.3y$  computed with the forward Euler method with step size  $h = 1$  (blue squares) and  $h = 0.7$  (red circles). The black curve shows the exact solution. Image attribution: Jitse Niesen, Instability of Euler's method, CC0 1.0.

with  $A \in \mathbb{R}^{n \times n}$ . Assume that  $A$  has  $n$  distinct eigenvalues  $\lambda_j$ ,  $j = 1, \dots, n$ ; therefore, the solution  $\mathbf{y}$  can be written as

$$\mathbf{y}(t) = \sum_{j=1}^n C_j e^{\lambda_j t} \mathbf{v}_j, \quad (3.90)$$

where  $C_1, \dots, C_n$  are some constants and  $\{\mathbf{v}_j\}$  is a basis formed by the eigenvectors of  $A$ , associated with the eigenvalues  $\lambda_j$  for  $j = 1, \dots, n$ . The solution is determined by setting  $n$  initial conditions.

From the numerical standpoint, the methods introduced in the scalar case can be extended to systems. A delicate matter is how to generalize the theory developed about absolute stability [11].

With this aim, consider system (3.89). As previously seen, the property of absolute stability is concerned with the behavior of the numerical solution as  $t$  grows to infinity, in the case where the solution of problem (3.87) satisfies

$$\|\mathbf{y}(t)\| \rightarrow 0 \text{ as } t \rightarrow \infty. \quad (3.91)$$

Condition (3.91) is satisfied if all the real parts of the eigenvalues of  $A$  are negative since this ensures that

$$e^{\lambda_j t} = e^{\operatorname{Re}(\lambda_j)t} (\cos(\operatorname{Im}(\lambda_j)t) + i \sin(\operatorname{Im}(\lambda_j)t)) \rightarrow 0, \text{ as } t \rightarrow \infty, \quad (3.92)$$

from which (3.91) follows recalling (3.90). Since  $A$  has  $n$  distinct eigenvalues, there exists a nonsingular matrix  $\mathbf{Q}$  such that  $\Lambda = \mathbf{Q}^{-1}A\mathbf{Q}$ ,  $\Lambda$  being the diagonal matrix whose entries are the eigenvalues of  $A$ .

Introducing the auxiliary variable  $\mathbf{z} = \mathbf{Q}^{-1}\mathbf{y}$ , the initial system can therefore be transformed into

$$\mathbf{z}' = \Lambda \mathbf{z}. \quad (3.93)$$

Since  $\Lambda$  is a diagonal matrix, the results holding in the scalar case immediately apply to the vector case as well, provided that the analysis is repeated on all the (scalar) equations of system (3.93).

## 11 Limitations of the CircAdapt Model

The CircAdapt code, widely used for simulating cardiovascular physiology, has certain limitations and complexities that users should be aware of. The most important of these is that, being a zero-dimensional (0D) representation, it inherently lacks the ability to account for wave propagation effects within the cardiovascular system. This simplification can lead to significant underestimations of important physiological phenomena. As a result, for these specific cases, the CircAdapt model may not be the most suitable approach. It is crucial to consider more complex models that incorporate wave dynamics to ensure a more comprehensive understanding and accurate representation of cardiovascular behavior.

Other limitations come from the reason why it was created and the implementation choices in the main versions (which can be found on the official website).

### 11.1 Educational Origins and Purpose

The CircAdapt platform was originally developed as a teaching tool for medical students. According to the website [5]:

*This website accommodates the CircAdapt source code (Matlab) as well as the CircAdapt Simulator, the latter being a user-friendly stand-alone simulation tool that can be used for education of cardiovascular physiology and pathophysiology. Both applications are developed with the aim to facilitate RESEARCH and EDUCATION in cardiovascular (patho-)physiology.*

This indicates that while the tool is beneficial for research, its primary design focus is educational, which may limit its suitability for more advanced or specific research applications.

### 11.2 Mass Conservation

Mass conservation within the CircAdapt model is a configurable code construct. It can be activated or deactivated via a flag. At the beginning of execution, during the adaptation phase, mass conservation is not enforced. It is only achieved upon convergence, provided the corresponding flag is set.

### 11.3 Negative Pressures

The CircAdapt code allows for the possibility of accepting negative pressures through the use of a specific flag. This means that the code will not produce an error if a negative pressure value is encountered. While this flexibility can be useful in certain pathological conditions or specific research scenarios, it also requires careful interpretation of the results.

### 11.4 Defects Activation

In the Matlab code of CircAdapt, certain defects (ventricular septal defect, atrial septal defect, ductus arteriosus opening) are always activated but kept small. This default setting might not be apparent to users and could potentially affect simulation outcomes.

---

# Bibliography

---

- [1] T. Arts et al. “**Relation between left ventricular cavity pressure and volume and systolic fiber stress and strain in the wall**”. In: *Biophysical Journal* 59.1 (Jan. 1991), pp. 93–102. DOI: [10.1016/s0006-3495\(91\)82201-9](https://doi.org/10.1016/s0006-3495(91)82201-9).
- [2] Theo Arts et al. “**Adaptation to Mechanical Load Determines Shape and Properties of Heart and Circulation: The CircAdapt Model**”. In: *American Journal of Physiology-Heart and Circulatory Physiology* 288.4 (Apr. 2005), H1943–H1954. DOI: [10.1152/ajpheart.00444.2004](https://doi.org/10.1152/ajpheart.00444.2004).
- [3] Christoph M. Augustin et al. “**A computationally efficient physiologically comprehensive 3D–0D closed-loop model of the heart and circulation**”. In: *Computer Methods in Applied Mechanics and Engineering* 386 (Dec. 2021), p. 114092. DOI: [10.1016/j.cma.2021.114092](https://doi.org/10.1016/j.cma.2021.114092).
- [4] J.C. Butcher. “**Numerical Methods for Ordinary Differential Equations**”. ISBN: 9780470753750. Wiley, 2008.
- [5] CircAdapt. *CircAdapt*. Available at <https://www.circadapt.org/>, accessed: July 9, 2024.
- [6] Michael Firstenberg et al. “**Noninvasive assessment of mitral inertance: Clinical results with numerical model validation**”. In: *Computers in cardiology* 28 (Feb. 2001). PMID: 14640109, pp. 613–6.
- [7] Joost Lumens et al. “**Three-Wall Segment (TriSeg) Model Describing Mechanics and Hemodynamics of Ventricular Interaction**”. In: *Annals of Biomedical Engineering* 37.11 (Nov. 2009), pp. 2234–2255. DOI: [10.1007/s10439-009-9774-2](https://doi.org/10.1007/s10439-009-9774-2).
- [8] Francesco Migliavacca et al. “**Modeling of the Norwood circulation: effects of shunt size, vascular resistances, and heart rate**”. In: *American Journal of Physiology-Heart and Circulatory Physiology* 280.5 (May 2001), H2076–H2086. DOI: [10.1152/ajpheart.2001.280.5.h2076](https://doi.org/10.1152/ajpheart.2001.280.5.h2076).
- [9] J.B. Olansen et al. “**A Closed-Loop Model of the Canine Cardiovascular System That Includes Ventricular Interaction**”. In: *Computers and Biomedical Research* 33.4 (Aug. 2000), pp. 260–295. DOI: [10.1006/cbmr.2000.1543](https://doi.org/10.1006/cbmr.2000.1543).
- [10] Giancarlo Pennati et al. “**A mathematical model of circulation in the presence of the bidirectional cavopulmonary anastomosis in children with a univentricular heart**”. In: *Medical Engineering’s Physics* 19.3 (Apr. 1997), pp. 223–234. DOI: [10.1016/s1350-4533\(96\)00071-9](https://doi.org/10.1016/s1350-4533(96)00071-9).
- [11] Alfio Quarteroni et al. “**Numerical Mathematics**”. Springer New York, 2007. DOI: [10.1007/b98885](https://doi.org/10.1007/b98885).
- [12] Y. Sun et al. “**A comprehensive model for right-left heart interaction under the influence of pericardium and baroreflex**”. In: *American Journal of Physiology-Heart and Circulatory Physiology* 272.3 (Mar. 1997), H1499–H1515. DOI: [10.1152/ajpheart.1997.272.3.h1499](https://doi.org/10.1152/ajpheart.1997.272.3.h1499).
- [13] J. D. Thomas et al. “**Physical and physiological determinants of pulmonary venous flow: numerical analysis**”. In: *American Journal of Physiology-Heart and Circulatory Physiology* 272.5 (May 1997), H2453–H2465. DOI: [10.1152/ajpheart.1997.272.5.h2453](https://doi.org/10.1152/ajpheart.1997.272.5.h2453).
- [14] John Walmsley et al. “**Fast Simulation of Mechanical Heterogeneity in the Electrically Asynchronous Heart Using the MultiPatch Module**”. In: *PLOS Computational Biology* 11.7 (July 2015). Ed. by Andrew D. McCulloch, e1004284. DOI: [10.1371/journal.pcbi.1004284](https://doi.org/10.1371/journal.pcbi.1004284).



---

## Coupling strategy

---

## Contents of the chapter

---

1	Model Adjustments for Coupling . . . . .	89
1.1	Components of the ADAVN Model . . . . .	89
1.2	Components of the CircAdapt Model . . . . .	89
2	Communication Between Models . . . . .	90
2.1	The AdavnTube Class in CircAdapt . . . . .	90
2.2	Options Configuration for the Coupled Model . . . . .	90
2.3	ADAVN Standalone Initialization . . . . .	90
2.4	Data Exchange . . . . .	90
2.5	Update Sequence . . . . .	91
2.6	Modification of Coronary Circulation Data Handling for CircAdapt Integration	92
3	Numerical Stability . . . . .	92
3.1	Monolithic vs. Data Exchange Approaches for Coupling . . . . .	92
3.2	Challenges with Segregated Methods in Coupling . . . . .	93
3.3	Time Stepping Strategy . . . . .	93

---

# 1 Model Adjustments for Coupling

After presenting a detailed explanation of the two main building blocks of the coupled model, ADANV in [Chapter 2](#) and CircAdapt in [Chapter 3](#), this chapter focuses on the modifications applied to both models. These adjustments, introduced in this work, were necessary to enable the coupling of the two models, allowing for their proper integration.

## 1.1 Components of the ADAVN Model

### Modification of Vessel Network for CircAdapt Coupling

In this work, only the systemic and coronary circulations from the reduced ADAVN model are utilized. From the full vessel network shown in [Figure 2.3](#), the pulmonary circulation, including the pulmonary vein, and pulmonary artery, as well as the heart, are removed from the model. By removing the pulmonary circulation and heart from the ADAVN model, the focus is entirely on the systemic vessels, allowing them to interact seamlessly with the 0D heart and pulmonary components provided by CircAdapt.

To achieve this, before disabling the heart and pulmonary circulation, an initialization of the standalone ADAVN model is performed to adjust the state of the vessels from the initial conditions. This initialization serves to bring the vessel states closer to the periodic state expected in the coupled model and to synchronize the two models, since at the start of the simulation, the ADAVN and CircAdapt models do not begin in the same phase of the cardiac cycle.

Once the initialization is complete, the heart and pulmonary circulation are disabled by setting the `hasHeart` variable to 0 during the coupling. This variable controls whether the ADAVN model executes the time evolution of heart and pulmonary circulation model, as well as the coupling of these components with the systemic circulation. At this point, the behavior of these functions is replaced with data coming from CircAdapt, as explained in [Section 2](#). For this purpose, new variables are added to the ADAVN model to receive and store information from CircAdapt, which are updated as the two models interact during the simulation.

## 1.2 Components of the CircAdapt Model

### Modification to the Systemic Circulation

In the CircAdapt model, the systemic circulation is simplified as two tubes representing the aorta and the vena cava connected by a resistive element. These components are thus removed to allow coupling with the systemic circulation module of the ADAVN model, while preserving the essential dynamics, including heart function, pulmonary circulation, sarcomere mechanics, and related processes as detailed in [Chapter 3](#).

In this adjustment, the systemic circulation is collapsed into a single tube that connects the systemic outlet, a fictitious valve at the entrance of the right atrium, to the aortic valve. The assignment of the variables which indicate the connected components, namely `out_comp` and `in_comp`, occurs during the connection of all cavities, specifically in the `ConnectTubes()` function, which is called within the `Initialize()` function of the model. In this process, `out_comp` is assigned to the systemic outlet element, and `in_comp` is assigned to the aortic valve.

Furthermore, similar adjustments were applied to the aortic valve and the systemic outlet. Both of these components are now specified to be connected to the systemic circulation rather than the vena cava and aorta.

## Integration of the ADAVN Model

To integrate the ADAVN model into the CircAdapt framework, several modifications were made to the Makefile. The necessary libraries for the ADAVN solver, such as `lib1dsolver.a`, `-lblas`, and other mathematical libraries, were added. Additionally, the paths for the solver's headers and libraries were specified to ensure that the system correctly includes and links all required files during the compilation and linking of the executable.

These changes ensure that the ADAVN model is included within the CircAdapt model by embedding it into a specially created tube class. This allows the creation of a model variable, enabling access to the functions and attributes of the ADAVN model directly within the CircAdapt framework.

# 2 Communication Between Models

## 2.1 The AdavnTube Class in CircAdapt

The class `AdavnTube` is designed similarly to other tube classes (e.g., `CircAdapt`, `Windkessel`, etc.) and inherits from the base class `Tube`. This inheritance ensures that `AdavnTube` maintains the same structure and variables as other tube classes, staying consistent with the overall framework. Like other tube classes, the main functions defined are `Initialize()`, `Update(double tm)`, and `UpdateState(double tm)` where `tm` is the actual time at which the functions are called.

## 2.2 Options Configuration for the Coupled Model

Before running the ADAVN model in standalone mode, several options are specified. These include the same duration of the cardiac cycle, the same time step used in the CircAdapt model, which in the case of ADAVN is set as the maximum time step limit for the LTS method (which defines the time at which all components of the systemic circulation will be synchronized, as explained in [Chapter 2](#)), the output folder for storing the results of the ADAVN model, and the initial pressures in arteries and veins.

## 2.3 ADAVN Standalone Initialization

In the `AdavnTube` class, in the `Initialize()` function, the standalone ADAVN model (including the heart and pulmonary circulation submodels) is first run for 1.7 s. Although the model does not achieve exact periodicity, the initialization phase allows the ADAVN model to adjust its output values to a range closer to that of the CircAdapt model. Also, since the two models begin the simulation at different phases of the cardiac cycle, it is necessary to initialize ADAVN at 1.7 seconds, equivalent to one full cardiac cycle and 0.7 of another, to synchronize both models in the same cardiac phase.

After the initialization of the ADAVN model, the heart component is disabled by setting `hasHeart=0` as specified previously.

## 2.4 Data Exchange

The `Update()` function of the `AdavnTube` class reads the time-averaged outflow value over a time interval from the CircAdapt aortic valve, as well as the pressure and volume values from the four heart chambers. The pressure and volume values from the heart chambers are used by ADAVN to update the coronary circulation model, while the outflow value from the aortic valve is used to impose a boundary condition at the inlet of the ascending aorta to update the

systemic circulation model, as explained in [Chapter 2, Section 5](#).

ADAVN now updates the systemic circulation and the coronary circulation modules for a time step. Following this, the CircAdapt model reads the values of cross-sectional area, pressure, and time-averaged flow over a time interval from the ADAVN model at the points where the coronary sinus, ascending aorta, superior vena cava, and inferior vena cava connect to the heart: specifically, from the initial spatial cell of the aorta and the terminal spatial cells of the other veins.

Finally, the `UpdateState()` function updates the internal variables of the `AdavnTube` class as follows. The outgoing flow variable is set to the sum of the time-averaged flows over a time interval from the three veins; the cross-sectional area variable is set to the sum of the cross-sectional areas of the veins; and the pressure variable is set to the pressure from the coronary sinus. This choice is arbitrary, as the other veins exhibit very similar pressures, and no significant differences are expected from using alternative pressures or their average. This information is necessary to update the systemic outlet, which behaves as a valve as explained in [Chapter 3, Section 9](#). Additionally, the pressure, cross-sectional area, and time-averaged flow values over a time interval from the ascending aorta of the ADAVN model are used to update the aortic valve model in CircAdapt.

A visual summary of the data exchange is depicted in [Figure 4.1](#).

It is worth noting that this integration is straightforward since both models are written in C++ using an object-oriented approach, allowing for seamless implementation.

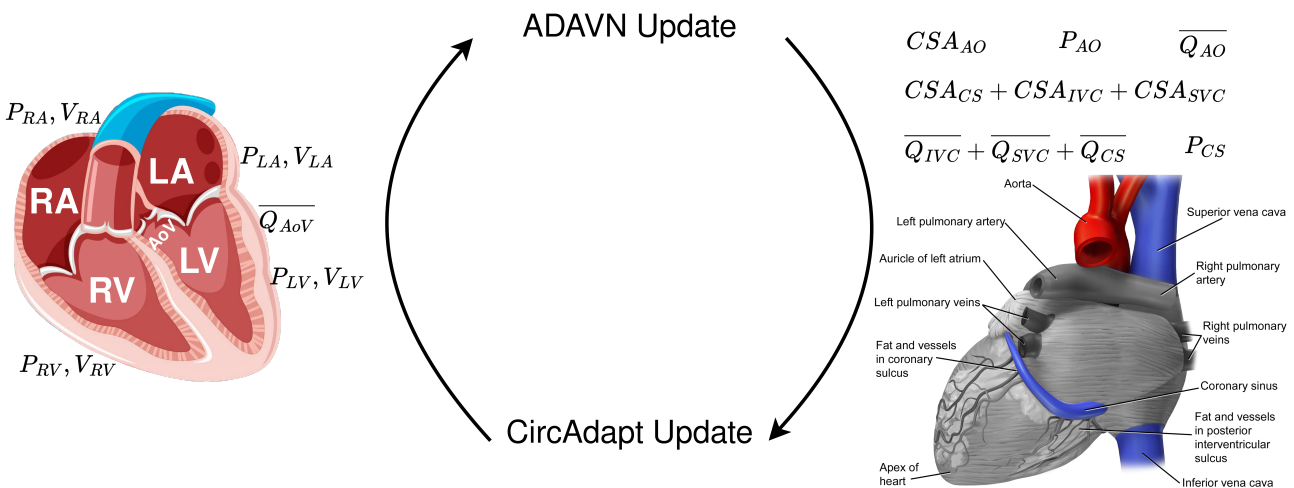


**Figure 4.1:** The diagram shows the coupling between the ADAVN and CircAdapt models. At each time step, CircAdapt provides to the ADAVN the time-averaged flow over a time interval through the aortic valve (AoV) and the pressures and volumes in the four cardiac chambers: right atrium (RA), right ventricle (RV), left atrium (LA), left ventricle (LV). After the update of its systemic circulation and coronary circulation models, ADAVN returns pressure, time-averaged flow over a time interval, and cross-sectional areas of aorta (AO), coronary sinus (CS), inferior vena cava (IVC) and superior vena cava (SVC) to CircAdapt, which then updates the other connected elements. Images adapted from: [2] and Freepik.

## 2.5 Update Sequence

The update of the ADAVN model occurs along with the updates of the other tubes, following the update cycle shown in [Figure 3.2](#). In CircAdapt the update process begins with the cavities, followed by the tubes, then valves and finally the remaining elements. In terms of time steps, once CircAdapt completes the update of all elements at the time step  $t_n$ , it moves

to time step  $t_{n+1}$ , and the update cycle begins again.

This means that in the coupled model, as can be seen in [Figure 4.2](#), the valves are processed after the AdavnTube update, meaning that the ADAVN model at  $t_n$  still uses the time-averaged outflow over a time interval from the aortic valve that has not yet been updated to  $t_n$  and is still at  $t_{n-1}$ . In contrast, the pressure and volume values from the heart chambers are already updated at the current time step  $t_n$ .

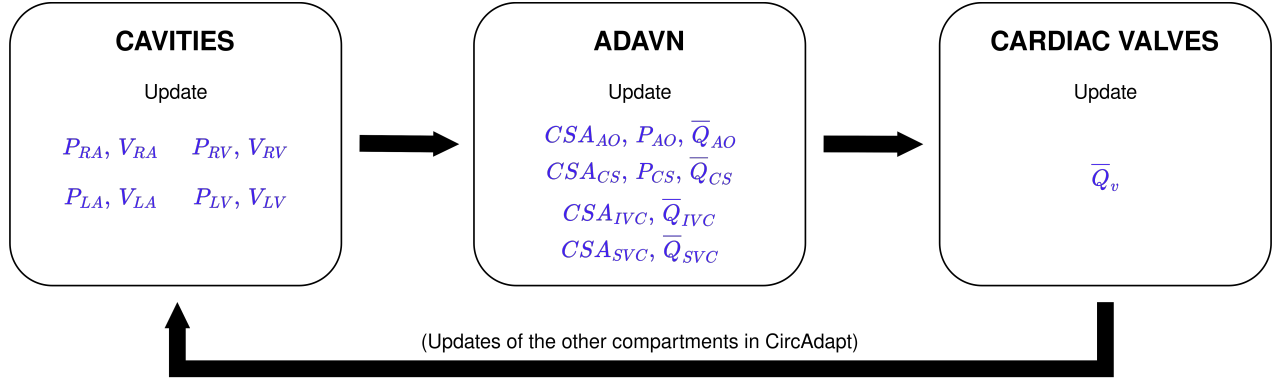


**Figure 4.2:** Diagram showing the update sequence of the coupled model, where the valves are processed after the AdavnTube update. As a result, the ADAVN model at time step  $t_n$  still uses the time-averaged outflow over a time interval from the aortic valve from time step  $t_{n-1}$ , while the pressure and volume values from the heart chambers are already updated to  $t_n$ .

## 2.6 Modification of Coronary Circulation Data Handling for CircAdapt Integration

In order to update the coronary circulation without the ADAVN heart submodel, a modification was made in the `solveTerminalsCoronary()` function so that it no longer reads information from the ADAVN but instead retrieves data from the CircAdapt heart submodel. This function executes the time evolution of coronary terminals, updating boundary conditions for arteries and veins connected to the coronaries based on blood flow data. To implement this, new variables are created within the ADAVN model and updated by the CircAdapt model.

## 3 Numerical Stability

### 3.1 Monolithic vs. Data Exchange Approaches for Coupling

To couple models like in this work, a well-known approach is the monolithic one [1, 3], where a saddle point problem is introduced into the system of equations, requiring both models to be solved simultaneously through a tightly integrated framework. While this method ensures strong coupling between the models, it can significantly increase both computational and implementation complexity [4, 5].

Alternatively, the method used in this work involves a loosely coupled approach, where no additional equations are introduced. Instead, data is exchanged between the models after each time step. In this case, the output of one model serves as input for the other, maintaining a more flexible and computationally efficient framework while preserving the essential dynamics of the coupled system.

### 3.2 Challenges with Segregated Methods in Coupling

When employing a loosely coupled approach, several challenges may arise. In a segregated (or partitioned) approach, where the models exchange information sequentially, rather than solving a unified system of equations, the main problem is ensuring stability and accuracy. One major issue is the potential for numerical instabilities, particularly at the interfaces between models. For instance, as highlighted in [4] and [6], improper handling of boundary conditions can lead to unphysical wave reflections, especially when coupling 0D and 1D models.

Additionally, the segregated method can suffer from convergence problems. Since each model is solved separately and data is exchanged iteratively, the method may require additional computational effort to achieve a stable solution. As discussed in [6], adopting segregated schemes often involves trade-offs between computational efficiency and stability.

### 3.3 Time Stepping Strategy

In our case, we employ the Forward Euler method to solve the CircAdapt model as explained in [Chapter 3, Section 10](#). The Forward Euler method is an explicit time integration method that is known to suffer from stability issues, especially when used with stiff systems or large time steps. To mitigate these potential instabilities, we use a small time step size of  $0.1\text{ ms}$  for CircAdapt, ensuring that the explicit nature of the method does not introduce numerical instabilities that could compromise the accuracy of the simulation. This strategy of using a small time step has proven sufficient to maintain stability in the overall coupled model.



---

# Bibliography

---

- [1] Christoph M. Augustin et al. “A computationally efficient physiologically comprehensive 3D–0D closed-loop model of the heart and circulation”. In: *Computer Methods in Applied Mechanics and Engineering* 386 (Dec. 2021), p. 114092. DOI: [10.1016/j.cma.2021.114092](https://doi.org/10.1016/j.cma.2021.114092).
- [2] Blausen. “Medical Gallery of Blausen Medical 2014”. In: *[[WikiJournal of Medicine—WikiJournal of Medicine]]* 1.2 (Aug. 29, 2014). DOI: [10.15347/WJM/2014.010](https://doi.org/10.15347/WJM/2014.010).
- [3] Federica Caforio et al. “A coupling strategy for a first 3D-1D model of the cardio-vascular system to study the effects of pulse wave propagation on cardiac function”. In: *Computational Mechanics* 70.4 (July 2022), pp. 703–722. DOI: [10.1007/s00466-022-02206-6](https://doi.org/10.1007/s00466-022-02206-6).
- [4] Luca Formaggia et al. “Multiscale modelling of the circulatory system: a preliminary analysis”. In: *Computing and Visualization in Science* 2.2–3 (Dec. 1999), pp. 75–83. DOI: [10.1007/s007910050030](https://doi.org/10.1007/s007910050030).
- [5] Alfio Quarteroni et al. “Integrated Heart—Coupling multiscale and multi-physics models for the simulation of the cardiac function”. In: *Computer Methods in Applied Mechanics and Engineering* 314 (Feb. 2017), pp. 345–407. DOI: [10.1016/j.cma.2016.05.031](https://doi.org/10.1016/j.cma.2016.05.031).
- [6] F. Regazzoni et al. “A cardiac electromechanical model coupled with a lumped-parameter model for closed-loop blood circulation”. In: *Journal of Computational Physics* 457 (May 2022), p. 111083. DOI: [10.1016/j.jcp.2022.111083](https://doi.org/10.1016/j.jcp.2022.111083).



## Results and Discussion

---

## Contents of the chapter

---

1	Performance and Computational Speed of the Coupled Model . . . . .	99
2	Convergence Analysis . . . . .	99
2.1	Comparison of Simulations Results with Different Time Resolutions . . . . .	100
3	Convergence of the Curves . . . . .	101
3.1	Convergence of the Pressures in the Ventricles . . . . .	101
3.2	Calculation of the Norms . . . . .	102
3.3	Convergence of the Total Mass . . . . .	103
3.4	Convergence of Various Compartments in the Coupled Model . . . . .	103
4	Haemodynamic Variables . . . . .	104
4.1	Computation and Meaning of Haemodynamic Variables . . . . .	104
4.2	Comparison of Haemodynamic Variables with Literature Values . . . . .	107
5	Curve Plots of Simulation Data . . . . .	107
5.1	Pressure, Volume and PV Loop of the Ventricles . . . . .	107
5.2	Pressure and Volume in the Atria . . . . .	109
5.3	Mass Conservation . . . . .	110
5.4	Pressure and Flow in the Ascending and Abdominal Aorta . . . . .	111
5.5	Pressure and Flow in the Superior Vena Cava . . . . .	112
5.6	Pressure and Flow in the Right Common Carotid Artery (RCCA) and Right Femoral Vein . . . . .	113
5.7	Pressure and Flow in the Left Internal Jugular Vein (LIJV) . . . . .	114

---

## 1 Performance and Computational Speed of the Coupled Model

The computational cost of the coupled ADAVN and CircAdapt model is comparable to the standalone ADAVN model. CircAdapt, being a 0D cardiovascular model, is extremely fast. When run independently, CircAdapt can simulate tens of cardiac cycles in just a few seconds on a standard office PC, making it highly efficient. However, in the coupled model, the component that requires the most computational time is ADAVN, which is significantly more complex than CircAdapt. This is because ADAVN involves solving nonlinear partial differential equations (PDEs), making it computationally slower. Consequently, the overall performance of the coupled model is largely determined by the ADAVN simulation speed.

On average, running a simulation of 50 cardiac cycles with the coupled model takes approximately 3 hours on a PC equipped with a 13th Gen Intel Core i7-13700H × 20, utilizing multiprocessing. This time frame reflects the additional complexity introduced by ADAVN compared to CircAdapt's standalone performance.

## 2 Convergence Analysis

In the numerical simulations carried out, an important observation is that the results remain unchanged when the time step  $\text{dt}$  is reduced beyond 0.0001s. This behavior shows that the solutions are mesh-independent with respect to the time step. Here, 'time step' refers to the input time step, which coincides with the one used in the CircAdapt model but serves as the maximum time step in the LTS method used by the ADAVN model. Additionally, in the ADAVN model, the spatial discretization proposed in [7] was used, where it is shown that the solution is mesh-independent.

In the following subsection, we present a comparison of curves from the last cycle of a 50-cycle simulation with different time steps, showing no significant differences for  $\text{dt}$  values smaller than 0.0001s. As illustrated in [Figure 5.1](#), [Figure 5.2](#), [Figure 5.4](#), and [Figure 5.3](#), the curves converge and overlap for time steps smaller than 0.0001s, suggesting the numerical stability of the model and indicating that the solutions are mesh-independent with respect to the time step.

## 2.1 Comparison of Simulations Results with Different Time Resolutions

In [Figure 5.1](#), the PV loop in the left ventricle at the final cycle of the simulations is compared across different  $dt$  values. Similarly, [Figure 5.2](#), [Figure 5.3](#), and [Figure 5.4](#) show comparisons of the pressure profiles in the ascending aorta, superior vena cava, and left internal jugular vein, respectively, for simulations with varying  $dt$  values.

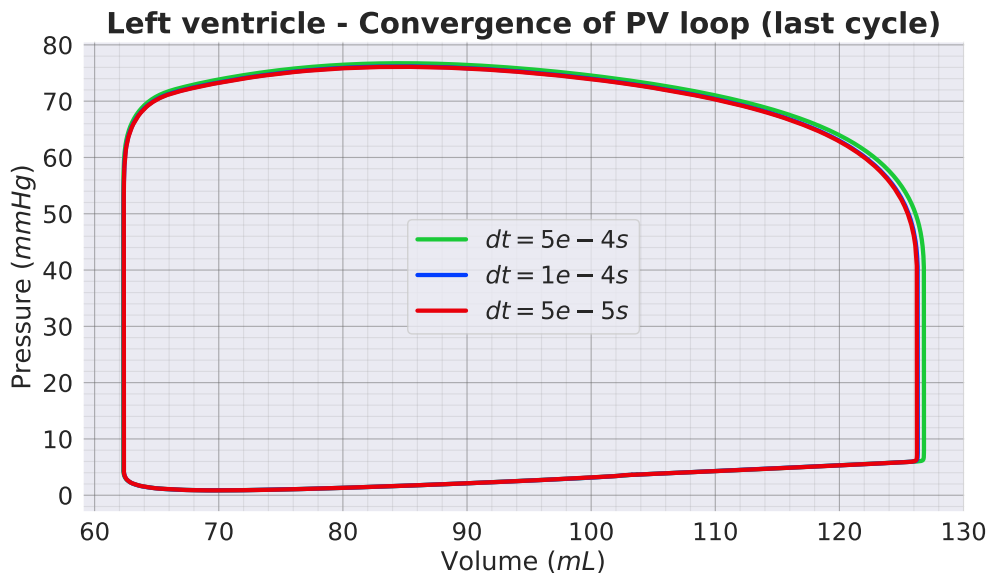


**Figure 5.1:** Convergence of the PV loop in LV for different choices of  $dt$ .

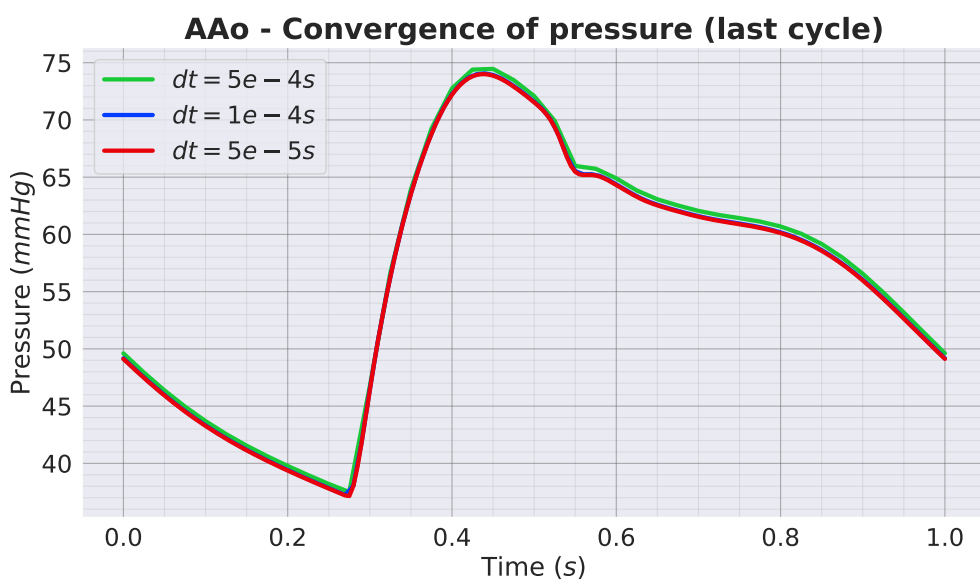


**Figure 5.2:** Convergence of the pressure in the ascending aorta (AAo) in ADAVN for different choices of  $dt$ .

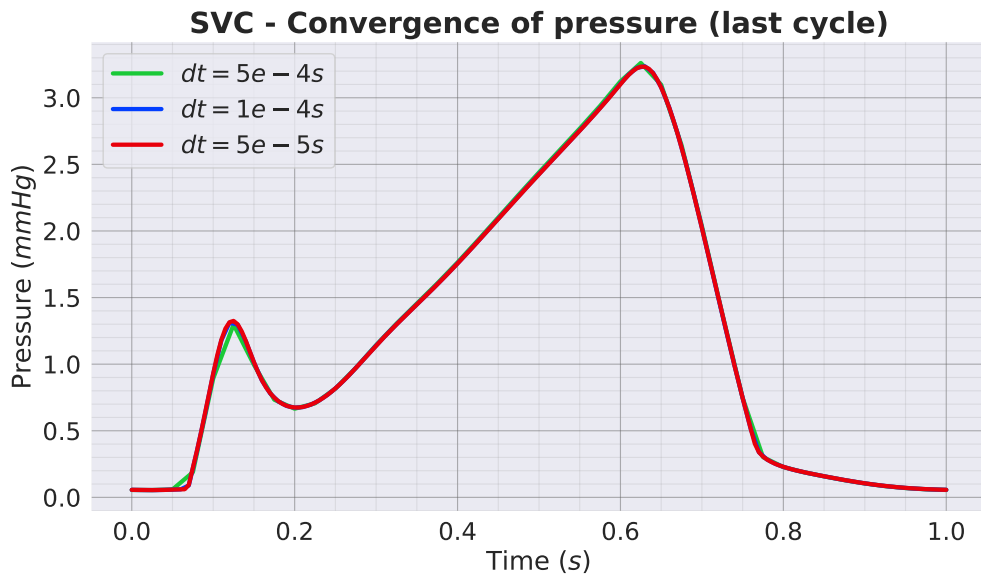


**Figure 5.3:** Convergence of the pressure profile in the superior vena cava (SVC) in ADAVN for different choices of  $dt$ .

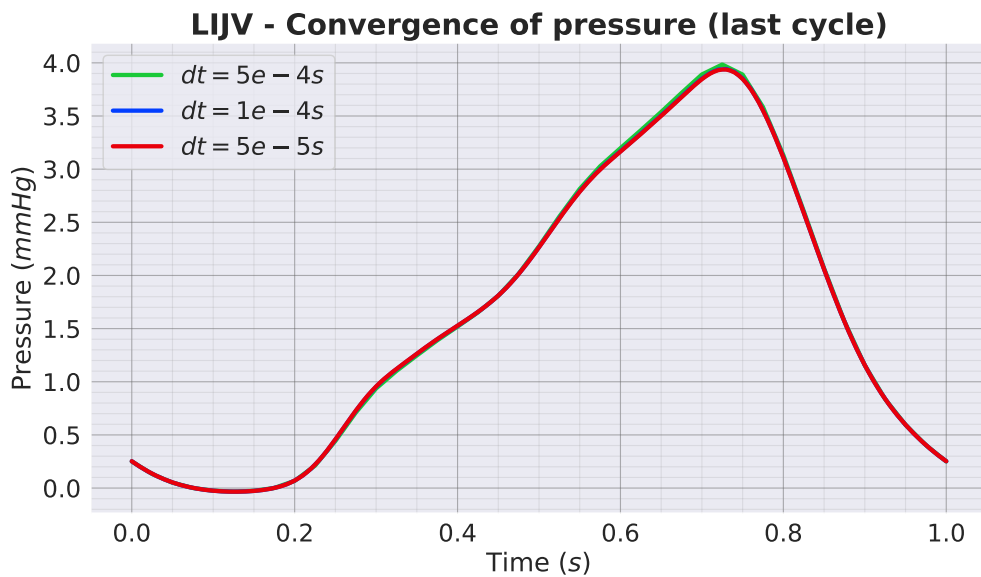


**Figure 5.4:** Convergence of the pressure profile in the left interior jugular vein (LIJV) in ADAVN for different choices of  $dt$ .

### 3 Convergence of the Curves

#### 3.1 Convergence of the Pressures in the Ventriles

In [Figure 5.5](#), the pressure profiles in the ventriles over the last 10 cycles of the simulation are shown, where convergence has already been achieved. While visually verifying the convergence is a positive first step, it is crucial to conduct a more in-depth analysis by studying the norm of the differences between successive cycles. This provides a quantitative measure of how well the

model approaches a steady state. Such an analysis is performed in the following subsections, where the norms are computed to rigorously confirm the model's convergence behavior.

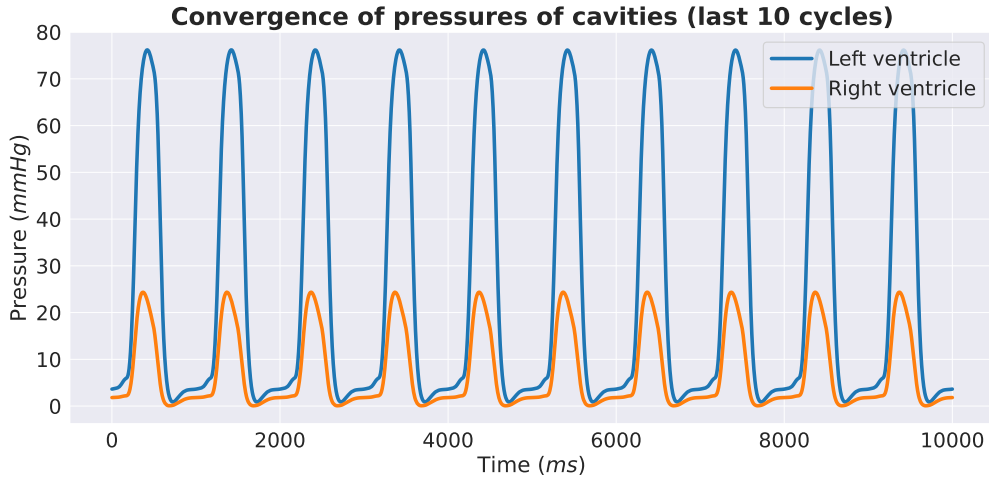


**Figure 5.5:** Pressure in the cardiac chambers over 10 cardiac cycles, demonstrating visual convergence.

### 3.2 Calculation of the Norms

To assess the convergence of pressures, flows and volumes, we compute the norms  $l^1$ ,  $l^2$ , and  $l^\infty$  of the differences between the two sets of values obtained in the last two cycles of the simulation. Let  $T$  be the duration of a cardiac cycle, and let  $f$  be a function defined on  $[0, T]$  that represents the values of a cardiovascular parameter during the last cardiac cycle. Similarly, let  $g$  be a function defined on  $[0, T]$  that represents the values of the same cardiovascular parameter during the second-to-last cardiac cycle. Assume  $N$  is the total number of time steps in  $[0, T]$ , where  $N$  depends on the choice of the time step  $dt$  in our numerical method; we then define  $t_i$  for  $i = 1, \dots, N$  as the points at which the parameter is sampled during a cardiac cycle. We can then define the following norms.

#### $l^1(N)$ norm

The  $l^1$  norm represents the total error over the entire domain, which in this case is the last cardiac cycle, and is calculated as the sum of the absolute differences between the two sets of values:

$$\|f - g\|_{l^1} = \sum_{i=1}^N |f(t_i) - g(t_i)|.$$

#### $l^2(N)$ norm

The  $l^2$  norm captures the root-mean-square error (RMSE) over the entire domain, and is computed as:

$$\|f - g\|_{l^2} = \sqrt{\sum_{i=1}^N (f(t_i) - g(t_i))^2}.$$

**$l^\infty$  norm**

The  $l^\infty$  norm evaluates the maximum error at any time point in the domain. It is computed as the maximum absolute difference between the two sets of values:

$$\|f - g\|_{l^\infty} = \max_{i=1}^N |f(t_i) - g(t_i)|.$$

### 3.3 Convergence of the Total Mass

**Table 5.1** shows the values of the norm of the difference of the total mass in the coupled model in the last two cycles of the simulation. The small values obtained across all norms indicate that the model has achieved convergence in terms of mass conservation. The  $l_\infty$  norm, representing the maximum difference at any point, is only slightly higher than the other norms, suggesting that the model maintains consistency throughout the entire cycle, without significant local deviations. For other considerations about the mass, see [Subsection 5.3](#).

	$\ \cdot\ _{l_1}$	$\ \cdot\ _{l_2}$	$\ \cdot\ _{l_\infty}$
Mass ( $mL$ )	0.034	0.034	0.039

**Table 5.1:** Convergence norms for the total mass in the coupled model.

### 3.4 Convergence of Various Compartments in the Coupled Model

**Table 5.2** shows the value of the norm of the difference of pressure, volume and flow in various compartments of the coupled model.

It is noticeable that the  $l_1$  norms of curves in the CircAdapt elements tend to be higher compared to the  $l_2$  and  $l_\infty$ . This higher value reflects a greater cumulative difference over the entire simulation domain, indicating that while the overall error across the time steps is larger, the local discrepancies (captured by  $l_2$  and  $l_\infty$ ) remain small. This behavior suggests that while the CircAdapt model exhibits good pointwise stability, there are more significant total variations throughout the cardiac cycle. This could be due to the simplified nature of CircAdapt, which might not capture certain dynamics with the same precision as more detailed models like ADAVN. Despite this, the fact that  $l_2$  and  $l_\infty$  norms remain small indicates that the model's local accuracy is sufficient for stable simulations.

The convergence norms for the components in the ADAVN model suggest numerical stability. The  $l_1$ ,  $l_2$ , and  $l_\infty$  norms for flow and pressure are relatively low, particularly for pressure, where values remain minimal.

		$\ \cdot\ _{l_1}$	$\ \cdot\ _{l_2}$	$\ \cdot\ _{l_\infty}$
ADAVN	$P_{AO} \text{ (mmHg)}$	0.094	0.010	0.001
	$P_{CS} \text{ (mmHg)}$	0.018	0.001	0.001
	$P_{IVC} \text{ (mmHg)}$	0.018	0.011	0.010
	$P_{SVC} \text{ (mmHg)}$	0.008	0.001	0.001
	$Q_{AO} \text{ (mL/s)}$	0.192	0.047	0.022
	$Q_{CS} \text{ (mL/s)}$	0.422	0.049	0.008
	$Q_{IVC} \text{ (mL/s)}$	0.569	0.070	0.013
	$Q_{SVC} \text{ (mL/s)}$	0.011	0.002	0.001
CircAdapt	$P_{LA} \text{ (mmHg)}$	0.846	0.029	0.001
	$P_{LV} \text{ (mmHg)}$	2.300	0.048	0.001
	$P_{RA} \text{ (mmHg)}$	0.189	0.014	0.001
	$P_{RV} \text{ (mmHg)}$	0.564	0.024	0.001
	$V_{LA} \text{ (mL)}$	3.550	0.060	0.001
	$V_{LV} \text{ (mL)}$	5.599	0.077	0.002
	$V_{RA} \text{ (mL)}$	1.445	0.038	0.001
	$V_{RV} \text{ (mL)}$	2.881	0.054	0.001
	$Q_{LA} \text{ (mL/s)}$	1.613	0.215	0.007
	$Q_{LV} \text{ (mL/s)}$	1.276	0.278	0.010
	$Q_{RA} \text{ (mL/s)}$	3.603	0.071	0.002
	$Q_{RV} \text{ (mL/s)}$	2.690	0.066	0.003

**Table 5.2:** Convergence norms for pressure, volume, and flow in various cardiovascular compartments in ADAVN and CircAdapt models.

## 4 Haemodynamic Variables

### 4.1 Computation and Meaning of Haemodynamic Variables

#### Mean Arterial Pressure (MAP)

Let  $P_{AAo}$  be the array representing the pressure curve during the last cycle of the simulation, recorded in the first spatial cell of the ascending aorta. The length of  $P_{AAo}$  is  $N$ , and each element  $P_{AAo,i}$  for  $i = 1, \dots, N$  corresponds to the pressure value at the  $i$ -th time point.

The Mean Arterial Pressure (MAP) is then calculated as the arithmetic mean of the values in  $P_{AAo}$  using the formula:

$$\text{MAP} = \frac{1}{N} \sum_{i=1}^N P_{AAo,i}.$$

The mean arterial pressure is a key hemodynamic parameter that represents the average pressure in the arteries during a full cardiac cycle. It provides an indication of the overall perfusion pressure to vital organs and is an important measure of cardiovascular function. MAP is often used clinically to assess the adequacy of blood flow, particularly in critically ill patients, as it reflects both the systolic and diastolic pressures, giving a more stable view of arterial pressure than either of these individual values alone [6].

### Diastolic Blood Pressure (DBP)

The Diastolic Blood Pressure (DBP) is calculated as the minimum value in  $P_{AAo}$  during the last cycle of the simulation:

$$\text{DBP} = \min_{i=1,\dots,N} P_{AAo,i}.$$

The diastolic blood pressure represents the lowest pressure in the arteries during the relaxation phase of the cardiac cycle, when the heart refills with blood. Clinically, elevated DBP can indicate increased vascular resistance, while low DBP may suggest poor arterial tone or blood volume [6].

### Systolic Blood Pressure (SBP)

The Systolic Blood Pressure (SBP) is calculated as the maximum value in  $P_{AAo}$  during the last cycle of the simulation:

$$\text{SBP} = \max_{i=1,\dots,N} P_{AAo,i}.$$

The systolic blood pressure represents the highest pressure in the arteries during the contraction phase of the heart, known as systole, when blood is being ejected from the heart into the aorta. SBP is an important indicator of the force exerted by the heart to pump blood and reflects the overall efficiency of cardiac function. Clinically, elevated SBP can signal conditions such as hypertension or increased workload on the heart, while lower SBP may indicate weakened heart function or decreased blood volume [6].

### Pulse Pressure in the Ascending Aorta ( $\text{PP}_A$ )

The Pulse Pressure in the Ascending Aorta ( $\text{PP}_A$ ) is calculated as the systolic blood pressure minus the diastolic blood pressure:

$$\text{PP}_A = \text{SBP} - \text{DBP}.$$

The pulse pressure in the ascending aorta represents the difference between systolic and diastolic blood pressure, providing an estimate of the force that the heart generates with each contraction. It reflects the elasticity of the arterial walls and the overall health of the cardiovascular system. A higher PP can indicate stiffening of the arteries or increased stroke volume, while a lower PP may suggest reduced cardiac output or compromised arterial elasticity [6].

### Mean Pulmonary Arterial Pressure (MPAP)

Let  $P_{AP}$  be the array representing the pressure curve during the last cycle of the simulation, recorded in the arteria pulmonaris. The length of  $P_{AP}$  is  $N$ , and each element  $P_{AP,i}$  for  $i = 1, \dots, N$  corresponds to the pressure value at the  $i$ -th time point.

The Mean Pulmonary Arterial Pressure (MPAP) is then calculated as the arithmetic mean of the values in  $P_{AP}$  using the formula:

$$\text{MPAP} = \frac{1}{N} \sum_{i=1}^N P_{AP,i}.$$

The mean pulmonary arterial pressure is an important hemodynamic parameter that reflects the average pressure in the pulmonary artery during a full cardiac cycle. MPAP provides insight into the function of the right side of the heart and the resistance of the pulmonary vasculature. It is a key indicator in diagnosing and monitoring pulmonary hypertension and assessing the overall pulmonary circulation's health. Elevated MPAP can indicate increased pulmonary vascular resistance, which may lead to right heart strain or failure [5].

### Central Venous Pressure (CVP)

Let  $P_{SVC}$  be the array representing the pressure curve during the last cycle of the simulation, recorded in the last spatial cell of the superior vena cava. The length of  $P_{SVC}$  is  $N$ , and each element  $P_{SVC,i}$  for  $i = 1, \dots, N$  corresponds to the pressure value at the  $i$ -th time point.

The Central Venous Pressure (CVP) is then calculated as the arithmetic mean of the values in  $P_{SVC}$  using the formula:

$$\text{CVP} = \frac{1}{N} \sum_{i=1}^N P_{SVC,i}.$$

The central venous pressure is a critical hemodynamic parameter that represents the average pressure in the superior vena cava, reflecting the pressure in the right atrium of the heart. Elevated CVP may indicate fluid overload, right heart failure, or increased venous pressure, while low CVP can suggest hypovolemia or reduced venous return [8].

### Left Ventricle Stroke Volume (LVSV)

Let  $V_{LV}$  be the array representing the volume curve during the last cycle of the simulation, recorded in the left ventricle. The length of  $V_{LV}$  is  $N$ , and each element  $V_{LV,i}$  for  $i = 1, \dots, N$  corresponds to the volume value at the  $i$ -th time point.

The Left Ventricle Stroke Volume (LVSV) is calculated as the maximum value in  $V_{LV}$  minus the minimum value in  $V_{LV}$ :

$$\text{LVSV} = \max_{i=1,\dots,N} V_{LV,i} - \min_{i=1,\dots,N} V_{LV,i}.$$

The left ventricle stroke volume represents the amount of blood ejected by the left ventricle during a single cardiac cycle. It is calculated as the difference between the maximum and minimum volumes in the left ventricle, corresponding to the volume of blood present at the end of diastole (end-diastolic volume) and the end of systole (end-systolic volume). LVSV is a key parameter in assessing cardiac performance, as it reflects the efficiency of the heart in pumping blood [8].

### Left Ventricle Ejection Fraction (LVEF)

The Left Ventricle Ejection Fraction (LVEF) is calculated as the LVSV divided by the maximum value in  $V_{LV}$  and then multiplied by 100 to obtain the percentage:

$$\text{LVEF} = \frac{\text{LVSV}}{\max_{i=1,\dots,N} V_{LV,i}} \cdot 100.$$

The left ventricle ejection fraction is a key measure of how effectively the left ventricle pumps blood with each heartbeat. A higher LVEF indicates a more efficient heart function, while a lower LVEF can signal weakened heart muscle or heart failure. Clinically, LVEF is widely used to assess the pumping capability of the heart and to monitor conditions such as heart failure or cardiomyopathy [4].

## 4.2 Comparison of Haemodynamic Variables with Literature Values

Parameter	Units	Model	Reference value	Reference
MAP	mmHg	59.28	88(8)	[6]
DBP	mmHg	38.24	73(8)	[6]
SBP	mmHg	76.06	123(10)	[6]
MPAP	mmHg	13.55	14(3)	[5]
CVP	mmHg	1.32	(0-5)	[8]
PP <sub>A</sub>	mmHg	35.82	30(6)	[6]
LHSV	mL	63.97	(40-120)	[8]
LVEF	%	52.65	(52-72)	[4]

**Table 5.3:** Main model-predicted cardiac and haemodynamic variables and reference values reported in the literature.

**Table 5.3** reports the values of typical cardiovascular indexes computed with the coupled model. Also, reference values extracted from the literature have been included. From the table is possible to study the performance of the model in terms of its capacity to reproduce a normal haemodynamic state.

The model is not able to reproduce all the indices listed in the table. In particular, the model generates a pressure in the ascending aorta that is too low, as can be seen from the MAP, DBP, and SBP values. However, the agreement found with PP<sub>A</sub> suggests that, although the pressure in the ascending aorta is too low, the difference between the systolic and diastolic pressure falls within the range reported in the literature.

The model performs better in the venous and pulmonary sections, where the CVP and MPAP indices align with values reported in the literature.

Additionally, the values in the left ventricle, such as LHSV and LVEF, are consistent with those found in the literature.

It appears that the model tends to operate with overall lower pressures than expected. This would explain why the venous and pulmonary pressures, such as CVP and MPAP, fall within acceptable ranges, while the arterial pressures, including MAP, DBP, and SBP, deviate from the expected values.

## 5 Curve Plots of Simulation Data

In this section we present the results obtained from 50 cycles of the coupled model simulation.

### 5.1 Pressure, Volume and PV Loop of the Ventricle

**Figure 5.6** shows the pressure and volume in the left ventricle in CircAdapt during the final cycle of the simulation, while **Figure 5.7** presents the same for the right ventricle. Similarly, **Figure 5.8** displays the pressure-volume loop in the left ventricle, and **Figure 5.9** shows the pressure-volume loop in the right ventricle, both during the final cycle of the simulation.

The pressure in the left ventricle is lower than expected, though the overall trend aligns well with physiological behavior. The volume curve is generally accurate, except during the phase corresponding to isovolumetric relaxation, where it remains constant at around 60 mL for too long. In reality, the volume should rise immediately during the filling phase. Despite this, the pressure-volume (PV) loop of the left ventricle matches the expected shape, although higher pressures would typically be observed in a physiological setting [2].

A remark is that the pressure and volume curves over time in the left ventricle obtained from the standalone CircAdapt simulations at the last cycle of 50 simulations are nearly identical in shape but reach more physiological values. In particular, in the standalone version, the left ventricle pressure reaches 120 mmHg, and the volume reaches 150 mL. Regarding the right ventricle, the curves are identical within the ranges achieved.

As shown in [Figure 5.7](#), the right ventricle exhibits lower pressures than expected, though the overall trend remains accurate. The pressure-volume (PV) loop in [Figure 5.9](#) also aligns with the expected behavior, capturing the key dynamics of ventricular filling and ejection. Despite the lower pressures in both ventricles, the model effectively simulates overall cardiac function, offering valuable insights into ventricular behavior [8].

Similarly to what was observed with pressures and volumes, the PV loop of the left ventricle in the last cycle of a simulation of 50 cycles with the standalone CircAdapt model is qualitatively identical but reaches higher pressures and volumes. The PV loop of the right ventricle is also qualitatively identical but reaches slightly higher pressures and slightly higher volumes.

The fact that the coupled model generates qualitatively similar results to those produced by the standalone CircAdapt model can be seen as an indication of the proper information transfer between the models, and thus the correct functioning of the coupling implementation. However, the observation that the pressures in the left ventricle are lower suggests that further work is needed to improve the parameterization of the coupled model.

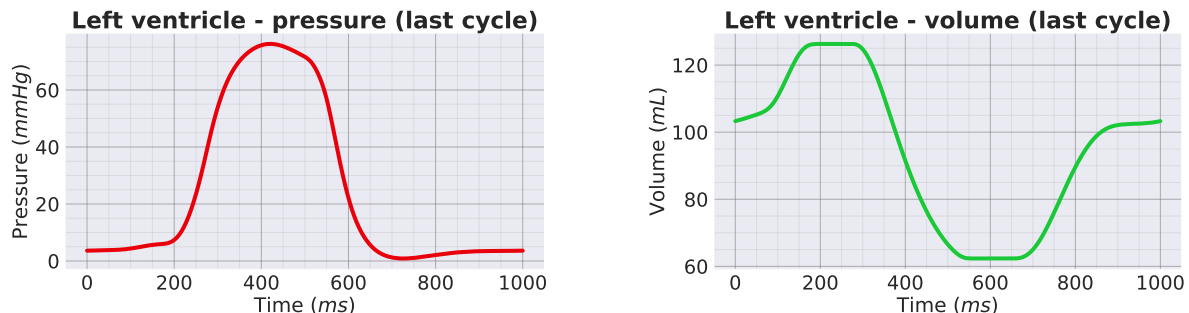


**Figure 5.6:** Pressure and volume in the left ventricle in CircAdapt during the last cycle of the simulation.

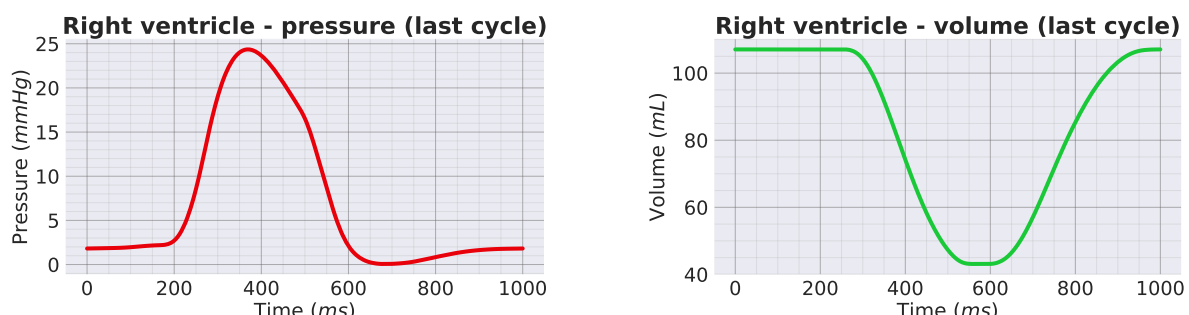


**Figure 5.7:** Pressure and volume in the right ventricle in CircAdapt during the last cycle of the simulation.

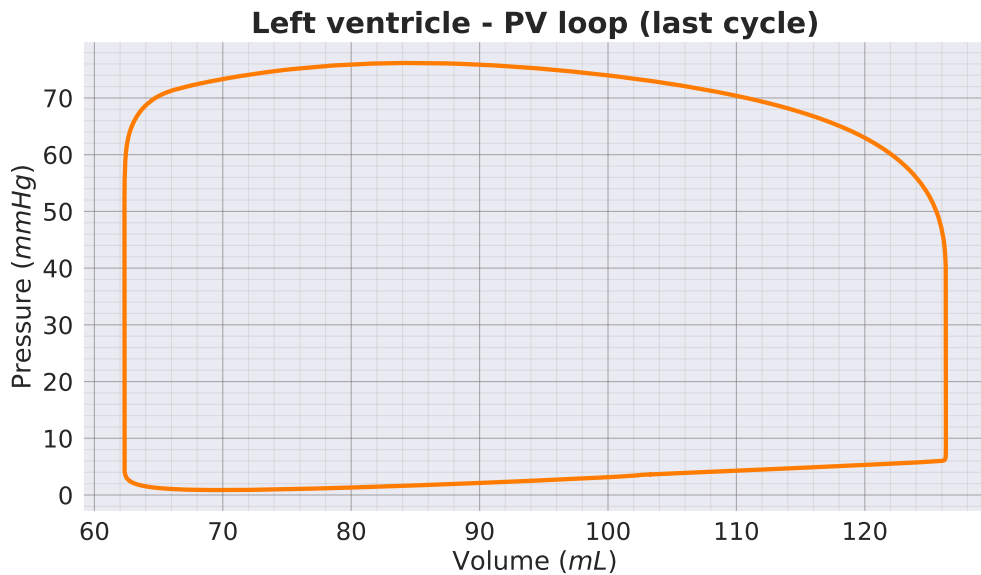


**Figure 5.8:** Pressure-volume loop in the left ventricle in CircAdapt during the last cycle of the simulations.

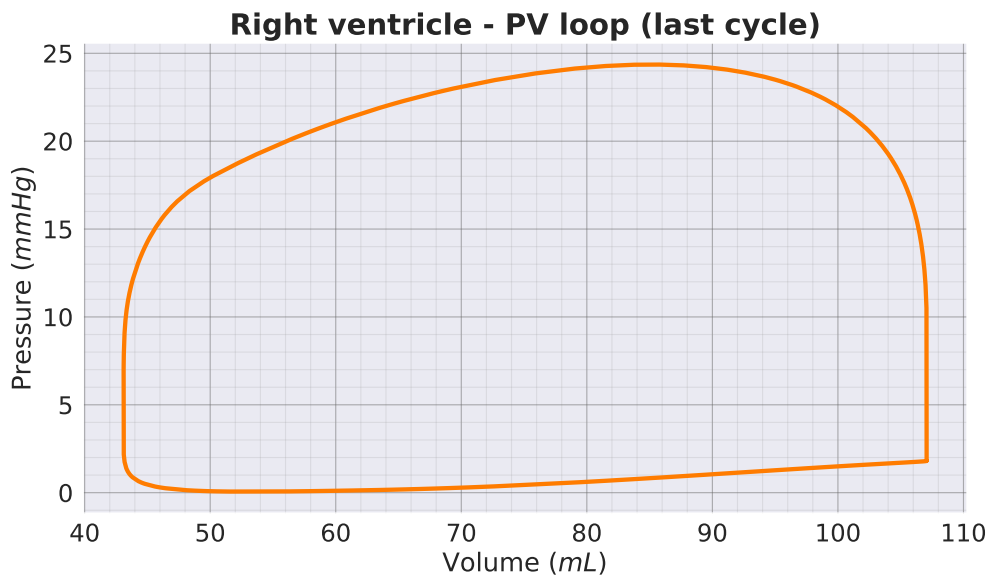


**Figure 5.9:** Pressure-volume loop in the right ventricle in CircAdapt during the last cycle of the simulations.

## 5.2 Pressure and Volume in the Atria

[Figure 5.10](#) shows the pressure and volume in the left atrium in CircAdapt during the final cycle of the simulation, while [Figure 5.11](#) presents the corresponding pressure and volume in the right atrium for the same cycle.

The pressure profiles of the left and right atria generally follow physiological trends, but notable discrepancies exist when compared to real data. For instance, the pressure remains lower than expected, particularly during atrial contraction, indicating a possible underestimation of atrial performance. The rise in pressure during atrial contraction is smoother than it should be, lacking the sharp increase typically observed in physiological conditions. These issues suggest

that while the model captures qualitative trends, it fails to accurately reproduce the quantitative details critical for understanding true atrial function. [8].

The coupled model generates qualitatively identical curves for the left atrium compared to the standalone CircAdapt model. Considering the pressure and volume curves in the left atrium during the last cycle of a 50-cycle simulation of the standalone CircAdapt model, the resulting curves are identical but slightly shifted upward, reaching  $12.5\text{ mmHg}$  and  $70\text{ mL}$ . In contrast, for the right atrium, the pressure curve shows two peaks, with the second peak being consistent with the values obtained from the standalone model. However, the first peak is significantly lower, reaching less than  $2\text{ mmHg}$ , while in the standalone model it exceeds  $6\text{ mmHg}$ . This difference is also evident in the volume curve, where the second peak aligns with the standalone model, but the first peak is completely absent.

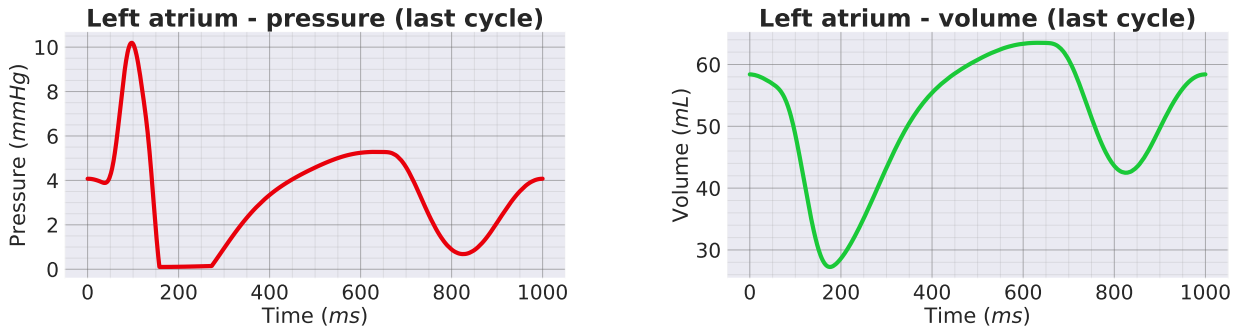


**Figure 5.10:** Pressure and volume in the left atrium in CircAdapt during the last cycle of the simulation.

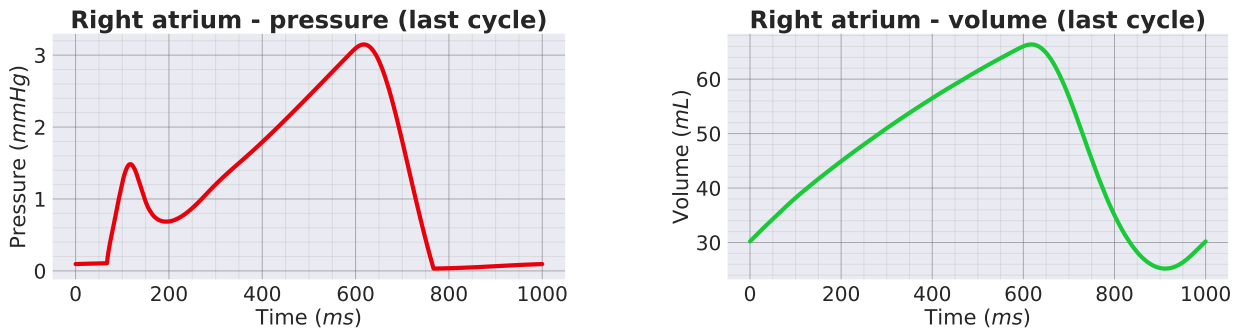


**Figure 5.11:** Pressure and volume in the right atrium in CircAdapt during the last cycle of the simulation.

### 5.3 Mass Conservation

**Figure 5.12** illustrates the mass conservation in CircAdapt during the final cycle of the simulation.

The total mass is not perfectly conserved, as the green curve does not form a perfectly straight line. However, the model produces a periodic curve that converges as the cardiac cycles progress. A peak occurs around  $700\text{ms}$ , showing a  $+16\text{mL}$  difference compared to the value at the beginning and end of the cardiac cycle (which coincide, given the periodic nature). This is problematic, as a closed model should maintain constant mass. Nevertheless, since the curve is periodic, it is suspected that this discrepancy arises from how the mass is being calculated, potentially due to an unmonitored compartment where these extra milliliters are being distributed.

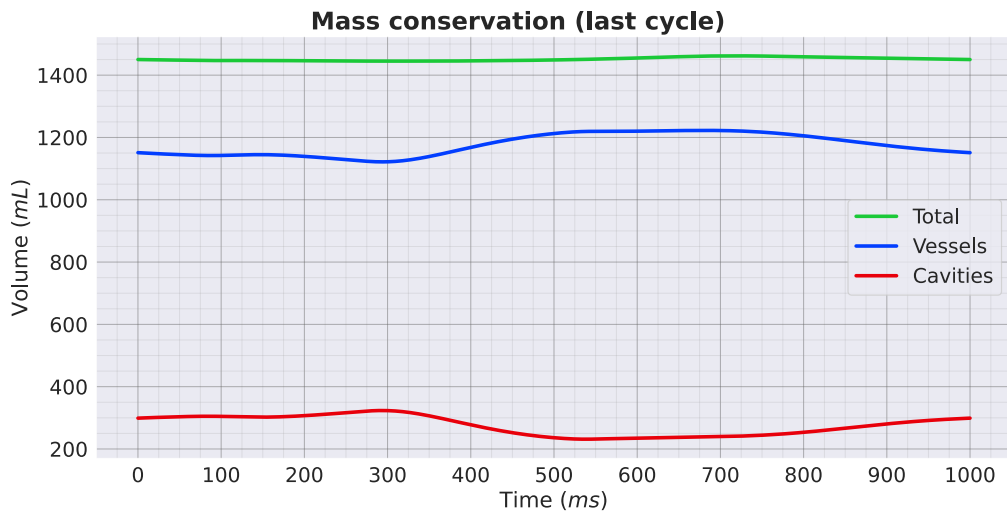


**Figure 5.12:** Mass conservation in CircAdapt during the last cycle of the simulations.

#### 5.4 Pressure and Flow in the Ascending and Abdominal Aorta

**Figure 5.13** shows the pressure and flow in the ascending aorta in ADAVN during the final cycle of the simulation, while **Figure 5.14** presents the corresponding pressure and flow in the abdominal aorta for the same cycle.

The pressure and flow profiles for the ascending aorta and abdominal aorta display general trends that align with expected physiological patterns, featuring pulsatile pressure waveforms associated with cardiac output. Notably, the ascending aorta exhibits a dicrotic notch, which indicates the brief decrease in pressure following aortic valve closure and marks the transition from systole to diastole. While the overall pressure dynamics during the cardiac cycle are represented in both vessels, it is important to note that the peak systolic pressures are consistently lower than those observed in real-world values [8].

As expected, a gradual reduction in flow and increase in pressure is observed as the pulse wave travels from the ascending aorta to the abdominal aorta. This is realistic because, as the pulse wave travels along the arterial tree, pulse pressure amplification occurs, a phenomenon that increases the pressure in the distal sections, such as the abdominal aorta [3]. Additionally, as blood moves through the vessel tree, some of it is diverted into lateral vessels, which decreases the overall flow further down the aorta [1].

Comparing the results with those obtained in [7] for the standalone ADAVN model, we can observe that the qualitative outcomes are similar. The main difference noted is that the pressure is significantly lower here, and there is an absence of retrograde flow in the flow profile of the ascending aorta.

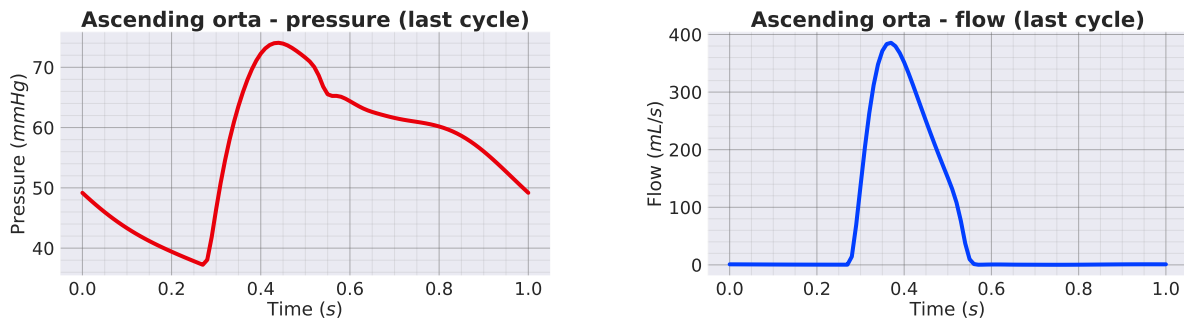


**Figure 5.13:** Pressure and flow in the ascending aorta in ADAVN during the last cycle of the simulation.

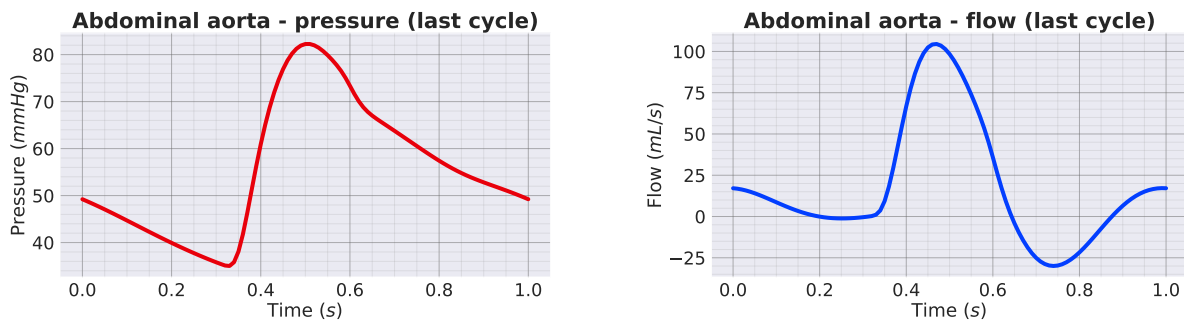


**Figure 5.14:** Pressure and flow in the abdominal aorta in ADAVN during the last cycle of the simulation.

## 5.5 Pressure and Flow in the Superior Vena Cava

**Figure 5.15** illustrates the pressure and flow in the superior vena cava in ADAVN during the final cycle of the simulation.

The results indicate room for improvement. The pressure curve exhibits the expected two peaks, as seen in physiological conditions, but the first peak is significantly lower than the second, whereas they should be approximately equal. Additionally, the flow curve presents only one of the two peaks typically observed in physiological scenarios [7].

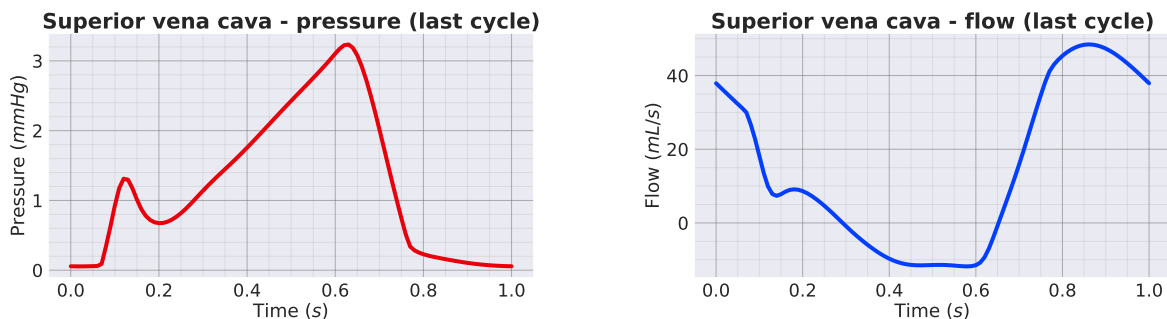


**Figure 5.15:** Pressure and flow in the superior vena cava in ADAVN during the last cycle of the simulation.

## 5.6 Pressure and Flow in the Right Common Carotid Artery (RCCA) and Right Femoral Vein

**Figure 5.16** shows the pressure and flow in the right common carotid artery in ADAVN during the final cycle of the simulation, while **Figure 5.17** presents the corresponding pressure and flow in the right femoral vein for the same cycle.

The flow profiles are qualitatively consistent with expected physiological trends, though the flow values are lower than those observed in real-life scenarios. The flow pattern we obtain is similar to the results presented in [7], but with lower flow values compared to those reported in that study for the simulated curves.

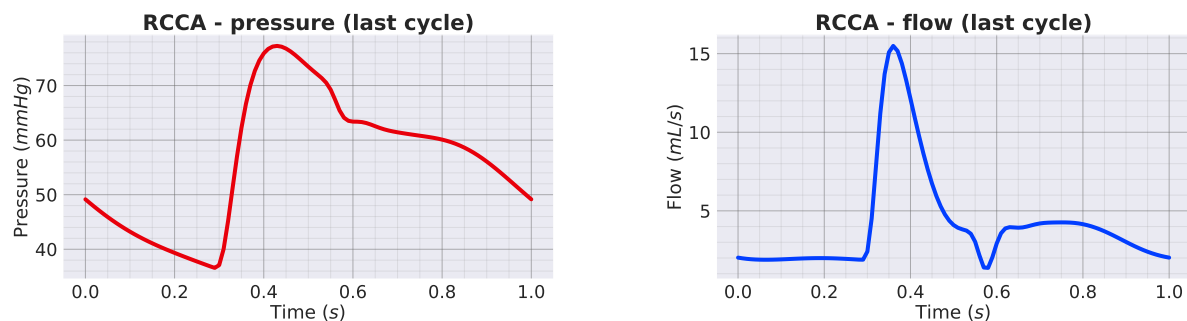


**Figure 5.16:** Pressure and flow in the right common carotid artery (RCCA) in ADAVN during the last cycle of the simulation.

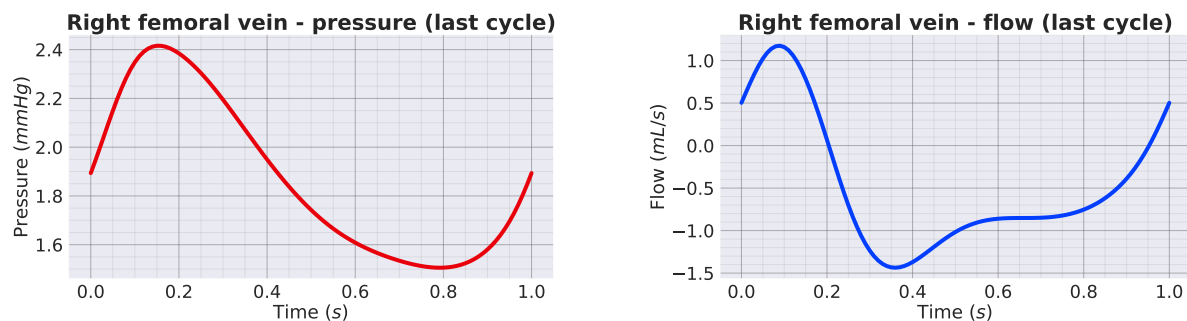


**Figure 5.17:** Pressure and flow in the right femoral vein in ADAVN during the last cycle of the simulation.

## 5.7 Pressure and Flow in the Left Internal Jugular Vein (LIJV)

**Figure 5.18** illustrates the pressure and flow in the left internal jugular vein in ADAVN during the final cycle of the simulation.

The results indicate room for improvement. The flow is lower than physiological values, and the first peak, which would be expected in real-life conditions, is absent [7].

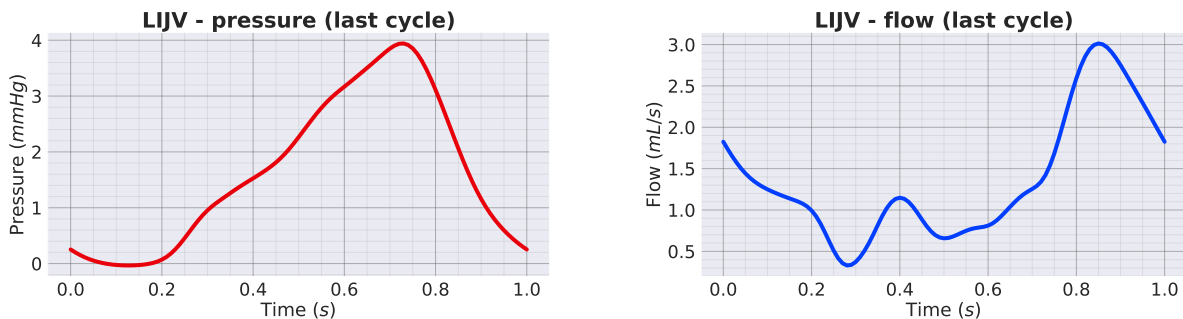


**Figure 5.18:** Pressure and flow in the left internal jugular vein (LIJV) in ADAVN during the last cycle of the simulation.

---

# Bibliography

---

- [1] M. J. Curtis. “**The Heart and Cardiovascular System**”. In: *Cardiovascular Research* 26.7 (July 1992), 720b–720b. DOI: [10.1093/cvr/26.7.720b](https://doi.org/10.1093/cvr/26.7.720b).
- [2] Arthur C. Guyton et al. “**Textbook of Medical Physiology**”. ISBN: [978-0-7216-0240-0](https://doi.org/978-0-7216-0240-0). Elsevier Saunders, 2006. 1160 pp.
- [3] Junichiro Hashimoto et al. “**Pulse Pressure Amplification, Arterial Stiffness, and Peripheral Wave Reflection Determine Pulsatile Flow Waveform of the Femoral Artery**”. In: *Hypertension* 56.5 (2010), pp. 926–933. DOI: [10.1161/HYPERTENSIONAHA.110.159368](https://doi.org/10.1161/HYPERTENSIONAHA.110.159368).
- [4] Ateet Kosaraju et al. “**Left Ventricular Ejection Fraction**”. Available at: <https://www.ncbi.nlm.nih.gov/books/NBK459131/>. StatPearls Publishing, 2023.
- [5] Edmund M. T. Lau et al. “**Resting pulmonary artery pressure of 21–24 mmHg predicts abnormal exercise haemodynamics**”. In: *European Respiratory Journal* 47.5 (Mar. 2016), pp. 1436–1444. DOI: [10.1183/13993003.01684-2015](https://doi.org/10.1183/13993003.01684-2015).
- [6] Carmel M. McEnery et al. “**Normal Vascular Aging: Differential Effects on Wave Reflection and Aortic Pulse Wave Velocity**”. In: *Journal of the American College of Cardiology* 46.9 (Nov. 2005), pp. 1753–1760. DOI: [10.1016/j.jacc.2005.07.037](https://doi.org/10.1016/j.jacc.2005.07.037).
- [7] Lucas O. Müller et al. “**An anatomically detailed arterial-venous network model. Cerebral and coronary circulation**”. In: *Frontiers in Physiology* 14 (June 2023). DOI: [10.3389/fphys.2023.1162391](https://doi.org/10.3389/fphys.2023.1162391).
- [8] David J. Paterson Neil Herring. “**Levick’s Introduction to Cardiovascular Physiology, Sixth Edition**”. Elsevier, 1991. DOI: [10.1016/c2013-0-06523-1](https://doi.org/10.1016/c2013-0-06523-1).



---

## Conclusions

---

## **Contents of the chapter**

---

1	Challenges in the Implementation . . . . .	119
2	Limitations of the Model . . . . .	119
3	Future Steps . . . . .	120

## 1 Challenges in the Implementation

The implementation of the coupled model presented several challenges, particularly in establishing effective communication between the two systems. Resolving compatibility issues was essential to ensure that data could be exchanged efficiently and that the models were synchronized to work seamlessly together.

A major challenge was the need to modify each model individually, especially the ADAVN model. Due to its complexity and extensive C++ codebase, this task required not only advanced programming skills but also a deep understanding of the model itself. One particularly complex aspect of this process was the removal of the heart from the ADAVN model, which was necessary for integration with CircAdapt. This involved not only removing all references to the original ADAVN heart but also integrating the new heart model so that the blood flow, pressure, and volume calculations were transferred correctly. Every reference to the heart in the ADAVN model, from maintaining flow dynamics to managing chamber pressures, had to be systematically replaced or reconfigured.

Modifying the CircAdapt model posed a significant challenge, particularly due to the integration of the ADAVN model. The primary challenge was restructuring the vascular network, transforming the systemic circulation from a configuration of two tubes connected by a resistance into a single tube, which was replaced by the ADAVN model. This restructuring required extensive modifications to the entire network of connections between the model's elements. The systemic circulation had to be redefined as a new element, replacing the previous two tubes and the resistance. This change required not only reconfiguring the circulation pathways but also adjusting how information was exchanged within CircAdapt.

The communication between ADAVN and CircAdapt was also challenging. It was first established through the newly created systemic circulation class in CircAdapt, specifically designed to interface with ADAVN. This class acted as a bridge, receiving and processing the outputs from the ADAVN model. Once the outputs were handled by the systemic circulation class, the relevant information was propagated to other elements within CircAdapt, ensuring seamless data flow across the entire system. The challenge lay in ensuring that this exchange of information was both efficient and accurate, allowing ADAVN to integrate smoothly into CircAdapt without disrupting the overall cardiovascular dynamics.

## 2 Limitations of the Model

The coupled model presented in this study combines two established models, CircAdapt (0D) and ADAVN (1D), to simulate cardiovascular dynamics in a closed-loop system. While this integration has demonstrated promising results, several limitations should be acknowledged.

Firstly, each individual model carries inherent limitations. CircAdapt employs a simplified representation of cardiac mechanics, which, although efficient for simulating pressure-volume relationships, sacrifices certain physiological details. More details can be found in [Chapter 3](#). Another limitation lies in the numerical methods employed. Although CircAdapt uses the forward Euler method, the model achieved stable results. This suggests that further refinement in the choice of numerical methods may not be necessary for basic simulations. However, the long-term stability and accuracy of the model under more complex conditions, such as pathological scenarios, remain untested.

Furthermore, the current version of the model has not undergone a precise comparison with physiological data from real patients. Such a comparison would require a thorough parametrization to align the model's outputs with measured clinical data. As a result, the model's ability

to produce results that can be directly compared to patient-specific data, or its potential to predict cardiovascular pathologies and therapeutic outcomes, has not yet been tested.

### 3 Future Steps

As observed in [Chapter 5](#), while the information transfer between the two models appears to function, the results obtained could be improved. This is especially true for the arterial pressures, which are notably low. Additionally, it seems that the connection between the venous system and the right atrium needs enhancement, as indicated by the unusual trends in the curves for the right atrium and the vena cava. However, we can note that the trends in the curves for the ventricles are qualitatively acceptable, although there is a need to increase the pressure, particularly in the left ventricle. Therefore, it is essential to work on better parameterization of the model to achieve quantitatively improved results that more closely resemble physiological values. The ultimate goal is to validate the model using values taken from the literature.

Once the model has been validated, it will be used to simulate various pathological conditions, with a specific interest in those affecting the venous system. Examples of future simulations include scenarios such as hypertension, tricuspid valve regurgitation (by increasing tricuspid valve leakage), and congestive heart failure (by reducing sarcomere contractility). These conditions will help to investigate how pathologies influence venous pulse wave propagation, which is a core feature of the ADAVN model.

Another improvement to the model would be to enable the use of the Runge-Kutta-Fehlberg 45 (RKF45) method. While this numerical method is already implemented in the CircAdapt model, its coupling with ADAVN has rendered the method unusable and need to be adapted. Restoring compatibility with RKF45 would enhance the model's accuracy and computational efficiency, allowing for adaptive step size control and better performance across a range of simulations.

In addition, there are plans to transition from the reduced version of the ADAVN model currently in use to the full ADAVN model. This enhancement will provide a more detailed representation of the arterial system, offering a more comprehensive understanding of arterial dynamics.

The long-term goal of this project is to explore cardiac pathologies and their impact on the venous system using an *in silico* model, providing a non-invasive alternative to traditional diagnostic methods.

---

## Appendix

---

## Contents of the chapter

---

1	Detailed Description of Vascular Connectivity in the ADAVN Model . . . . .	123
2	Cardiovascular Adaptation Mechanisms in CircAdapt . . . . .	136
2.1	Cardiovascular Adaptation in the Human Heart . . . . .	136
2.2	Example of Adaptation: Raise in Arterial Pressure . . . . .	137
2.3	Adaptation Rules in CircAdapt . . . . .	137
2.4	CircAdapt Adaptation in Detail: Vessel Adaptation . . . . .	140

---

## 1 Detailed Description of Vascular Connectivity in the ADAVN Model

### Brain Vessels: Left Anterior Cerebral Artery

The following is a list of terminal veins connected to the left anterior cerebral artery, as depicted in [Figure 7.1](#):

- ▷ Inferior Sagittal Sinus
- ▷ Superior Sagittal Sinus
- ▷ Internal Cerebral Vein
- ▷ Central Superficial Medial Superior Cerebral Vein
- ▷ Occipital Superficial Medial Superior Cerebral Vein
- ▷ Parietal Superficial Medial Superior Cerebral Vein
- ▷ Precentral Superficial Medial Superior Cerebral Vein
- ▷ Prefrontal Superficial Medial Superior Cerebral Vein

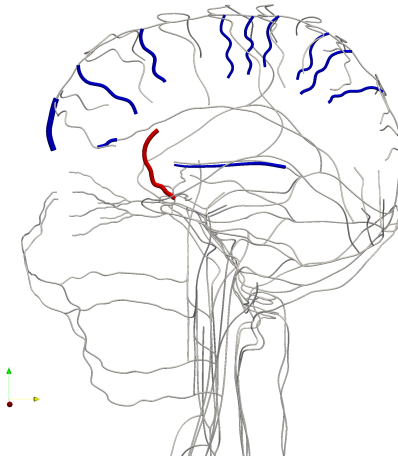


**Figure 7.1:** In red is depicted the left anterior cerebral artery, in blue the terminal veins connected to it [5].

To identify these terminal veins, we followed the vascular path in the ADAVN network originating from the left anterior cerebral artery, tracing the arteries connected to it. All venous terminals that drain these connected arteries were included in this list. To ensure accuracy, we cross-referenced these connections with established brain perfusion zones as documented in the literature. The same criteria is used for all the arteries and veins that follow.

### Brain Vessels: Right Anterior Cerebral Artery

The following is a list of terminal veins connected to the right anterior cerebral artery, as depicted in [Figure 7.2](#):

- ▷ Inferior Sagittal Sinus
- ▷ Superior Sagittal Sinus
- ▷ Internal Cerebral Vein (Right)
- ▷ Central Superficial Medial Superior Cerebral Vein
- ▷ Occipital Superficial Medial Superior Cerebral Vein
- ▷ Parietal Superficial Medial Superior Cerebral Vein
- ▷ Precentral Superficial Medial Superior Cerebral Vein
- ▷ Prefrontal Superficial Medial Superior Cerebral Vein

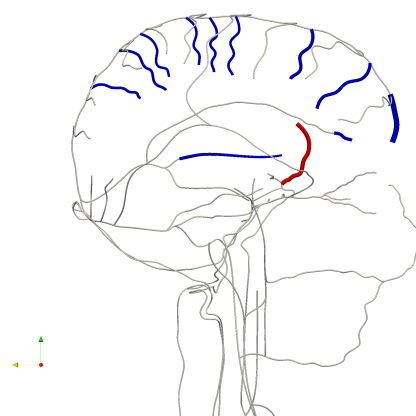


**Figure 7.2:** In red is depicted the right anterior cerebral artery, in blue the terminal veins connected to it [5].

### Brain Vessels: Left Middle Cerebral Artery

The following is a list of terminal veins connected to the left middle cerebral artery, as depicted in [Figure 7.3](#):

- ▷ Left basal vein of Rosenthal
- ▷ Left central superficial lateral superior cerebral vein
- ▷ Left occipital superficial inferior cerebral vein
- ▷ Left occipital superficial lateral superior cerebral vein
- ▷ Left parietal superficial lateral superior cerebral vein
- ▷ Left prefrontal superficial lateral superior cerebral vein

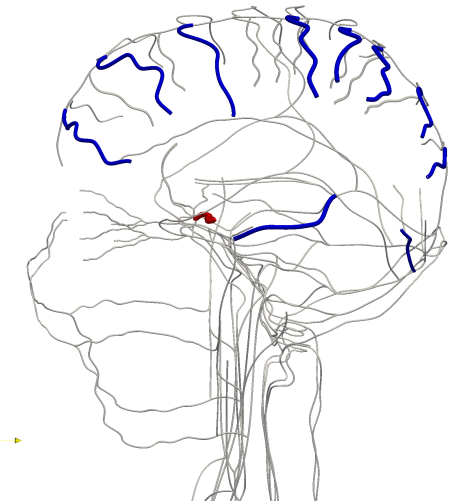


**Figure 7.3:** In red is depicted the left middle cerebral artery, in blue the terminal veins connected to it [5].

### Brain Vessels: Right Middle Cerebral Artery

The following is a list of terminal veins connected to the right middle cerebral artery, as depicted in [Figure 7.4](#):

- ▷ Right basal vein of Rosenthal
- ▷ Right central superficial lateral superior cerebral vein
- ▷ Right occipital superficial inferior cerebral vein
- ▷ Right occipital superficial lateral superior cerebral vein
- ▷ Right parietal superficial lateral superior cerebral vein
- ▷ Right prefrontal superficial lateral superior cerebral vein

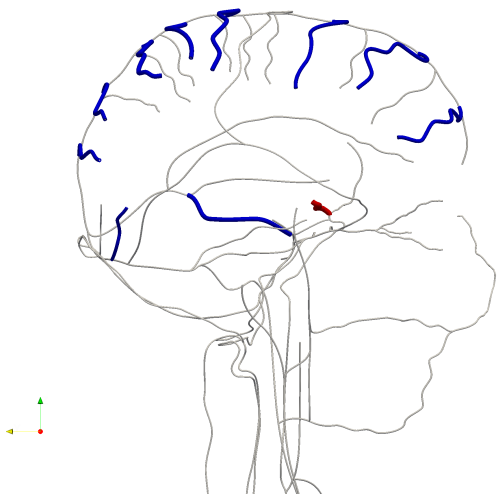


**Figure 7.4:** In red is depicted the right middle cerebral artery, in blue the terminal veins connected to it [5].

### Brain Vessels: Left Posterior Cerebral Postcommunicating Artery

The following is a list of terminal veins connected to the left posterior cerebral postcommunicating artery, as depicted in [Figure 7.5](#):

- ▷ Left basal vein of Rosenthal
- ▷ Left occipital superficial inferior cerebral vein
- ▷ Left occipital superficial lateral superior cerebral vein
- ▷ Left occipital superficial medial superior cerebral vein
- ▷ Central terminal superior sagittal sinus
- ▷ Left temporal superficial inferior cerebral vein

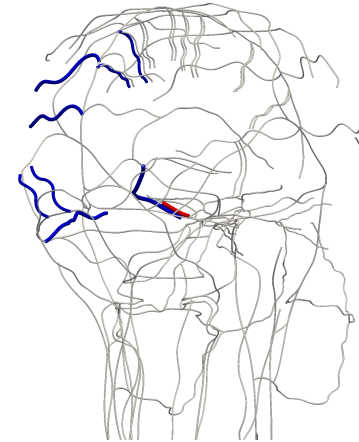


**Figure 7.5:** In red is depicted the left posterior cerebral postcommunicating artery, in blue the terminal veins connected to it [5].

### Brain Vessels: Right Posterior Cerebral Postcommunicating Artery

The following is a list of terminal veins connected to the right posterior cerebral postcommunicating artery, as depicted in [Figure 7.6](#):

- ▷ Right basal vein of Rosenthal
- ▷ Right occipital superficial inferior cerebral vein
- ▷ Right occipital superficial lateral superior cerebral vein
- ▷ Right occipital superficial medial superior cerebral vein
- ▷ Right temporal superficial inferior cerebral vein

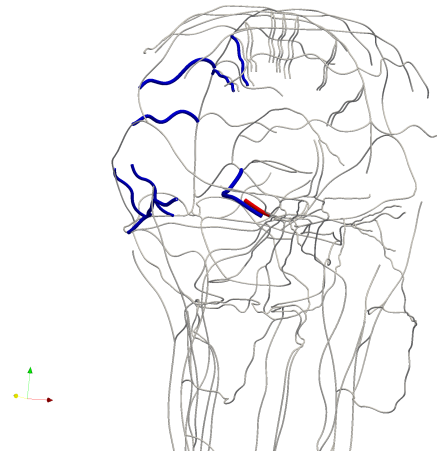


**Figure 7.6:** In red is depicted the right posterior cerebral postcommunicating artery, in blue the terminal veins connected to it [5].

### Neck Vessels: Left External Carotid Artery

The following is a list of terminal veins connected to the left external carotid artery, as depicted in [Figure 7.7](#):

- ▷ Left central retinal vein
- ▷ Left facial vein
- ▷ Left inferior ophthalmic vein
- ▷ Left middle thyroid vein
- ▷ Left posterior auricular vein
- ▷ Left superficial temporal vein
- ▷ Left superior ophthalmic vein
- ▷ Left superior thyroid vein
- ▷ Left inferior thyroid vein

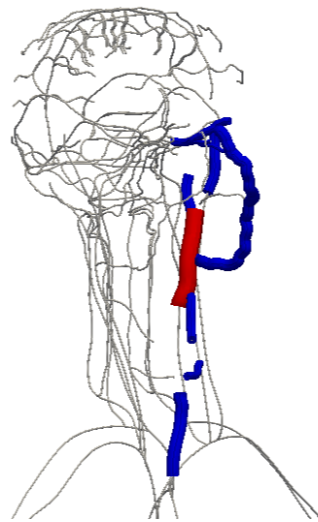


**Figure 7.7:** In red is depicted the left external carotid artery, in blue the terminal veins connected to it [5].

### Neck Vessels: Right External Carotid Artery

The following is a list of terminal veins connected to the right external carotid artery, as depicted in [Figure 7.8](#):

- ▷ Right central retinal vein
- ▷ Right facial vein
- ▷ Right inferior ophthalmic vein
- ▷ Right middle thyroid vein
- ▷ Right posterior auricular vein
- ▷ Right superficial temporal vein
- ▷ Right superior ophthalmic vein
- ▷ Right superior thyroid vein

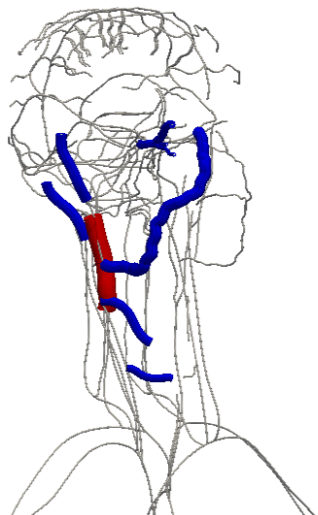


**Figure 7.8:** In red is depicted the right external carotid artery, in blue the terminal veins connected to it [5].

### Torso and Abdomen Vessels: Azygos Vein

The following is a list of terminal arteries connected to the azygos vein, as depicted in [Figure 7.9](#):

- ▷ Right posterior intercostal artery
- ▷ Left posterior intercostal artery

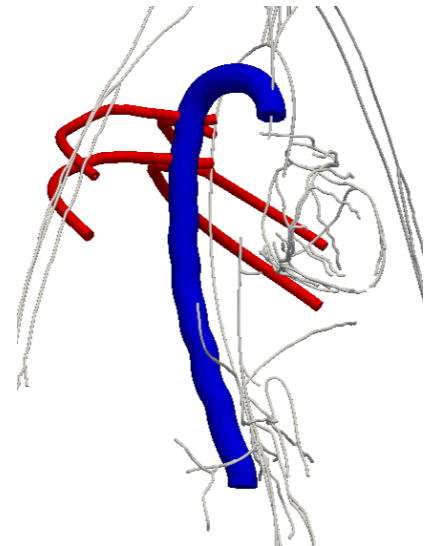


**Figure 7.9:** In blue is depicted the azygos vein, in red the arteries connected to it [5].

### Torso and Abdomen Vessels: Hepatic Vein

The following is a list of terminal arteries connected to the hepatic vein, as depicted in [Figure 7.10](#):

- ▷ Left gastric artery
- ▷ Splenic artery
- ▷ Dorsal pancreatic artery
- ▷ Middle colic artery
- ▷ Inferior mesenteric artery
- ▷ Superior mesenteric artery
- ▷ Jejunal artery
- ▷ Ileal artery
- ▷ Ileocolic artery

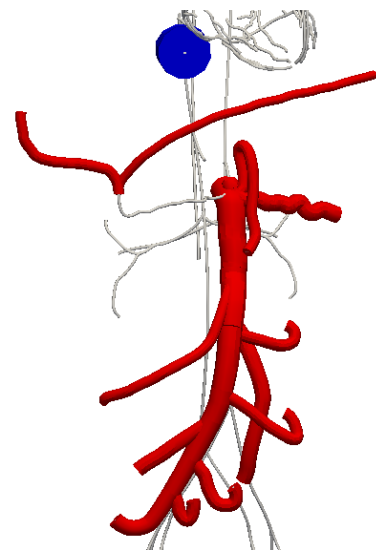


**Figure 7.10:** In blue is depicted the hepatic vein, in red the arteries connected to it [5].

**Torso and Abdomen Vessels: Venous Perforator**

The following is a list of terminal arteries connected to the venous perforator, as depicted in [Figure 7.11](#):

- ▷ Right posterior intercostal artery
- ▷ Left posterior intercostal artery

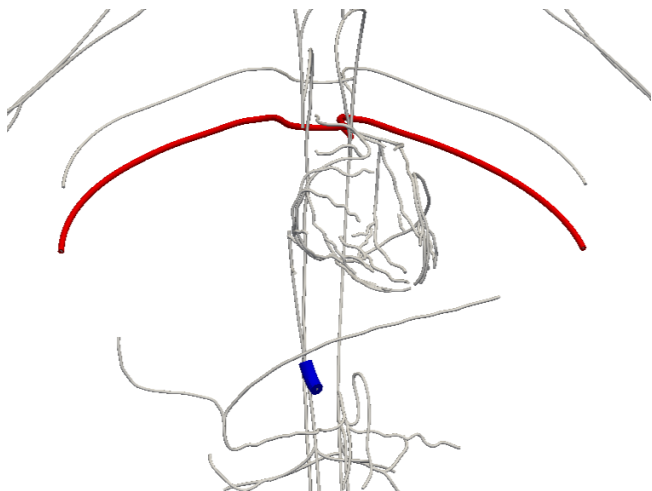


**Figure 7.11:** In blue is depicted the venous perforator, in red the arteries connected to it [5].

**Torso and Abdomen Vessels: Left Renal Vein**

The following is a list of terminal arteries connected to the left renal vein, as depicted in [Figure 7.12](#):

- ▷ Left superior segmental artery
- ▷ Left inferior segmental artery
- ▷ Left renal posterior branch artery

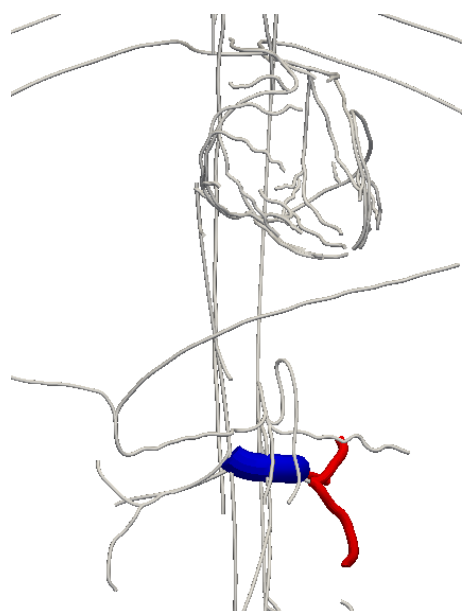


**Figure 7.12:** In blue is depicted the left renal vein, in red the arteries connected to it [5].

**Torso and Abdomen Vessels: Right Renal Vein**

The following is a list of terminal arteries connected to the right renal vein, as depicted in [Figure 7.13](#):

- ▷ Right renal posterior branch artery
- ▷ Right superior segmental artery
- ▷ Right inferior segmental artery

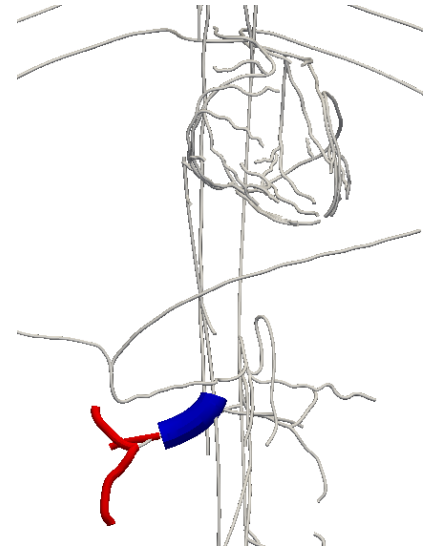


**Figure 7.13:** In blue is depicted the right renal vein, in red the arteries connected to it [5].

**Torso and Abdomen Vessels: Right Internal Iliac Vein**

The following is a list of terminal arteries connected to the right internal iliac vein, as depicted in [Figure 7.14](#):

- ▷ Right internal iliac artery

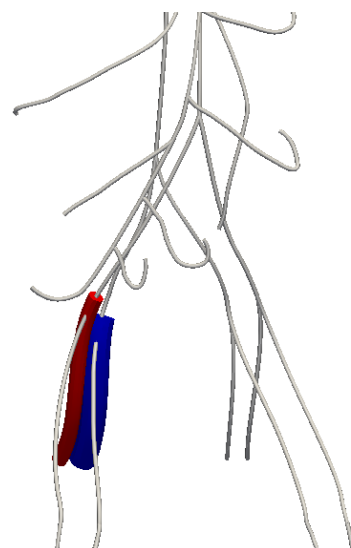


**Figure 7.14:** In blue is depicted the right internal iliac vein, in red the arteries connected to it [5].

**Torso and Abdomen Vessels: Left Internal Iliac Vein**

The following is a list of terminal arteries connected to the left internal iliac vein, as depicted in [Figure 7.15](#):

- ▷ Left internal iliac artery

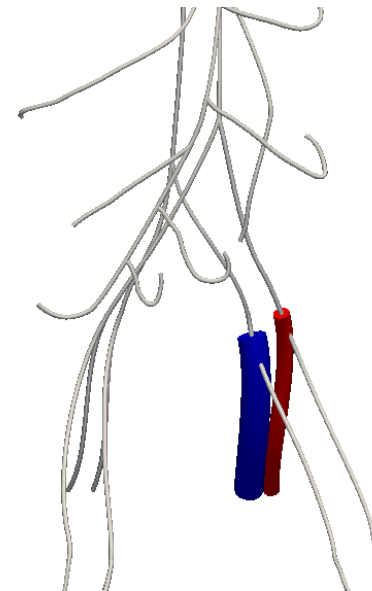


**Figure 7.15:** In blue is depicted the left internal iliac vein, in red the arteries connected to it [5].

**Arm and Leg Vessels: Left Posterior Interosseous Artery**

The following is a list of terminal veins connected to the left posterior interosseous artery, as depicted in [Figure 7.16](#):

- ▷ Left anterior interosseous vein

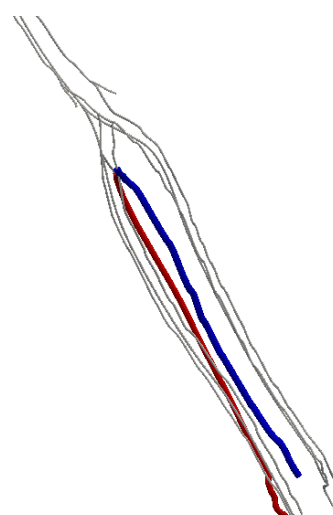


**Figure 7.16:** In red is depicted the left posterior interosseous artery, in blue the veins connected to it [5].

**Arm and Leg Vessels: Right Posterior Interosseous Artery**

The following is a list of terminal veins connected to the right posterior interosseous artery, as depicted in [Figure 7.17](#):

- ▷ Right anterior interosseous vein

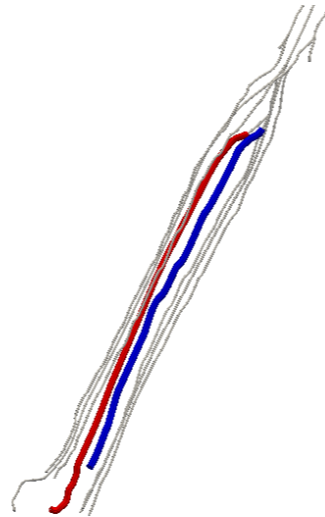


**Figure 7.17:** In red is depicted the right posterior interosseous artery, in blue the veins connected to it [5].

**Arm and Leg Vessels: Left Radial Artery**

The following is a list of terminal veins connected to the left radial artery, as depicted in [Figure 7.18](#):

- ▷ Left venous perforator
- ▷ Left radial vein

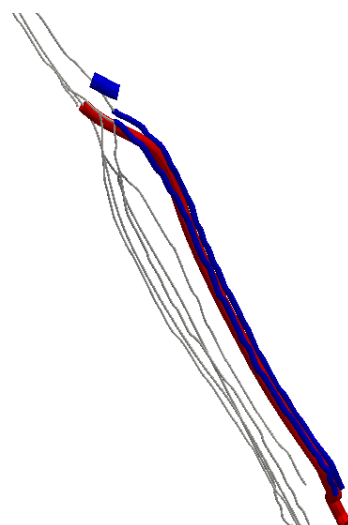


**Figure 7.18:** In red is depicted the left radial artery, in blue the veins connected to it [5].

### Arm and Leg Vessels: Right Radial Artery

The following is a list of terminal veins connected to the right radial artery, as depicted in [Figure 7.19](#):

- ▷ Right venous perforator
- ▷ Right radial vein

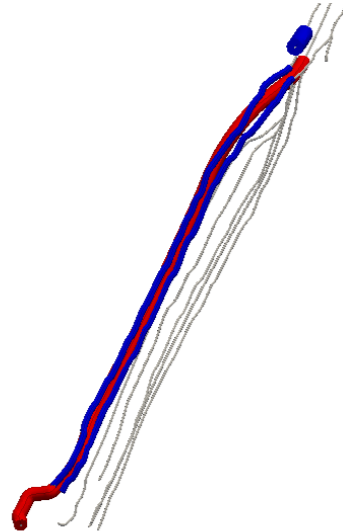


**Figure 7.19:** In red is depicted the right radial artery, in blue the veins connected to it [5].

### Arm and Leg Vessels: Left Ulnar Artery

The following is a list of terminal veins connected to the left ulnar artery, as depicted in [Figure 7.20](#):

- ▷ Left venous perforator
- ▷ Left ulnar vein

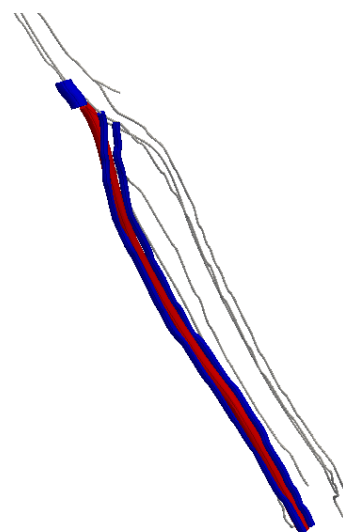


**Figure 7.20:** In red is depicted the left ulnar artery, in blue the veins connected to it [5].

**Arm and Leg Vessels: Right Ulnar Artery**

The following is a list of terminal veins connected to the right ulnar artery, as depicted in [Figure 7.21](#):

- ▷ Right venous perforator
- ▷ Right ulnar vein

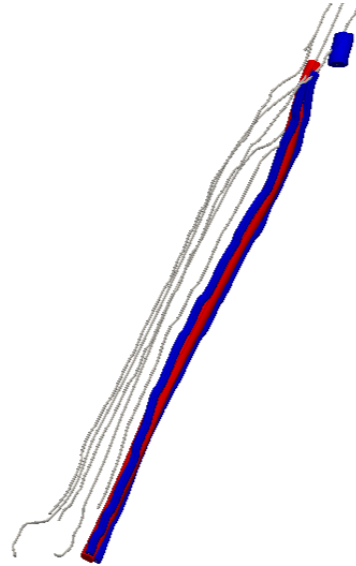


**Figure 7.21:** In red is depicted the right ulnar artery, in blue the veins connected to it [5].

**Arm and Leg Vessels: Left Profunda Femoris Artery**

The following is a list of terminal veins connected to the left profunda femoris artery, as depicted in [Figure 7.22](#):

- ▷ Left profunda femoris vein

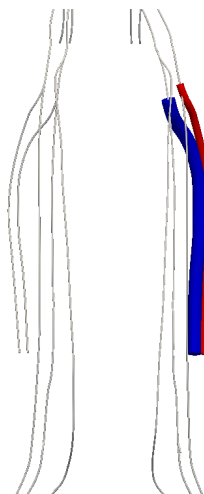


**Figure 7.22:** In red is depicted the left profunda femoris artery, in blue the veins connected to it [5].

**Arm and Leg Vessels: Right Profunda Femoris Artery**

The following is a list of terminal veins connected to the right profunda femoris artery, as depicted in [Figure 7.23](#):

- ▷ Right profunda femoris vein

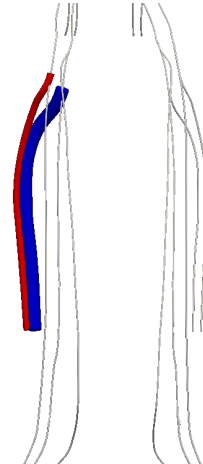


**Figure 7.23:** In red is depicted the right profunda femoris artery, in blue the veins connected to it [5].

**Arm and Leg Vessels: Left Anterior Tibial Artery**

The following is a list of terminal veins connected to the left anterior tibial artery, as depicted in [Figure 7.24](#):

- ▷ Left venous perforator
- ▷ Left anterior tibial vein

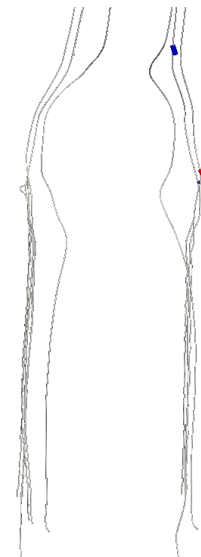


**Figure 7.24:** In red is depicted the left anterior tibial artery, in blue the veins connected to it [5].

**Arm and Leg Vessels: Right Anterior Tibial Artery**

The following is a list of terminal veins connected to the right anterior tibial artery, as depicted in [Figure 7.25](#):

- ▷ Right venous perforator
- ▷ Right anterior tibial vein

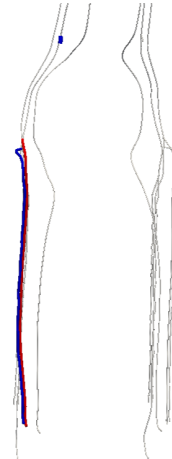


**Figure 7.25:** In red is depicted the right anterior tibial artery, in blue the veins connected to it [5].

**Arm and Leg Vessels: Left Posterior Tibial Artery**

The following is a list of terminal veins connected to the left posterior tibial artery, as depicted in [Figure 7.26](#):

- ▷ Left posterior tibial vein 1
- ▷ Left great saphenous vein

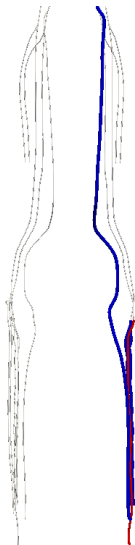


**Figure 7.26:** In red is depicted the left posterior tibial artery, in blue the veins connected to it [5].

### Arm and Leg Vessels: Right Posterior Tibial Artery

The following is a list of terminal veins connected to the right posterior tibial artery, as depicted in [Figure 7.27](#):

- ▷ Right posterior tibial vein
- ▷ Right great saphenous vein



**Figure 7.27:** In red is depicted the right posterior tibial artery, in blue the veins connected to it [5].

## 2 Cardiovascular Adaptation Mechanisms in CircAdapt

Adaptation in the cardiovascular system is a fundamental concept and a key strength of the CircAdapt model. Adaptation rules simulate the macroscopic effects of processes where mechanical signals induce gene expressions, leading to changes in cell structure and mechanical behavior within the cell's vicinity. These complex, intertwined adaptation mechanisms are summarized into relatively simple rules. The geometry of the cardiac cavities and vessel walls adapts to normalize the load on the surrounding tissues [1].

This feature of the CircAdapt model is utilized only when pathologies or changes are made to the model once the solution has reached convergence. While this characteristic is not used in the current project, it remains an important aspect of the model. Since it might be used in the future in the context of the coupled model developed in this thesis, it is considered sufficiently important to be included in the work, but only in the appendix.

### 2.1 Cardiovascular Adaptation in the Human Heart

The human heart is a four-chambered muscular organ that drives the circulatory system [7]. Its primary function is to ensure a continuous supply of oxygenated blood to the organs through systemic arteries (systemic circulation) and to recycle deoxygenated blood back to the lungs via systemic veins (pulmonary circulation) for reoxygenation. This complex task is managed efficiently by a regulatory system that adjusts cardiac output in response to physiological changes such as stress, physical exercise, and illness. A healthy human heart typically beats at a rate of 60-100 beats per minute and maintains a cardiac output of 5-6 liters of blood per minute in adults. Unlike skeletal muscles, the specialized cardiac muscle tissue does not fatigue under

stress but requires a constant oxygen supply and is vulnerable to damage (infarction) if this supply is interrupted. Previously, it was believed that cardiac muscle cells could not regenerate after damage. However, recent studies have indicated that some regeneration, approximately 1% of the total volume per year, is possible [4].

## 2.2 Example of Adaptation: Raise in Arterial Pressure

As an example to demonstrate the complexity of cardiovascular system adaptations, a raised arterial pressure evokes these secondary effects (see the diagrammatical summary in [Figure 7.28](#)) [6]:

1. Compensation through the Frank–Starling mechanism.

When arterial pressure increases acutely, initial ejection is reduced. This causes blood to accumulate in the left ventricle, expanding the end-diastolic volume over a few beats. This expansion increases the contractile energy of the ventricle via the Frank–Starling mechanism. Consequently, the pump function curve shifts to a higher level, improving stroke volume but causing cardiac dilation.

2. Compensation through the Anrep effect.

Over the next 5–10 minutes, further adaptation occurs. The contractility of the ventricle increases, enabling it to maintain stroke volume from a lower, near-normal end-diastolic volume. This response, known as the Anrep effect, involves several mechanisms:

- ▷ Inotropic agents, such as myocardial angiotensin II and endothelin 1, are produced within the myocardium. These agents increase the myocyte  $\text{Ca}^{2+}$  store and  $\text{Ca}^{2+}$  transient.
- ▷ Activation of the  $\text{Na}^+/\text{H}^+$  pumps raises intracellular  $\text{Na}^+$ , which slows the expulsion of  $\text{Ca}^{2+}$  by the  $\text{Na}^+/\text{Ca}^{2+}$  exchanger.
- ▷ Stretch-activated channels increase the entry of extracellular  $\text{Ca}^{2+}$ , boosting the  $\text{Ca}^{2+}$  store.

3. Reduction of output by the baroreflex.

In an intact animal, an acute rise in arterial pressure triggers the baroreceptor reflex. This reflex reduces cardiac sympathetic nerve activity, decreasing ventricular contractility, stroke volume, and heart rate, thereby returning arterial pressure to normal.

The overall effect of an acute rise in arterial pressure on stroke volume depends on the interplay between two negative influences (increased afterload and the baroreflex) and two compensatory changes (the Starling and Anrep effects).

## 2.3 Adaptation Rules in CircAdapt

The CircAdapt model simulates various aspects of cardiovascular adaptation. This allows for the modification of a wide range of parameters to achieve simulations of the pathological cases or patient-specific scenarios (see [Figure 7.29](#)) [2]. As demonstrated in [2], the model can be used to simulate left ventricle function in elderly patients, estimate the pressure-volume loop of the left ventricle, and simulate the delay of LV activation in left bundle branch block using patient measurements. Therefore, the CircAdapt model is an excellent tool for similar applications, also due to its modular structure, which makes it versatile.

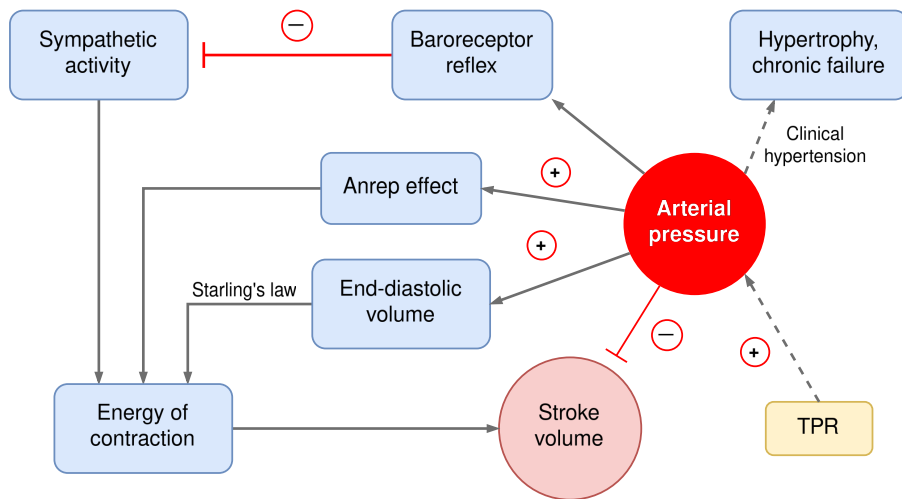


**Figure 7.28:** An acute rise in arterial pressure (AP), resulting from a rise in total peripheral resistance (TPR), affects stroke volume through two negative and two positive mechanisms. TPR may be increased acutely by sympathetic vasomotor activity, or chronically by clinical hypertension. Chronic hypertension introduces additional factors: ventricular hypertrophy and eventual failure. On the right side, pulmonary resistance may be increased acutely by pulmonary embolism, raising pulmonary AP. Adapted from [6].

### Adaptation in Cardiovascular Tissue

The CircAdapt model attributes adaptation to tissue properties. For a given tissue, various types of load or concentrations are sensed and compared with tissue-specific set points. Following the principle that both load sensing and compensatory actions occur in and around the same cell, the model assumes that discrepancies between actual load and set points trigger adaptive actions in the immediate environment of the sensing location. Different tissue types have different adaptation rules. The model focuses on mechanical load sensing and the resulting adaptation effects such as growth or changes in structure or function. These adaptation effects change the dimensions and structure of the heart and blood vessels, counteracting discrepancies between actual and reference load levels, thus closing the control loop by adaptation. Once adaptation is complete, a steady state is reached with load near the set-point values, meaning that load is uniformly distributed over the tissues. Adaptation drives the self-organization of the circulatory system elements, ensuring tissues work within their optimal performance range.

### Adaptation in Myocardial Tissue

The model distinguishes between two types of myocardial hypertrophy: concentric and eccentric. Concentric hypertrophy is induced by pressure overload, leading to wall thickening without changing cavity volume. Eccentric hypertrophy is induced by volume overload, leading to wall thickening with a proportional increase in cavity diameter.

The model considers the diastolic stress or stretch in the extracellular matrix as trigger for hypertrophy. Increased volume load stretches the wall, causing an increase in wall mass. Similarly, increased afterload hampers full ejection, raising end-systolic volume and stretching the wall, thus increasing wall mass.

The model postulates that both preload and afterload induce myocardial hypertrophy, with high strain during the cardiac cycle causing myocardial tissue to soften and dilate, differentiating between concentric and eccentric hypertrophy.

Myofiber orientation, crucial for the three-dimensional modeling of the heart, is assumed to

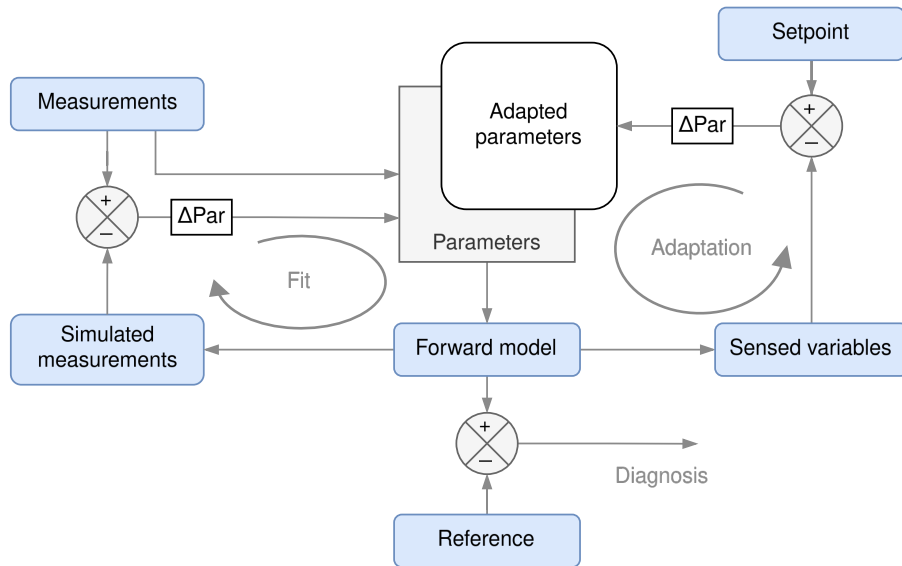


**Figure 7.29:** Patient-specific modeling. With more comprehensive models, usually there are too many parameters for a reliable fit. Physiological knowledge of adaption of subsystems to load is used to simulate a most likely state of adaptation, thus narrowing down uncertainty in many parameters. A remaining relatively small set of parameters is fit to available measurements for assessment of the status of the patient. Investigation whether critical values in the simulation are within the normal or pathologic range allows diagnostic differentiation. Adapted from [2]

adapt by aligning with optimal strain levels or stress directions. This adaptation rule suggests that myofibers maintain straight pathways during systole and diastole to optimize their function.

### Sarcomere and Myofiber Adaptation

Sarcomeres, responsible for myocardial contraction, have a narrow working range of length. The model incorporates a control mechanism for sarcomere length, considering it narrow and controlled by adding more sarcomeres in series. The adaptation rule for myofiber is about directioning it by the stress along itself, which is equivalent with directioning by transverse shear strain at the beginning of systole. With this adaptation rule, the myofiber searches for straight pathways of systolic stress. If the myofibers were not straight before contraction, the extracellular matrix around the myofibers would be deformed in systole, thus imposing stresses perpendicular to the myofibers. With the proposed adaptation rule, the model assumes that the active myofiber migrates through the passive matrix structure until the oblique stress component disappears. As a result, myofiber pathways tend to follow straight (geodesic) pathways in systole, while maintaining their straightness in diastole.

### Vascular Adaptation

Blood vessels, composed of intima, media, and adventitia layers, adapt their diameter in response to shear stress from blood flow. Increased flow and shear stress induce wall dilation, reducing flow velocity and shear stress, closing the control loop for vessel diameter. However, shear stress control varies between small and large vessels, with small vessels universally experiencing high shear rates and large vessels showing additional sensitivity mechanisms. Additionally, vessel wall thickness adapts to transmural pressure to maintain constant wall stress.

## 2.4 CircAdapt Adaptation in Detail: Vessel Adaptation

### Neural Control and Reflex Mechanisms in Cardiovascular Regulation [6]

The activity of the cardiovascular sympathetic and parasympathetic nerves is regulated by the brain, which is guided by sensory information from neural receptors both inside and outside the circulation. Key sensors include pressure receptors in the walls of specific systemic arteries (arterial baroreceptors) and pressure receptors in the heart (cardiopulmonary receptors). Afferent fibers from these receptors transmit information about arterial blood pressure (BP) and cardiac filling to the brainstem, where it is integrated with information from muscle receptors, arterial chemoreceptors, and other sensors.

These reflexes often, but not always, aim to stabilize BP. For example, a reflex response to a rise in BP is bradycardia and peripheral vasodilatation, which restore BP to its original level, known as a depressor reflex. Other reflexes, such as those from arterial and muscle chemoreceptors, are excitatory and raise rather than stabilize pressure (pressor reflexes).

### Baroreceptors: Location, Mechanism, and Function [6]

Baroreceptors are located in the adventitia of arteries (see [Figure 7.30](#)) at two main sites: the carotid sinus and the aortic arch. Aortic baroreceptors are primarily found on the transverse arch of the aorta.

Baroreceptors are mechanoreceptors that respond to stretch, not blood flow. A rise in arterial pressure stretches the artery wall, deforming and exciting the receptor terminals. The wall of the carotid sinus is relatively thin, with the sinus diameter changing by approximately 15% with each pulse. Arterial baroreceptors respond to both the magnitude of pressure (static sensitivity) and its rate of change (dynamic sensitivity).

Carotid baroreceptors signal not only the mean pressure but also the size of the oscillation about the mean, or the pulse pressure.

The baroreflex adjusts cardiac output and peripheral vascular tone to stabilize arterial BP. Experimental animals deprived of baroreceptor input exhibit highly unstable arterial pressure from minute to minute.

### CircAdapt Model and Vascular Adaptation [1, 3]

Although the CircAdapt model does not simulate the vast network of receptors and complex biochemical pathways present in the human body, it mimics the adaptation of blood vessels to maintain specific flow rates and withstand internal pressures. It is designed to reflect the natural adaptation processes in the human body: in both the model and the body, the vessel cross-sectional area adjusts to regulate blood flow shear rate, and the vessel walls adapt to handle varying pressures without exceeding stress limits. Additionally, Circadapt accounts for dynamic physiological conditions, such as movement-induced pressure fluctuations, mirroring how the body naturally adjusts to different physical activities and impacts.

#### CircAdapt Adaptation of the Tube

In a vessel,  $A_t^{\text{ref}}$  adapts to maintain a level of flow shear rate  $S_t^e$  along the endothelium of the blood vessel [3]. Assuming a parabolic profile one obtains:

$$A_t^{\text{ref}} = \pi^{1/3} \left( 4 \frac{q_t^{\text{ref}}}{S_t^e} \right)^{2/3}, \quad (7.1)$$

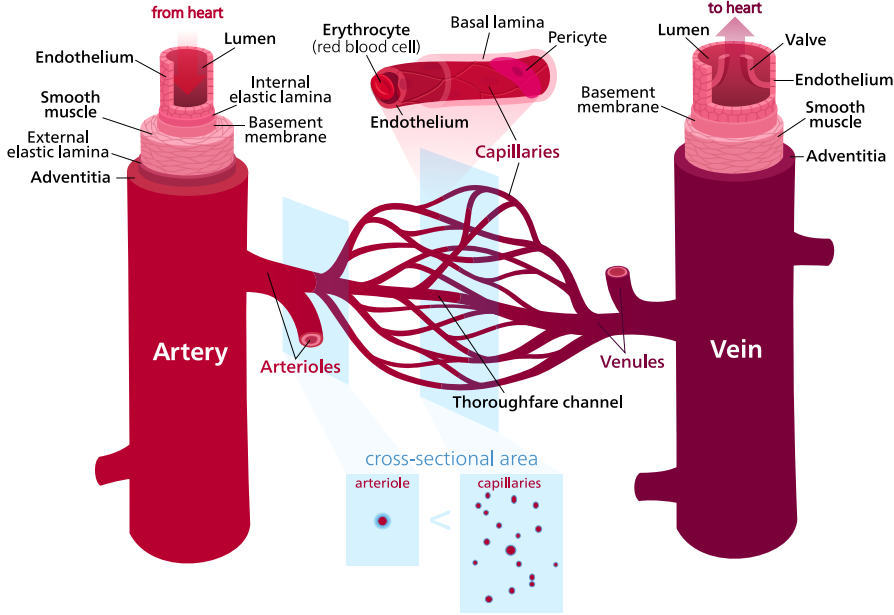


**Figure 7.30:** Summary diagram of blood vessel structure. Image used under the Creative Commons Attribution-Share Alike 3.0 Unported license; image author (Wikimedia Commons user): Begoon; image link: [Blood vessels]

where  $q_t^{\text{ref}}$  is the mean flow [1].

As an inherent characteristic of the vessel wall, it must be sufficiently thick to endure a maximum pressure  $p_t^{\max}$  while experiencing maximum wall stress  $\sigma_t^{\max}$ . With use of (3.2) and (3.3) for maximum pressure load one obtains:

$$A_t^{\text{wall}} = \frac{3A_t^{\text{ref}}}{\frac{\sigma_t^{\max}}{p_t^{\max}} - 1}. \quad (7.2)$$

Equations (7.1) and (7.2) hold for different mean physiological working pressure and maximum occurring pressure, respectively. If (3.5) is applied to both loading conditions one obtains

$$\frac{p_t^{\text{ref}}}{p_t^{\max}} = \left( \frac{A_t^{\text{wall}} + 2A_t^{\text{ref}}}{A_t^{\text{wall}} + 2A_t^{\max}} \right)^{\frac{k-3}{3}}. \quad (7.3)$$

Solving the system (7.2) and (7.3) by eliminating  $A_t^{\max}$  for  $A_t^{\text{wall}}$  one obtains:

$$A_t^{\text{wall}} = \frac{3A_t^{\text{ref}}}{\sigma_t^{\max} \left( \frac{p_t^{\text{ref}}}{p_t^{\max}} \right)^{\frac{3}{k-3}} - 1}, \quad (7.4)$$

where  $p_t^{\max}$  may appear very low for veins, with (7.4) leading to very thin vessel walls.

It is important to recognize that a living body undergoes arbitrary movements, leading to pressure fluctuations in blood vessels. The model assumes that the body frequently experiences impacts with velocity  $v_t^{\text{impact}}$ , for example, from jumping. A column of blood moving at this velocity generates a flow shock wave, resulting in a pressure step influenced by the wave impedance  $Z_t$  from (3.8). Therefore, the model considers

$$p_t^{\max} = \max[p(t)] + Z_t A_t v_t^{\text{impact}}. \quad (7.5)$$



---

# Bibliography

---

- [1] Theo Arts et al. “**Adaptation to Mechanical Load Determines Shape and Properties of Heart and Circulation: The CircAdapt Model**”. In: *American Journal of Physiology—Heart and Circulatory Physiology* 288.4 (Apr. 2005), H1943–H1954. DOI: [10.1152/ajpheart.00444.2004](https://doi.org/10.1152/ajpheart.00444.2004).
- [2] Theo Arts et al. “**Patient-Specific Modeling of Cardiovascular Dynamics with a Major Role for Adaptation**”. In: *Patient-Specific Modeling of the Cardiovascular System*. Springer New York, 2010, pp. 21–41. DOI: [10.1007/978-1-4419-6691-9\\_2](https://doi.org/10.1007/978-1-4419-6691-9_2).
- [3] Christoph M. Augustin et al. “**A computationally efficient physiologically comprehensive 3D–0D closed-loop model of the heart and circulation**”. In: *Computer Methods in Applied Mechanics and Engineering* 386 (Dec. 2021), p. 114092. DOI: [10.1016/j.cma.2021.114092](https://doi.org/10.1016/j.cma.2021.114092).
- [4] Olaf Bergmann et al. “**Evidence for Cardiomyocyte Renewal in Humans**”. In: *Science* 324.5923 (Apr. 2009), pp. 98–102. DOI: [10.1126/science.1164680](https://doi.org/10.1126/science.1164680).
- [5] Caterina Dalmaso. *Preliminary Documentation for ADAVN86*. Tech. rep. Trento (TN): Università degli Studi di Trento, 2024.
- [6] David J. Paterson Neil Herring. “**Levick’s Introduction to Cardiovascular Physiology, Sixth Edition**”. Elsevier, 1991. DOI: [10.1016/c2013-0-06523-1](https://doi.org/10.1016/c2013-0-06523-1).
- [7] Alfio Quarteroni et al. “**Integrated Heart—Coupling multiscale and multi-physics models for the simulation of the cardiac function**”. In: *Computer Methods in Applied Mechanics and Engineering* 314 (Feb. 2017), pp. 345–407. DOI: [10.1016/j.cma.2016.05.031](https://doi.org/10.1016/j.cma.2016.05.031).